Full-field measurements for the mechanics of micrometer-sized structures

Fabien Amiot

EDSP
École Doctorale
Sciences Pratiques

ENS
CACHAN

Mémoire

Présenté par
Fabien AMIOT

en vue de l'obtention
de l'habilitation à diriger les recherches :

Full-field measurements for the mechanics of micrometer-sized structures

soutenu à Cachan le 17 Avril 2015 devant le jury composé de :

Stéphane ANDRIEUX	Directeur Scientifique ONERA	Rapporteur
Claude BOCCARA	Professeur (ESPCI)	Président
Hans-Jürgen BUTT	Professeur (Max Planck Institute for Polymer Research)	Examinateur
Samuel FOREST	Directeur de Recherche (CNRS)	Rapporteur
Christian FRETIGNY	Directeur de Recherche (CNRS)	Rapporteur
François HILD	Directeur de Recherche (CNRS)	Garant
Frédéric KANOUFI	Directeur de Recherche (CNRS)	Invité

To cite this document : F. Amiot, Full-field measurements for the mechanics of micrometer-sized structures, Habilitation thesis, 2015. DOI :

C’est autant le souci de nommer les têtes de pont qui balisent cette zone de “l’archipel des sciences” dans laquelle je croise que celui de manifester ma profonde gratitude pour les contributions (plus ou moins directes, mais toujours indispensables) au travail présenté ici qui m’incitent à remercier :

Stéphane Andrieux, Samuel Forest et Christian Frétigny pour avoir accepté de rapporter sur ce document ;

Claude Boccara, Hans-Jürgen Butt et Frédéric Kanoufi pour avoir accepté de participer au jury ;

François Hild pour avoir accepté, avec la rigueur qui le caractérise, d’être garant de ce travail ;

Gaël Chevalier pour la relecture, en naïf, du document ;

Gaël Chevalier (encore), Yves Gaillard et Morvan Ouisse pour le regard critique porté sur la présentation ;

Catherine Génin, bienveillant et indispensable relais dans l’organisation de la soutenance ;

Jean Paul Roger, Frédéric Kanoufi (encore) et Gilles Tessier, pour leur compagnonnage sur les pistes parfois farfelues de mon imagination ;

Anja Boisen, Zach Davis, Søren Dohn, Maria Tenje, Stefan Keller, Gabi Blagoi, Jan Hales (et les autres...) pour leur confiance, leur efficacité et leur compréhension durant de mes années scandinaves ;

Michel de Labachelerie, Lamine Boubakar et Patrick Delobelle pour leur soutien et leur souci d’assurer le meilleur environnement possible pour mon activité scientifique à FEMTO-ST ;

Les membres (passés et présents) du thème PMMCM, Pascal Vairac et les caféïnomanes anonymes qui se reconnaîtront pour les discussions (plus ou moins) scientifiques partagées ;

Béatrice Parguel pour l’accueil toujours parfait sur son matelas gonflable et parisien.

This document gathers some of the ideas, developments and results for the period 2006-2014. It results from the extension of the research initiated with a PhD thesis defended in December 2005. In order to provide tools to describe chemically-induced mechanical deformations, the PhD thesis proposed and implemented methods:

- To measure nanometric displacement fields at the micrometer scale;
- To identify heterogeneous surface loading fields and heterogeneous mechanical properties fields, and to assess a model quality;
- To model strong surface couplings.

This initial work, which focused on the deformation of microcantilevers induced by DNA hybridization, was supervised by François Hild (LMT-Cachan) and Jean Paul Roger (LOP-ESPCI). It allowed for the identification of the main experimental and theoretical barriers to be overcome in order to describe surface mechanical couplings. This work has been extended:

- By focusing on reproducible and easily controllable surface modifications induced by electrochemistry. This was initiated during a post-doc stay at MIC-DTU and pursued by collaborating with Frédéric Kanoufi (PECSA-ESPCI).
- By developing processes to fabricate dedicated micromechanical structures (post-doc stay at MIC-DTU, PhD work of Cécile Flammier, post-doc of Chang Wu).
- By developing imaging techniques providing simultaneously access to kinematic and/or chemical fields. This analysis was part of the PhD work of Nicolas Garraud.
- By proposing two different ways of modeling surface couplings, namely, an asymptotic modeling (developed during a post-doc stay at MIC-DTU) and a second strain gradient description of materials. The inverse problem resulting from the asymptotic description has been studied during the Ph.D work of Cécile Flammier.

Whatever the considered mechanical description, the in-situ mechanical characterization at the microscale of the involved materials is a key point for the quantitative analysis of surface couplings. A collaboration with Pascal Vairac and Patrick Delobelle (FEMTO-ST) has thus been initiated in order to extend the capabilities and the robustness of the scanning microdeformation microscope (SMM). This collaboration has initiated the development of:

- an imaging technique providing access to surface rotation instead of surface displacement. This is particularly desirable in order to access kinematic quantities nearby a tip in contact with a specimen.
- an identification method based on the extension of the equilibrium gap method to dynamic systems that has also been implemented to decouple elastic parameters from multiple modes SMM.

Both aspects have been first devised in collaboration with Søren Dohn at MIC-DTU, and fully implemented as part of the PhD work of Thomas Travaillot.

All these contributions aim at building a quantitative description of surface couplings from experimental data at the micrometer scale.

Contents

List of Figures

List of Tables

Introduction

The development of micro- and nanotechnologies has first been envisioned as a scientific and technological breakthrough by Drexler in 1981 [1]. Inspired by a lecture given by Richard Feynman in 1959, he suggested that engineering at the molecular level would be the next scientific and technological revolution.

Even though these utopian views were first received by skepticism, they quickly turned out to be reachable with the first set-ups based on tunneling effect in 1982 [2] and the synthesis of fullerenes by Smalley's group [3]. The race for the control of single molecules was just starting.

As often, the development of research activities was supported by the prevailing views considering that most of the key challenges (western) societies had to face could benefit from (or should not be taken up without) micro- and nano-technologies. The first decade of the 2000s was that of all the promises, namely, iron nanoparticles were seen as the agent for in-situ soil remediation [4], nanotechnologies were expected to play a key role in the hydrogen based economy, to significantly improve solar power technology or to allow for next generation batteries, so that it could have a profound impact on energy consumption and hence greenhouse gas emissions [5]. Nanoparticle aerosols were also thought as a tool to engineer the Earth's albedo and thus to gain control over global climate changes [6].

Simultaneously, scaling down the objects makes them of interest for scientists of several (previously strictly separated) disciplines, thus blurring the borders between investigation fields that were remaining distinct. This is illustrated with molecular electronics, which originates from the possibility to manipulate very few molecules and to have access to their electronic state. This yields new hybrid electronic devices using either new transistors or new physical ways to store information, such as triggering the oxidation state of molecules (porphyrins for example) [7].

This reorganization of knowledge fields, usually referred to as "convergence" when focusing on the distance between life and physical sciences, efficiently reactivated Prometheus myth and attracted massive funding [8]. Besides groundbreaking innovations, this convergence between biology and nanotechnology was thought to renew the engineering process as well as the links between science and societies.

This last point is of particular importance. If the genetically-modified organisms episode stressed the fact that shaping the future a new technology opens is a continuous social construction, it also highlighted that scientists and funding organizations are not the sole stakeholders. Many organizations (*e.g.,* NGOs, groups of concerned citi-

zens) claimed the right to be part of this shaping process, hence calling for a democratic definition of research policies. The nanotechnology era has thus been seen as an opportunity (for sociologists) to observe in real-time this shaping process and (for anybody) to experience an open, pacified, two-way interaction between "science" and societies [9].

Besides social engineering attempts intended to fake an "upstream" shaping of the nanotechnology research agenda, it looks like the promise for a renewed connection between science and societies was vain so far. Several organizations (*e.g.,* ETC group, Friends of the Earth) are thus still struggling for a more open way to direct the research effort and campaigning to raise awareness of the risks associated with the present research priorities. As a consequence, shaping the research agenda or adapting regulations keep on relying on a conflictual relationship between academic research and/or economic needs, NGOs campaigning and scientists responsibility. This may be illustrated by the widespread use of nanomaterials in food, initiatives such as the "is there nano in your sweets?" campaign by *As You Sow* [10] and discussions among toxicologists to decide whether nanomaterials should be considered as a new class of toxic chemicals under REACH regulation (Registration Evaluation Authorization and Restriction of Chemicals) [11].

This environment generates a rather controversial field, to which mechanical scientists should be prepared. They actually would be mistaken to consider themselves as far from the above-mentioned "convergence", namely, the chemo-mechanical couplings initially exploited to devise micromechanical sensors [12] may now be the key for the design of homeostatic mechanical systems, and may thus play a crucial role in moving toward synthetic biology [13].

As micromachined commercial products with mechanical features today exploit only the integration capabilities microfabrication technologies allow (for mass-production of reliable products), there is room for innovative products making the most of micrometer-sized objects, which are very specific from the mechanical point of view for two reasons:

- Their surface/volume ratio is much larger than for the objects mechanical engineers are used to deal with. The consequence is that strong surface couplings have been evidenced, translating changes in the (electro-)chemical environment into mechanical deformation.

- the geometric margins (compared to the dimensions) and the material homogeneity resulting from the usual processing techniques are very poor.

As a consequence, studying the mechanical behavior of micrometer-sized objects requires to overcome two main barriers:

- To identify material constitutive laws at the micrometer scale and to quantify the role of the environment on the behavior;

- To model chemo-mechanical couplings when materials are heterogeneous and structures are poorly defined.

Moving forward along these two lines requires the development of a dedicated instrumentation and the use of identification techniques suited both to the available experimental data and to the proposed mechanical descriptions. This document is therefore organized as follows:

- The first chapter is devoted to the mechanical characterization techniques at the micrometer scale. The full-field measurements techniques proposed within the last few years are presented, and the various extensions of scanning microdeformation microscopy toward a quantitative local characterization of anisotropic thin-film materials are detailed.

- The second chapter focuses on chemo-mechanical couplings. The various experimental tools developed to measure and control these couplings are first described, and the two proposed frameworks for modeling these surface couplings are detailed.

Perspectives of my research activities in the coming years are presented and an appendix finally gathers some technical details that may be useful to the interested reader.

Chapter 1

Mechanical characterization at the microscale

This first chapter is devoted to the mechanical characterization techniques at the micrometer scale. As vanishingly small tested volumes may be achieved either by downsizing a fully loaded object or by locally loading larger samples, an overview of the measurements methods proposed for both approaches within the last few years is proposed. It is shown that full-field measurements are desirable for both approaches, and the various extensions of scanning microdeformation microscopy towards a quantitative local characterization of anisotropic thin-film materials are introduced.

Contents

1 Mechanical testing at the microscale

This first section aims at presenting an overview of the mechanical characterization methods proposed in the last few years, focusing on the achievements permitted by the use of full-field measurements and on the needs that still have to be fulfilled. The context is first set by recalling the range of materials under scrutiny.

1.1 Target materials

The iconic material of micromechanical devices is indisputably silicon. Even though most of the silicon metal production goes to alloying applications (with aluminum), the last major shifts in the silicon world market result from the strong growth of silicon use in solar cells [14]. The rapid development of this market motivated the extensive study of the mechanical properties of (poly)silicon wafers [15, 16, 17, 18], as well as their dependence to the material processing conditions [19, 20] and to the product manufacturing parameters (see [21] for dicing, for instance).

The rest of the semiconductor industry only uses one fourth of the silicon used for solar cells [14], but it is clear that the development of MEMS devices requires mechanical data that could not be inferred from traditional (macroscale) tests [22]. Besides elastic properties, lifetime prediction requires fatigue data. If single-crystal silicon [23] is also concerned, most of the effort has been put on polycrystalline silicon (also referred to as polysilicon). Well-defined elaboration processes are commercially available for polysilicon, see for instance the "Multi-User MEMS ProcesS" (MUMPS) that is ARPA-sponsored or "Sandia Ultra-planar Multi-level MEMS Technology" (SUMMiT) [24]. These processes allowed for large scale studies so it became possible to tackle reproducibility issues. The achieved reproducibility even allowed for studying the process-material relationships [25] at an early development stage of MEMS technology. After a time lapse necessary to establish good practices in fatigue testing of polysilicon [26], the first scenarios explaining its fatigue behavior have been proposed [27]. It then became clear that the environment plays a key role and that the surrounding relative humidity controls the fatigue limit to a large extent, through the growth and cracking of an oxide layer [28, 29, 30, 31]. The validity of these scenarios could then be assessed under conditions similar to those experienced by commercially available devices [32, 33] or for monocrystalline silicon [34, 35, 36, 37].

Besides values for the fatigue limit of silicon, its fracture strength is also a key design parameter. A wide range of methods has been devised to estimate such values, with rather contradictory results. The first results were obtained by using surface micromachined cantilevers, which were loaded until fracture using a nanoindentation system [38, 39]. These results could later be compared to those obtained with a different loading device [40]. The key role of the process on the fracture strength distribution of silicon has then been evidenced [41, 42, 43] and confirmed for devices [44]. It highlights the fact that one should first wonder about the flaw population to consider for a Weibull-like statistical

analysis [45]. Depending on the process, the fracture strength may be driven by surface or lateral-surface flaws instead of bulk defects. The same difficulty has been reported with diamond-like carbon material [46]. In addition, one should mention that the ability of the material to sustain shocks has also received some attention [47, 48, 49, 50], as well as tribological properties [51, 52].

Even though it has been less studied, the mechanical properties of silicon nitride for MEMS devices has been investigated [53, 54, 55]. Again, relationships between the elaboration process and the material properties have been evidenced [56, 57].

In addition to silicon and silicon-based materials, MEMS devices make an extensive use of metals that in turn have been investigated, either for their wide use as conductive materials or for their status of "well-known" materials. One thus finds numerous studies of the mechanical properties (elasticity, strength) of aluminum [58], nickel [59], nickel-cobalt alloys [60] or copper [61]. As for silicon, determining fatigue properties is crucial, so that the fatigue behavior of nickel [62], gold [63] or copper [64] has been investigated. Metal layers or devices are also rather easy to elaborate, so that they are used in basic studies of size effects [65] or deformation mechanisms [66, 67, 68].

This very short overview of the involved materials should not be closed without mentioning the rapidly growing use of polymers as MEMS materials. The most promising polymer for MEMS applications is probably SU-8. The SU-8 is a negative, epoxy-type, near-UV photoresist based on EPON SU-8 epoxy resin (from Shell Chemical) that has been originally developed and patented by IBM [69, 70]. This trend is cost-driven [71] and requires a mechanical characterization effort [72]. This is also supported by preliminary studies indicating rather heterogeneous properties for photosensitive polymers [73].

1.2 Methods

When choosing or developing a mechanical testing procedure at the micrometer scale, one has to strike a balance between various needs and constrains:

- As for many macroscopic tests, one may wish to establish a homogeneous stress in the tested volume in order to facilitate the translation from global variables (force, displacement) into local ones (stress, strain).
- The structure under scrutiny should easily obtainable, using reliable and reproducible processes. This is of particular importance since:
  - geometrical fluctuations may significantly jeopardize the above-mentioned strain homogeneity in the tested volume;
  - it has already been demonstrated that the process controls some of the material properties.

- The testing device should be easy to handle. The mechanical connections and the associated margins on positions should not be such as the actual stress field may deviate from the nominal stress field.

One should underline that if the first of these needs concerns materials irrespective of the tested volume scale, the two latter ones are of particular importance for thin film materials and small loaded volumes. Downsizing the sample amplifies the role of geometrical margins and makes the definition of precise and quantitative testing procedures a challenge. Various solutions have emerged in groups from different communities, and their diversity represents the possible combinations between the accessible manufacturing capabilities, instrumentation, and the allowed complexity for the mechanical state.

A wide class of solutions involves micromachined cantilevers [74, 75]. They are easily obtained by surface micromachining and yield simple structures whose behavior is described by closed-form equations, provided the thickness and mechanical properties are homogeneous along the cantilever. They are often loaded using a nano-indentation system, thus making use of a commercially available instrumentation for both the loading and the measurement. Even for such a simple system, it has been shown that it is crucial to carefully assess the underlying modeling and to compare results from different methods [76, 77]. For communities less familiar with nano-indentation systems, adding an actuation layer made of a material deposited under conditions that make it stressed at room temperature on top of the cantilever to be tested is a smart alternative for loading [78, 79]. Such an approach requires an accurate control over the initial stress, but does not necessarily allow to overcome difficulties from uncertain boundary conditions (clamping, interface between the materials). Another alternative is to make use of a surface profilometer instead of a nano-indentation system. Exploiting a constant force mode, the cantilever surface is scanned by a tip that acts both as an actuator and a sensor [80]. This interestingly yields a (low resolution) field information which allows to recover the actual boundary conditions.

There is another solution requiring even less machining, which is rather popular among the polymer and soft matter communities. The material to be tested is deposited on a soft pre-stretched substrate, and the film topography is monitored after the pre-strain is released. The film then buckles and the shape and periodicity of the resulting wrinkles is used to retrieve the elastic properties of the film [81, 82]. It is worth noting that the readout technique may be chosen to allow for quick batch measurements [83]. Even though this is a testing procedure of limited interest for mechanics of materials, it is fairly easy to implement and makes use of macroscopic devices.

An alternative family of approaches is based on the translation at the microscale of the procedures proposed by the ASTM. The primary goal is thus to establish a homogeneous stress state in the tested volume, regardless of the processing complexity and resulting handling issues. This effort was initiated in the late nineties [84, 85, 86] and gave rise to many developments. The interested reader will find several dedicated review papers

[87, 88, 89, 90, 91]. Investigating the scale effects on the mechanical behavior of materials however highlighted the difficulties coming from the above-mentioned trade-off between simple processing and stress state [92]. The need for a tight control over environmental effects as well as the roughness of the material specimen then became crucial challenges to overcome even for a simple tensile testing [93, 94]. As for macro-scale testing, the characterization of brittle materials requires a particular effort [77, 95, 96, 97].

It should be noted that the very last years have shown a much wider dissemination of micromachining capabilities among the mechanics of materials community and offered new trading possibilities so that wafer-scale mechanical characterization methods have been devised [98, 99, 100]. Solutions fully integrating the actuation system to the tested device have been proposed [101, 102, 103]. Along a similar line, discarding surface micro-machining and using focused-ion beam (FIB) to shape testing structures resulted in the development of micro-pillars (whose typical larger dimensions scale as few micrometers) as structures dedicated to the study of elementary plastic processes [104]. The micro-pillar is usually put in a compression state using a nano-indenter placed inside the SEM chamber in which the micro-pillar has been fabricated. The available literature mainly focuses on metals [105], but other materials featuring inelastic deformation mechanisms have been investigated [106]. The obtained results are however questionable since the FIB shaping probably strongly alters the sample surface [107]. The pillar may also be subjected to buckling, which is not easily detected from the sole force-displacement curves retrieved from the nano-indentation system [108]. It should be noted that the feasibility of a poorly spatially-resolved kinematic measurement using the SEM imaging capabilities have been proposed [109]. Accepting a similar but more complex fabrication process allows the tensile testing of specimen of comparable sizes [110, 111, 112] and yields results that stimulate the discussion about the deformation processes in metals [113].

As seen from this rapid overview, the plethora of proposed characterization devices results from the various balances one can achieve between stress-homogeneity, straightforward sample fabrication and handling ease. The main constrain driving the characterization method selection seems however to be the available fabrication techniques, whereas the stress-state in the specimen is always kept (nominally) homogeneous or very simple.

The remainder of this introduction section is thus dedicated to review the development of full-field kinematic measurements, since they potentially allow to release the need for homogeneous stress states. The use of test specimen under heterogeneous stress states may allow for the design of test structures more easily obtainable or using less restrictive processes.

Many full-field kinematic measurement techniques have been made available to the solid mechanics community during the second half of the twentieth century [114]. Even though these techniques were already providing a large amount of mechanically redundant data, their effective use in experimental mechanics was limited. The renewed interest for full-field measurement techniques in the late twentieth century may be seen as

a consequence of the availability of both affordable imaging devices and low-cost computing capabilities. Among these techniques, digital image correlation (DIC) quickly proved to be well suited to the environment found in an experimental mechanics laboratory [115, 116, 117]. It makes use of incoherent illumination and only requires (for plane displacement measurements) a single imaging device focused on the surface under scrutiny [118]. As the complexity is thus pushed back at the numerical processing stage, the easy access to large computing capabilities allowed by personal computers strengthened the interest for such technique [119]. As the determination of a displacement field from a reference and deformed image is an ill-posed problem, its projection onto a user-defined basis is sought [120]. Considering various sets of assumptions on displacement continuity [121], material homogeneity and including various amount of a priori knowledge on the displacement field to be measured yields a plethora of DIC implementations [122]. These approaches can be classified into local or global implementations, depending on whether the displacement field on different subsets is obtained sequentially (local DIC) or in a single step involving the full region of interest (global DIC). Global algorithms are more resource demanding but allow one to tailor the displacement field basis to the phenomena under scrutiny. As these techniques also involve a larger amount of pixels, global implementations usually outperform local ones when comparing noise sensitivities [123]. These imaging techniques are particularly appealing so that some effort has been put on the assessment of the role of several parameters on the accuracy of the obtained displacement fields [124, 125, 126, 127, 128].

As DIC is rather easy to implement, it is an interesting choice when dealing with thin films or MEMS devices, since it provides non-contact kinematic measurements provided that contrasted enough images of the surface under scrutiny are available. As most MEMS devices are essentially planar structures, the measurement of a plane displacement field may be sufficient so that the simpler configuration can be used. DIC has thus been quickly used for small scale devices [129] and for a wide range of materials [58, 130, 131, 132]. As most of the algorithm performances are driven by the characteristics of the images of the pattern attached to the surface, procedures and know-how have been developed in order to produce patterned images [133]. It should also be noted that somehow degraded image processing methods, making use of gold lines [134] or dots [135] instead of a random pattern have also been proposed. These imaging techniques translated from the macroscale already contributed to the development of tension, compression [136] or fatigue [137] testing at the microscale.

It is worth noting that DIC algorithms require images of a pattern whose displacement translates the underlying surface movement, whatever the imaging technique or the origin of the imaged contrast. Topography measurements obtained by confocal microscopy (via global DIC) [138] or atomic force microscopy (AFM) have thus been successfully proposed [139, 140] and applied to study the fracture of polysilicon [141, 142], to estimate residual stresses [143] or to quantify the role of the latter on fracture toughness [144]. If DIC algorithms require contrasted images regardless of the imaging techniques, the scanning nature of AFM induces very different errors and deviations compared to those

encountered in CCD and CMOS imaging devices, so that specific discrepancies may be observed after computing the displacement fields [145]. A very similar comment would apply to images obtained using scanning electron microscopy (SEM) images. They can be used as input for DIC algorithms to characterize thin film materials [146] or estimate residual stresses [147]. To achieve the latter, the hole-drilling method is easily implemented by exploiting a focused ion beam [148]. The strain fields nearby a crack-tip can also be captured [149]. The quantitative determination of kinematic fields similarly requires a careful analysis to assess and control how the imaging parameters control the displacement determination quality [150, 151].

Sticking to optical techniques and dealing with micrometer-sized devices, out-of-plane displacements are usually very small so that interferometric techniques may be used with low coherence length illuminations [152]. The arrangements are usually much more compact and thus much more stable than those at the macroscale, so that interferometric techniques are much more practical. For imaging through disturbed media, differential (common-path) imaging interferometry may be implemented to yield extremely stable imaging devices [153]. With interferometric techniques, the wavelength of the light source acts as a ruler to measure the displacement, so that the spatial or temporal resolution may limit the displacement resolution. This difficulty may be overcome by combining an interferometric technique with a purely geometric one such as fringe projection whose sensitivity may be adjusted to the required dynamic range [154]. For structures requiring 3D displacement measurements, electronic speckle pattern interferometry (ESPI) is an alternative, provided the surface is rough enough to generate a diffraction pattern [155]. It should also be noted that thin films of optically transparent materials may be monitored through the measurement of the stress-induced birefringence they feature [156].

Alternatively, focusing on tiny objects allows for the use of other imaging mechanisms. Full-field measurements may be obtained by using a correlation algorithm with images obtained by techniques such as SEM or TEM [157]. It is also possible to take advantage of the mechanisms involved in forming such images. The scanning lines in a SEM may for instance be used to interact with a grating deposited onto the sample to produce moiré fringes that will be affected by the surface displacement [158]. Such a grating may be e-beam-printed using a resist or FIB-printed [159]. Similarly, high-resolution TEM images obtained in a deformed and a reference area may be used to compute a displacement field with respect to this reference state [160, 161]. The electron beam may also be split to travel through different areas before interfering and thus producing a phase pattern that may be interpreted as a displacement field [162, 163]. The stiffness of materials deposited under conditions that make them stressed at room temperature may thus be obtained by measuring the displacement of the underlying substrate [164]. The various TEM-based techniques are compared in Ref.[165]. Electron backscattered diffraction (EBSD) is now routinely used to characterize crystal orientations or grain boundaries [166]. The spread of the crystal orientation inside a grain may be used to quantify its plastic deformation [167], but measuring elastic strain fields in crystalline materials requires a much better angular

resolution. The measurement relies on the analysis of the recorded EBSD patterns [168]. Different approaches are used to describe the pattern changes [169, 170], all leading to a strain resolution in the 10^{-4} range [171]. Similar strain resolutions have been achieved using confocal Raman microscopy [172]. As probing the Raman effect in strained materials is essentially measuring the intensity of the Raman peak in the backscattered light, the main difficulty is to retrieve from the experimental set-up a sufficient amount of information to resolve the tensorial nature of strains. Several improvements have been successively proposed by controlling the polarization state of the incident and scattered light [173] and by using an off-axis illumination configuration [174]. The spatial resolution is also acceptable to allow for the elastic characterization of MEMS devices [175]. Interestingly, similar difficulties have arisen when trying to measure a full strain tensor by X-ray (Laue) diffraction. Broadband "white" X-ray microbeams are now available in few facilities and are used to illuminate crystalline samples. The local deviatoric part of the strain tensor is deduced from the Laue pattern. Accessing the local hydrostatic strain is slightly more challenging and requires the precise measurement of the spot energy obtained under a monochromatic illumination. Combining these measurements under two different illuminations is particularly difficult, so that very few studies have proposed to measure a full strain tensor map. It should however be highlighted that a method avoiding the need for switching between different illumination sources has been proposed [176], thus allowing for full strain tensor mapping.

A wide range of techniques providing full-field kinematic measurements are thus available. These techniques are thus a way release the need to establish an homogeneous strain state in a tested specimen. The two other main requirements (the testing device should be easily obtainable and easy to handle) are then made easier to satisfy. As mentioned in the introduction, one is particularly interested in probing chemo-mechanical couplings at the microscale so that the chosen full-field measurement technique should allow for a wide range of environmental conditions. The next sections of this chapter are thus devoted to the description of several contributions to the mechanical characterization of materials making use of various optical imaging techniques.

2 Experimental developments

This section describes the experimental techniques developed in order to achieve a mechanical characterization of thin film materials at a very small scale. Dealing with essentially planar structures, one may wish to focus on structures that mostly deform either out-of-plane or in-plane. These options are not mutually exclusive, but the following subsections detail distinct set-ups encoding out-of-plane or in-plane displacements separately.

The first subsection focuses on an imaging set-up that is tailored to measure surface rotations instead of the surface out-of-plane displacements. This limits the differentiations required to estimate an experimental deformation and it is shown to be of particular

interest when dealing with small structures or probed volumes. The second subsection describes a lithographic procedure to pattern surfaces that do not naturally produce contrasted images, thus making DIC applicable. It is also shown that the pattern may be tailored to make the in-plane displacement field measurement easier under particular constrains.

2.1 Surface rotation measurement

This subsection describes a polarized light imaging interferometer to measure the rotation field of reflecting surfaces [177]. This set-up is based on a home-made prism featuring a birefringence gradient. The arrangement is presented before focusing on the home-made prism and its manufacturing process. The dependence of the measured optical phase on the rotation of the surface is derived, thus highlighting the key parameters driving the sensitivity. The system capabilities are illustrated by imaging the rotation field at the surface of a tip-loaded polymer specimen.

Many imaging interferometric systems can be utilized to measure a displacement field, such as compensated interferometers described by Françon or Nomarski [178] employing a Savart polariscope or a Wollaston prism, respectively [179]. It is worth noting that the latter features a usually overlooked rotation sensitivity [153], and that such a rotation sensitivity is of major interest when downsizing tested volumes or samples:

- Let us consider Boussinesq's problem [180] as the prototype of very local characterization. Applying a point load on an elastic half-space, the surface displacement field $w(r)$ scales as $1/r$ (with r: the in-plane distance between the loading point and the point of interest) and is therefore very confined. The surface rotation $\theta(r)$ thus scales as $w(r)/r$ and may reach experimentally accessible values since r is very small, even though the maximum displacement amplitude (under the tip) is kept vanishingly small in order to probe a tiny volume. It would seem wise to measure the rotation field instead of the out-of-plane displacement field.

- The same conclusion applies to vanishingly small structures such as microcantilevers. Considering a clamped-free beam (of length L) with a constant curvature, the maximum out-of-plane displacement scales as L^2 while the rotation scales as L. As a consequence, if L decreases, the out-of-plane displacement decreases faster than the rotation. In the case of micro or even nano-system, it thus becomes interesting to measure a rotation rather than a displacement.

Many interferometric [181, 182, 183, 184] or non interferometric [185] systems have been devised in the past to allow for a pointwise angular measurement. For mechanical engineering applications, imaging techniques such as deflectometry [186] are available to provide rotation maps. At the macro-scale, this is already extremely useful since it avoids one differentiation (which consists of applying a high-pass operator) in the data treatment, compared to a displacement measurement.

This subsection therefore describes a polarized-light imaging interferometer derived from the one already proposed to measure out-of-plane displacement fields [153]. The set-up is based on a home-made prism featuring a birefringence gradient. The device and the interference pattern are described. The manufacturing process for the prism is then detailed. The dependence of the measured optical phase on the rotation of the surface is exhibited and the key parameters driving its rotation sensitivity are highlighted. An example for the practical calibration of the set-up is given. Finally, an example with a micro-tip pressing onto a polymer (PDMS) sample demonstrates the ability of the proposed set-up, which is combined with a phase-stepping method, to catch localized phenomena. Detailed calculations describing the effect of the numerical aperture [187, 188, 190, 189] are presented in Ref. [177].

2.1.1 Experimental set-up

A schematic view of the interferential microscopy imaging set-up is shown in FIG.1.1. The device is based on a home-made prism, featuring an uniaxial birefringence gradient. The light source is a spatially incoherent light-emitting diode (LED, λ = 627 nm), which is used to illuminate a polarizing beam splitter. The polarizing beam splitter is mounted so that the reflected beam is polarized at 45° of the gradient direction (**y**) of the birefringent prism. The prism splits the beam into two orthogonally polarized beams with a small angle between each other. One of these beams is polarized orthogonally to the plane Π defined by the optical axis of the system and the gradient direction of the prism (**y**), and will be referred to as transverse electric (TE) beam. The other one is polarized in the plane Π, and will be referred to as transverse magnetic (TM) beam. These beams are focused on the sample by an objective lens. After reflection on the sample and recombination by the birefringent prism, the beam goes through the polarization beam splitter, which thus behaves as a polarizer orthogonal to the entrance one. The transmitted beam is finally focused on a CCD array (DALSA 1M30, 1024 $\times$ 1024 pixels, 12 bits) that records the interference pattern. As the set-up is illuminated using a light-emitting diode, the interference pattern reads [153]

$$I = I_0 + A\cos(\phi + \pi) \tag{1.1}$$

where ϕ is the phase shift between the TM and TE polarization components.

2.1.2 Home-made birefringent prism

The key element in the imaging set-up is the birefringent prism. The (O_1xy) plane corresponds to the entrance surface of the prism. A heterogeneous stress state is frozen in the material to induce a heterogeneous birefringence state. To set a uniaxial stress gradient of the σ_{xx} component along **y**, it is necessary to induce a homogeneous bending moment in the prism.

In practice, the prism is made out of PS-8A epoxy resin (Vishay Micro-Measurements). A test sample is machined from the polymer plate and then heated up above its glass tran-

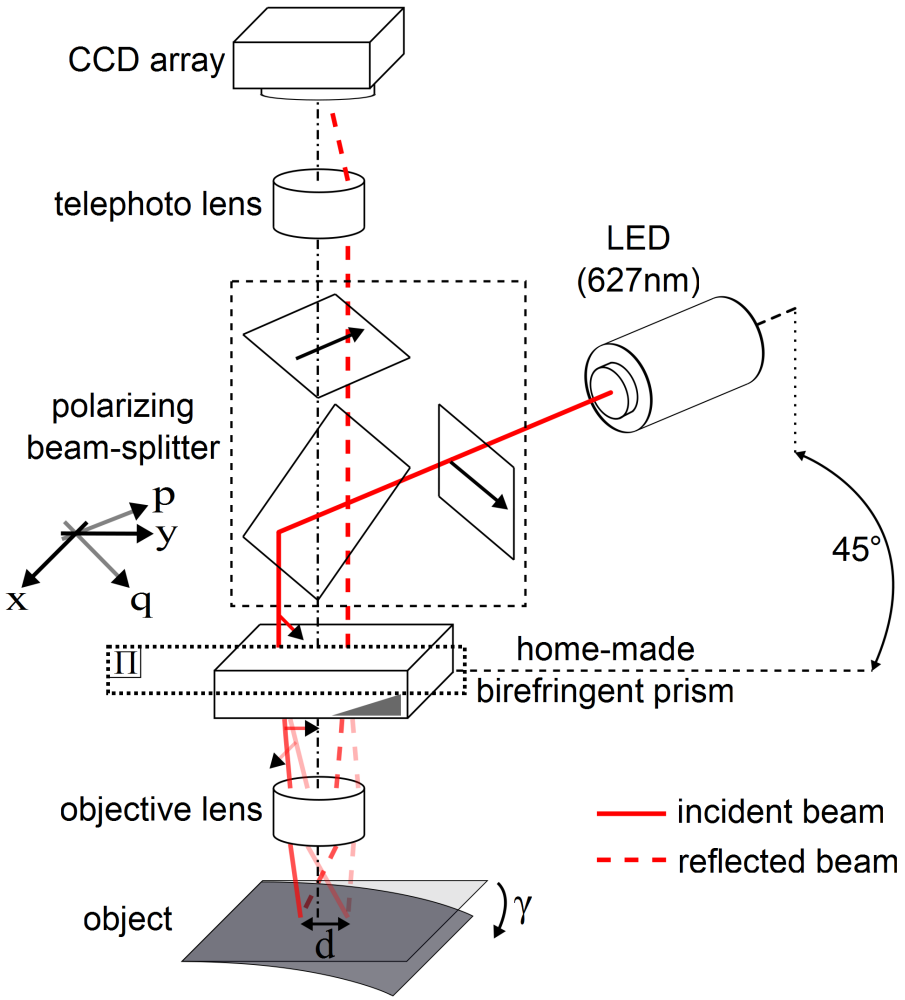

Figure 1.1: Schematic view of the interferometric imaging set-up.

sition temperature ($T_g \simeq 85$ °C). It then undergoes an off-axis tensile test, described in FIG.1.2. The test sample is finally cooled at room temperature when maintaining the applied force to freeze the birefringence state in the prism. The prism is cut out of the specimen gauge section. By tailoring the specimen geometry and loading, it is possible to obtain a wide range of values for the birefringence gradient. Using beam theory, the stress tensor $\underline{\underline{\sigma}}$ in the prism reads

$$\underline{\underline{\sigma}} = \begin{pmatrix} Gy & 0 & 0 \\ 0 & 0 & 0 \\ 0 & 0 & 0 \end{pmatrix}_{(x,y,z)} \tag{1.2}$$

where G denotes the stress gradient. For the description of the prism, let us denote Π_0 the plane such as $\sigma_{xx}(y) = 0$. Let us describe the prism in the plane (O_1yz) where O_1 is the intersection between the y axis and the plane Π_0. (O_1yz) is assumed to be made coincident with the plane Π.

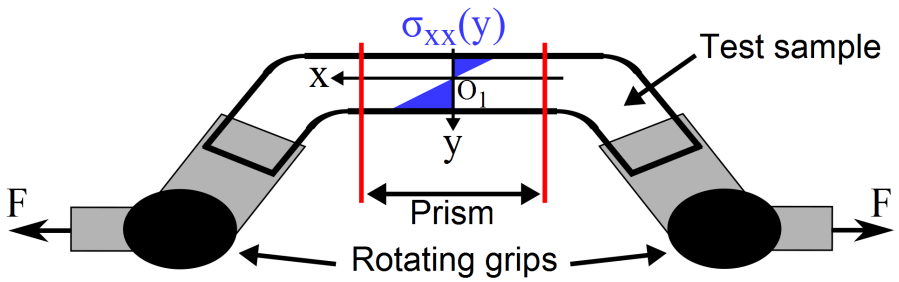

Figure 1.2: Arrangement used to establish a stress gradient in the sample.

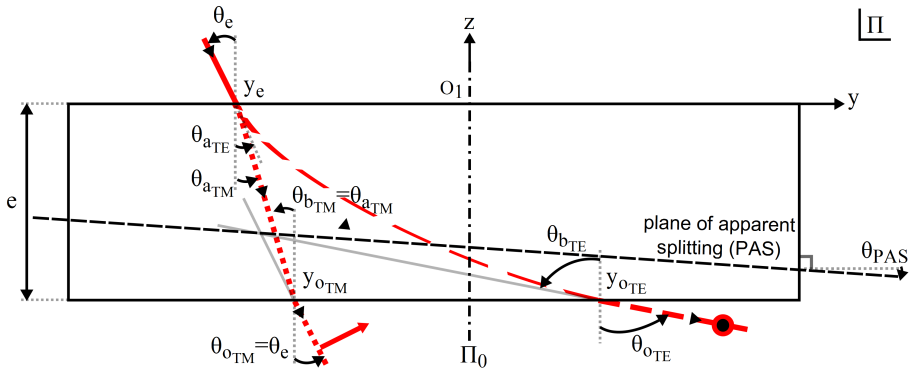

Figure 1.3: Ray tracing in the prism.

The frozen uniaxial stress gradient results in a refractive index gradient in the prism. Initially, the unstressed material has a refractive index $n^* = 1.5$ for both TE and TM rays. As a consequence of the arrangement described in FIG.1.2, TM rays are polarized in the y-direction. As σ_{yy} is equal to 0 everywhere, the TM index is equal to n^* for any entrance point ($n_{TM} = n^*$). TE rays are polarized in the x-direction so they experience refractive indexes modified by σ_{xx}. As σ_{xx} linearly depends on y, the TE index varies linearly with y. The TE refractive index thus reads

$$n_{TE} = n^* + C_b G y = n^* + c_{TE} y \tag{1.3}$$

where C_b is the photoelastic constant of the birefringent material. Using a 3 mm thick polymer plate, a birefringence gradient $c_{TE} \sim 0.1$ m^{-1} is achieved with the chosen material. FIG.1.3 shows (in the Π plane) the decomposition of an incident ray by the prism into two emerging rays. Assuming that the surrounding refractive index equals 1, the Snell-Descartes laws on the entrance interface of the prism read

$$\sin\theta_e = n_{TM} \sin\theta_{a_{TM}} = n_{TE}(y_e) \sin\theta_{a_{TE}} \tag{1.4}$$

where θ_e is the incidence angle, y_e the entrance point, $\theta_{a_{TE}}$ and $\theta_{a_{TM}}$ the angles of the refracted rays at the entrance interface. The Snell-Descartes laws for the exit interface of

the prism read

$$n_{TM}\sin\theta_{b_{TM}} = \sin\theta_{o_{TM}} = \sin\theta_e \tag{1.5}$$
$$n_{TE}(y_{o_{TE}})\sin\theta_{b_{TE}} = \sin\theta_{o_{TE}} \tag{1.6}$$

where $y_{o_{TE}}$ is the exit point for the TE ray. $\theta_{b_{TE}}$ and $\theta_{b_{TM}}$ are the incidence angles at the exit interface for TE and TM rays respectively. $\theta_{o_{TE}}$ and $\theta_{o_{TM}}$ are the emerging angles for TE and TM rays respectively. The relationship between entrance and exit angles of the prism for the TE ray is given by the eikonal equation and reads

$$\theta_{b_{TE}} = \theta_{a_{TE}} + \varepsilon + o\left(\theta_{a_{TE}}^3, \varepsilon^3\right) \tag{1.7}$$

with:

$$\varepsilon = \frac{c_{TE}e}{n_{TE}(y_e)} \simeq 3\times10^{-4}\ \text{rad} \tag{1.8}$$

It depends on the thickness of the prism ($e = 3$ mm), birefringence gradient and TE rays refractive index at the entrance point. ε represents the deflection of the TE ray inside the prism by the birefringence gradient. For the TM ray, the exit point $y_{o_{TM}}$ reads

$$y_{o_{TM}} = y_e + e\tan\theta_{a_{TM}} \tag{1.9}$$

The relationship between entrance and exit points of the prism for the TE ray is also given by the eikonal equation and reads

$$y_{o_{TE}} = y_e + e\left(\theta_{a_{TE}} + \frac{\varepsilon}{2}\right) + o\left(\theta_{a_{TE}}^3, \varepsilon^3\right) \tag{1.10}$$

The separation between TE and TM rays reads

$$\theta_{o_{TE}} - \theta_{o_{TM}} = c_{TE}e + o\left(\theta_e^3, \varepsilon^3\right) \sim 10^{-4}\ \text{rad} \tag{1.11}$$

It only depends on the thickness of the prism and the birefringence gradient. Further developments will be made easier by defining the plane of apparent splitting (PAS, see FIG.1.3). For an incident ray, it corresponds to the points where TE and TM rays appear to split. The equation of the PAS reads

$$z = \tan(\theta_{PAS})y - e\left[1 - \frac{1}{2n^*}\right] + o\left(\theta_e^2, \varepsilon^2, (c_{TE}y_e)^2\right) \tag{1.12}$$

with:

$$\theta_{PAS} = \frac{ec_{TE} + 2\theta_e}{2n^{*2}} + o\left(\theta_e^2, \varepsilon^2, (c_{TE}y_e)^2\right) \tag{1.13}$$

where θ_{PAS} is the angle between PAS and surface of the prism (see FIG.1.3). Taylor expansion with respect to $c_{TE}y_e$ is possible because $c_{TE}y_e \ll n^*$ in the expression of ε (see Eq. (1.8)).

For the TM ray, the refractive index is constant, so that the optical length L_{TM} reads

$$L_{TM} = n^* \frac{e}{\cos\theta_{a_{TM}}} = \frac{n^{*^2} e}{\sqrt{n^{*^2} - \sin^2\theta_e}} \tag{1.14}$$

The optical path length for the TM ray thus depends on the incidence angle (see FIG.1.3) but does not depend on the entrance point. For the TE ray, the optical path length reads

$$L_{TE} = \int_{-e}^{0} \frac{n_{TE}(y_{TE}(z))}{\cos(\theta_{TE}(z))}\,\mathrm{d}z \tag{1.15}$$

with:

$$y_{TE}(z) = y_e - z\left(\frac{\theta_e}{n_{TE}(y_e)} - \frac{\varepsilon z}{2e}\right) + o\left(\theta_e^3, \varepsilon^3\right) \tag{1.16}$$

$$\theta_{TE}(z) = \frac{\theta_e}{n_{TE}(y_e)} - \frac{\varepsilon z}{e} + o\left(\theta_e^3, \varepsilon^3\right) \tag{1.17}$$

The optical path length for the TE ray finally reads

$$L_{TE} = e\left[n_{TE}(y_e)\left(1 + \frac{\varepsilon^2}{6}\right) + \frac{c_{TE} e}{6}\varepsilon + \varepsilon\theta_e + \frac{\theta_e^2}{2n_{TE}(y_e)}\right] + o\left(\theta_e^3, \varepsilon^3\right) \tag{1.18}$$

so that L_{TE} depends on both the incidence angle θ_e and the entrance point y_e.

2.1.3 Optical phase

Let us assume that the optical phase difference ϕ due to the path prism-objective-sample-objective-prism can be decomposed as $\phi = \phi_p + \phi_o$ where ϕ_p denotes the part arising from the birefringent prism and ϕ_o the contribution due to the object.

FIG.1.4 presents the full ray tracing for the two emerging rays of FIG.1.3. δ_{PAS} and α_{PAS} are the position and the rotation of the actual PAS with respect to the rear focal plane of the objective lens, respectively. The point O_2 is the intersection of the PAS with the optical axis. It is the origin of the frame (O_2YZ). Z is made coincident with the optical axis and Y lies in the Π plane. Δ is the distance between O_2 and O_1 projected onto Y (if $\Delta = 0$, O_1 and O_2 belong to the optical axis). γ_{TE} and γ_{TM} define the surface orientation for the TE and TM rays, respectively. The two rays emerge from the PAS at the point whose orthogonal projection on the Y axis is Y_{PAS}. Then, they travel through the objective, are reflected by the sample and intersect the PAS at $Y'_{PAS_{TE}}$ and $Y'_{PAS_{TM}}$

$$\begin{aligned} Y'_{PAS_i} &= -Y_{PAS} - 2\frac{f_o^2 + Y_{PAS_i}^2}{f_o}\gamma_i - 2\left[\alpha_{PAS} + \left(1 + \frac{1}{n^{*^2}}\right)\theta_e + n^*\varepsilon + \frac{e c_{TE}}{2n^{*^2}}\right]\delta_{PAS} \\ &\quad + o\left(\alpha_{PAS}^2, \theta_e^2, \theta_{PAS}^2, \varepsilon^2, \gamma_i^2\right) \end{aligned} \tag{1.19}$$

where i stands for TE or TM.

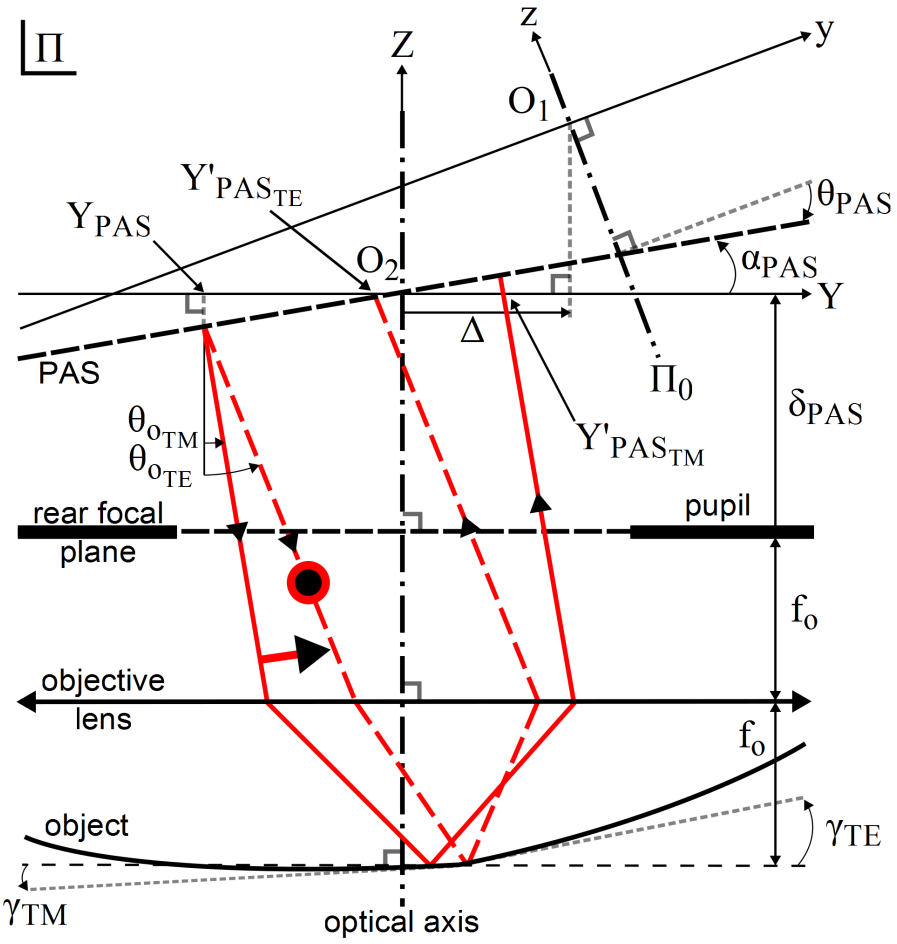

Figure 1.4: Ray tracing through the objective for the two emerging rays of FIG.1.3.

The position of Y'_{PAS_i} depends on the position of Y_{PAS}, on the objective focal length f_o, on the incidence angle θ_e, on PAS position (δ_{PAS} , α_{PAS}) and on the corresponding surface orientation (γ_i). As described in equation (1.18), the optical path length in the prism for the TE ray depends on the entrance point. For the back TE path, this entrance point ($Y'_{PAS_{TE}}$) depends on γ_{TE}, so that the back optical path length in the prism for TE ray depends on γ_{TE}. Eq. (1.14) indicates that the optical path length in the prism for the TM ray only depends on the incidence angle and does not depend on the entrance point. As a consequence the optical path length in the prism for the TM ray is independent of the TM orientation of the sample γ_{TM}. Finally, the total optical phase depends on γ_{TE}. It demonstrates how the system is sensitive to the TE orientation of the sample and insensitive to TM. The TM beam will thus act as a reference beam in the interferometer. The total optical path length arising from the birefringent prism is the difference between the optical path length for TE and TM rays

$$\phi_p(\gamma_{TE}) = \frac{2\pi}{\lambda}\{[L_{TE_{\text{forth}}} + L_{TE_{\text{back}}}(\gamma_{TE})] - [L_{TM_{\text{forth}}} + L_{TM_{\text{back}}}]\} \tag{1.20}$$

Using equations (1.14), (1.18) and (1.20) and first-order Taylor expansions with respect to α_{PAS}, θ_e, θ_{PAS}, ε and γ_{TE}, the difference between the optical path length for TE and TM rays reads

$$\phi_p = \phi_{\gamma_{TE}} + \phi_{\theta_e} + \phi_\Delta + \phi_r \tag{1.21}$$

with

$$\begin{aligned}
\phi_{\gamma_{TE}} &= -\frac{4\pi}{\lambda} c_{TE} e \frac{f_o^2 + Y_e^2}{f_o} \gamma_{TE} + o\left(\gamma_{TE}^2\right) && (1.22)\\
\phi_{\theta_e} &= -\frac{2\pi}{\lambda} c_{TE} e \left[2\left(1 + \frac{1}{n^{*2}}\right)\delta_{PAS} + \frac{e}{n^*}\right]\theta_e + o\left(\theta_e^2, \theta_{PAS}^2\right) && (1.23)\\
\phi_\Delta &= -\frac{4\pi}{\lambda} c_{TE} e \Delta + o\left(\theta_{PAS}^2\right) && (1.24)\\
\phi_r &= -\frac{2\pi}{\lambda} c_{TE} e \left[\left(2\alpha_{PAS} + \frac{c_{TE} e}{n^{*2}}\right)\delta_{PAS} + \left(2n^*\delta_{PAS} - \frac{e}{3}\right)\varepsilon\right] \\
&\quad + o\left(\alpha_{PAS}^2, \theta_{PAS}^2, \varepsilon^2\right) && (1.25)
\end{aligned}$$

where Y_e denotes the entrance point on the prism (on Y axis). Δ can be changed by translating the prism so it will be used for phase modulation.

The rotation sensitivity $\frac{\partial \phi}{\partial \gamma_{TE}}$ depends on the thickness of the prism e and on the birefringence gradient c_{TE}. It also increases with the objective focal length f_o and with the prism entrance point Y_e. Therefore equation (1.21) is only valid for a ray. For the full beam, the rotation sensitivity depends on the objective numerical aperture [177]. In addition, expanding (1.21) up to the second order shows the rotation sensitivity dependence on the incidence angle and on implementation defects is negligible. Finally, the lateral shear d between TE and TM rays on the sample (see FIG.1.1) reads

$$d = f_o c_{TE} e + o\left(\theta_e^2, \theta_{PAS}^2, \alpha_{PAS}^2, \varepsilon^2\right) \tag{1.26}$$

It depends on the objective focal length f_o as well as on the thickness of the prism and birefringence gradient. d corresponds to the separation, in the Y-direction, between the two reflected images of the sample due to the birefringence.

In addition to ϕ_p, there is also a phase contribution arising from the object. Let us consider the case of a tilted and stepped sample (of height $\Delta Z = Z_{TE} - Z_{TM}$), where TE and TM rays are reflected at different heights. According to Fermat's principle, tilting the sample does not induce any additional phase difference in the objective-sample-objective path. However, the step induces an additional phase ϕ_o that reads (assuming the ambient refractive index of the medium is 1)

$$\phi_o = -\frac{4\pi}{\lambda} \Delta Z \cos\alpha \tag{1.27}$$

where α is the incidence angle on the sample. α spans the full range defined by the objective entrance pupil, so that for the full beam ϕ_o, an integration over α has to be considered [177].

2.1.4 Calibration and example

As the parameters driving the phase sensitivity to the topography depend on the numerical aperture and thus on the illumination, a calibration procedure is desirable for practical applications. This section presents the calibration of the set-up and an example to validate both the system capabilities and its modeling.

The calibration consists of plotting interferograms obtained by tilting a planar sample. A PDMS sample, charged with 50wt% of Co nano-particles, is tilted from $\delta\gamma = -5^\circ$ to 5° by 0.05° steps with respect to the (unknown) initial stage orientation γ_d. Intensity images are acquired for each tilt value. This experiment gives one interferogram per pixel, which are used to retrieve modeling parameters. For the calibration, the phase equation for one ray [177] is recast:

$$\phi(K, \gamma_d + \delta\gamma, \Psi, \alpha) = -K[1 + \sin^2(\alpha)][\gamma_d + \delta\gamma] + \Psi \tag{1.28}$$

with

$$K = \frac{4\pi}{\lambda} c_{TE} e f_o \tag{1.29}$$

$$\gamma_d + \delta\gamma = \gamma_{TE} = \gamma_{TM} \tag{1.30}$$

$$\Psi = \phi_{\theta_e} + \phi_\Delta + \phi_r \tag{1.31}$$

where Ψ represents the phase contribution which is independent of γ_{TE}, as the contribution (1.27) from the object vanishes in this configuration. Because of the dependence on θ_e, Ψ reads

$$\Psi = \Psi_a Y + \Psi_b \tag{1.32}$$

with

$$\Psi_a Y = \phi_{\theta_e} \qquad \Psi_b = \phi_\Delta + \phi_r \tag{1.33}$$

Let us denote *NA* the numerical aperture of the objective lens. Taking the full aperture into account, equation (1.1) is modified by weighting and summing all useful rays of the light beam (see [177]) and the intensity equation reads

$$I(K, \gamma_d + \delta\gamma, \Psi, \gamma_c, NA, m) = I_0 + AF\left(\gamma_d + \delta\gamma, \gamma_c, NA, m, K, \Psi\right) \tag{1.34}$$

where F is the weighted sum of the contributions of each ray (some light rays are lost in the pupil of the objective, depending on the tilt), m a parameter used to describe the pupil illumination. It is used in the apodization function P_m that corresponds to the light distribution over the pupil ($P_m(\alpha) = [\cos(\alpha)]^m$). γ_c is used to account for negligible phenomena not taken into consideration in the model, such as the distance between the pupil

and the rear focal plane. It modifies the pseudo-period of the intensity with the tilt. For the sake of generality γ_c is assumed to depend on Y

$$\gamma_c = \gamma_{c_a} Y + \gamma_{c_b} \tag{1.35}$$

The involved parameters thus fall into two categories. The first one contains global parameters, which have the same value for all pixels: K, γ_d, NA, m, Ψ_a, Ψ_b, γ_{c_a} and γ_{c_b}. For the sake of brevity, these global parameters set is denoted $\}$ in the following. The second one contains the local parameters, which have a different value for each pixel: I_0 and A. Starting with a set of global parameters $\}$, the first step of the identification procedure consists of calculating $F(\},\delta\gamma)$ (as defined by Eq. 1.34) for all values of $\delta\gamma$. For each pixel (i,j) the local residual is defined as

$$R_0^2(\},I_0(i,j),A(i,j)) = \sum_{\delta\gamma} \{I_{\exp}(i,j,\delta\gamma) - [I_0(i,j) + A(i,j)F(\},\delta\gamma)]\}^2 \tag{1.36}$$

The optimal values $I_{0_{\text{optimum}}}(i,j)$ and $A_{\text{optimum}}(i,j)$ are obtained as the minimizers of the residual R_0^2. Using more than 2 different $\delta\gamma$ values, the stationarity condition yields an overdetermined linear system for each pixel. The description quality is then locally assessed through

$$R_1^2(\},i,j) = \min_{I_0(i,j),A(i,j)} R_0^2(\},I_0(i,j),A(i,j)) \tag{1.37}$$

A global residual taking in consideration residuals R_1^2 for every pixels and normalized to the measured intensities is then defined:

$$R_2^2(\}) = \frac{\sum_{i,j} R_1^2(\},i,j)}{\sum_{i,j}\sum_{\delta\gamma} [I_{\exp}(i,j,\delta\gamma)]^2} \tag{1.38}$$

The set of parameters $\}_{\text{optimum}}$ is retrieved as the minimizer of R_2^2, using the conjugate gradient algorithm. Let us define the final residual

$$R_3^2 = \min_{\}} R_2^2(\}) \tag{1.39}$$

where $\}_{\text{optimum}}, I_{0_{\text{optimum}}}(i,j), A_{\text{optimum}}(i,j)$ is then the set of fitted parameters. This calibration has to be performed after each modification of the set-up.

The interferograms for three different pixels, along the Y-direction, are displayed in FIG.1.6. The position of the interferogram center is controlled by Ψ. The attenuation of the signal with absolute tilt (upper envelope) is driven by NA, m and γ_d. The pseudo-period depends on NA, K and γ_c. The experimental, identified global and local parameter values, all calculated on 160 pixels regularly distributed along the 2 lines of FIG.1.7 (80 regularly spaced pixels by line) are given in TAB.1.1, 1.2 and 1.3, respectively. The comparison between the fitted and the experimental values shows that the fitted value of NA

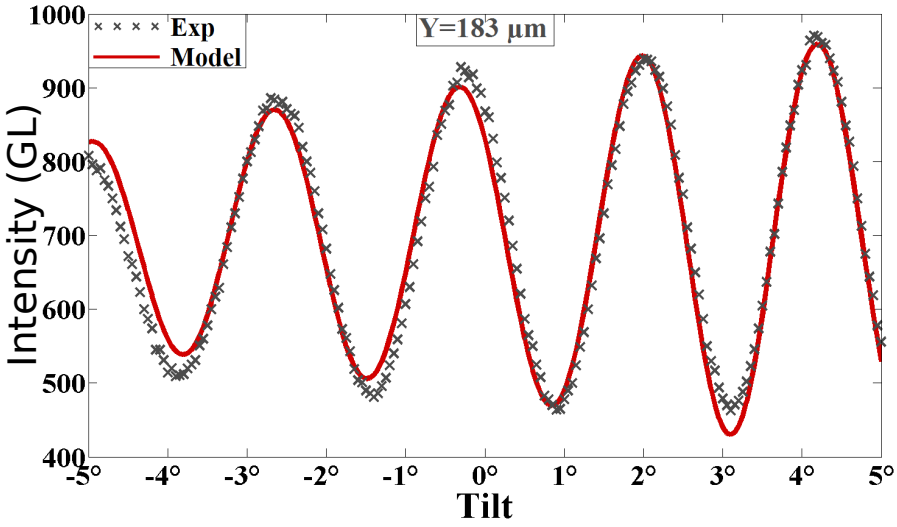

Figure 1.5: Tilting sample interferograms for $Y = 183\ \mu$m and for $\delta\gamma \in [-5°, 5°]$.

is the same as the experimental one within 2.4%. m vanishes so the light distribution over the pupil is almost homogeneous. The retrieved value for K is lower than the estimated one, it is thought to result (to a large extent) from c_{TE} which is estimated with an uncertainty of almost 10%. The identified initial stage misorientation γ_d is about 3.7° which is a realistic value because the surfaces of the sample are not parallel. Finally, the residual R_3^2 is about 2.31×10^{-3} thereby proving the identification quality.

Table 1.1: Estimated parameters.

LED		**Objective lens**	
$\boldsymbol{\lambda}$ (nm)		$\mathbf{f_o}$ (mm)	**NA**
627		20	0.45
Prism		**Rotation sensitivity**	
$\mathbf{c_{TE}}$ (m^{-1})	**e** (mm)	**K** ($rad.rad^{-1}$)	
0.139	3	167	

Table 1.2: Fitted global parameters.

NA	**m**	**K** ($rad.rad^{-1}$)
0.439	2.78×10^{-4}	147
γ_{c_a} ($rad.\mu m^{-1}$)	γ_{c_b} (rad)	γ_d (rad)
2.30×10^{-4}	0.117	-6.45×10^{-2}
Ψ_a ($rad.\mu m^{-1}$)	Ψ_b (rad)	$\mathbf{R_3^2}$
-1.87×10^{-2}	4.82	2.31×10^{-3}

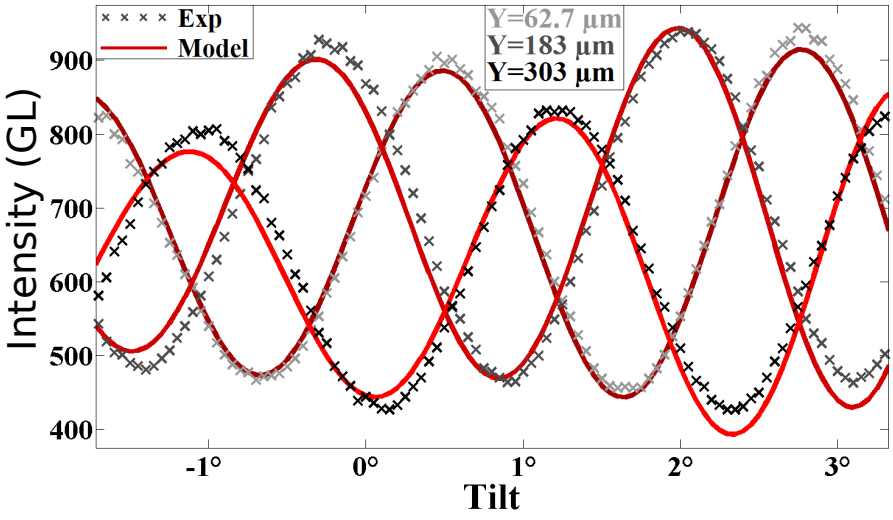

Figure 1.6: Tilting sample interferograms for $Y = \{62.7, 183, 303\}\mu$m, $\delta\gamma \in [-2°, 3°]$.

Table 1.3: Fitted local parameters.

Interferogram	**X** (μm)	**Y** (μm)	$\mathbf{I_0}$ (GL)	**A** (GL)	Ψ (rad)	γ_c (rad)
(a)	42.5	62.7	672	234	3.65	0.132
(b)	42.5	183	695	251	1.40	0.160
(a)	42.5	303	620	224	-0.853	0.187

The Δ-sensitivity $\left(s_\Delta = \frac{\partial\phi}{\partial\Delta}\right)$ will be used in the following for phase modulation and has thus to be estimated. It is proposed to change Δ from a known value $\delta\Delta$ ($\delta\Delta = 0.5$ mm) and to reproduce the above-described calibration experiment. For this second calibration, global parameters are set to the previously identified values $\}_{\text{optimum}}$, except the parameter Ψ_b which is changed to Ψ'_b

$$\Psi'_b = \phi_{\Delta+\delta\Delta} + \phi_r = \Psi_b + \phi_{\delta\Delta} = \Psi_b + s_\Delta \delta\Delta \tag{1.40}$$

where Ψ_b is the homogeneous part of the γ_{TE}-independent contribution of the phase. The calibration procedure is the same as above but the last minimization is performed with respect to Ψ'_b instead of the full set p. For the actual set-up (experimental parameters values are given in in TAB.1.1), one obtains

$$s_{\Delta_{\text{th}}} = -\frac{4\pi}{\lambda} c_{TE} e \simeq -8.36 \times 10^3 \text{ rad.m}^{-1} \tag{1.41}$$

$$s_{\Delta_{\text{exp}}} = \frac{\Psi'_b - \Psi_b}{\delta\Delta} \simeq -6.66 \times 10^3 \text{ rad.m}^{-1} \tag{1.42}$$

The difference between the theoretical and the experimental values is, to a large extent,

due to c_{TE} as it is consistent with the error on K

$$K_{\text{th}} = \frac{4\pi}{\lambda} c_{TE} e f_o \simeq 167 \text{ rad.rad}^{-1} \tag{1.43}$$

$$K_{\text{exp}} \simeq 147 \text{ rad.rad}^{-1} \tag{1.44}$$

$$\frac{K_{\text{th}}}{|s_{\Delta_{\text{th}}}|} = f_o = 20 \text{ mm} \tag{1.45}$$

$$\frac{K_{\text{exp}}}{|s_{\Delta_{\text{exp}}}|} \simeq 22.1 \text{ mm} \tag{1.46}$$

The value of Δ-sensitivity can be compared with the parameter K. The identification is consistent because the ratios (theoretical and experimental) between the 2 parameters give the same value to within 10% error, thereby proving the slight discrepancy obtained on K results from the product $c_{TE}e$. In addition, the value of the shear d (Eq. (1.26)) is compared with the parameter K. d is obtained by measuring the separation between the 2 superimposed pictures on an intensity image. One obtains $d_{\text{exp}} \simeq 7.86\ \mu$m, which should be compared to $d_{\text{th}} = c_{TE} e f_o = 8.34\ \mu$m. Considering the ratios

$$\frac{K_{\text{th}}}{d_{\text{th}}} = \frac{4\pi}{\lambda} \simeq 20.0\ \mu\text{m}^{-1} \tag{1.47}$$

$$\frac{K_{\text{exp}}}{d_{\text{exp}}} \simeq 18.7\ \mu\text{m}^{-1} \tag{1.48}$$

The identification is consistent with a discrepancy in $c_{TE}e$ because the ratios (theoretical and experimental) between the 2 parameters give the same value with a 6.5% difference. The goal is to measure the rotation field around a tip (of radius $\sim 10\ \mu$m) which presses onto a sample. The validation experiment consists of pressing a tip onto the previously described specimen.

The considered phase-stepping method makes use of 4 pictures obtained for $\Delta_k = [0, 0.1, 0.2, 0.3]$ mm. Using equation (1.1) to approximate the intensity (a small range of tilt is swept so interferograms remain similar to a sine curve), the measured intensities read

$$I_{\text{exp}}(i, j, \Delta_k) = I_0(i, j) + A(i, j) \cos[\phi(i, j) + s_\Delta \Delta_k] \tag{1.49}$$

Eq. (1.49) therefore yields 4 equations per pixel for only 3 unknowns ($I_0(i, j)$, $A(i, j)$ and $\phi(i, j)$), so that ϕ is obtained by solving it in a least-squares sense.

A phase map example is presented in FIG.1.7. It is obtained when pressing a tungsten tip (of radius $= 30\ \mu$m) onto an opaque sample made of PDMS, charged with 50wt% of Co nano-particles (sample thickness $\simeq 2.6$ mm). The noise is estimated by making 2 identical phase maps and averaging the norm of their difference. The noise on phase ϕ_{noise} is estimated to be 8.9×10^{-3} rad. The phase map is described in the $(O_T X_T Y_T)$ plane, with O_T the tip loading point. X_T and Y_T are oriented as X and Y. Let us consider the phase along the Y_T axis in 2 different parts of the phase map. The first one corresponds to

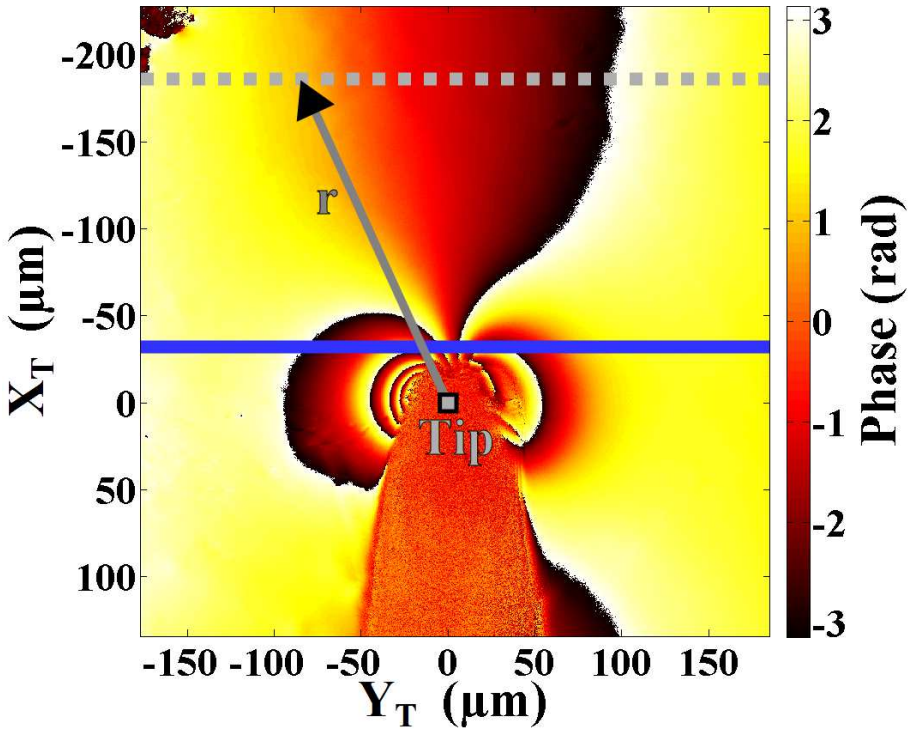

Figure 1.7: Phase map obtained when pressing a tip onto a PDMS sample.

the zone far from the tip (dotted line in FIG.1.7) where the sample is not deformed. The phase is linear with respect to Y_T (circles in FIG.1.8), as a result of the dependence on the incidence angle (θ_e). It corresponds to the parameter Ψ presented in the calibration subsection. The phase equation reads

$$\phi_{\text{far from the tip}} = \phi_{\theta_e} + \phi_\Delta + \phi_r = \Psi_a Y + \Psi_b = \Psi \tag{1.50}$$

The theoretical phase far from the tip shown in FIG.1.8 is as obtained from the calibration, along the Y_T axis. The good agreement validates the proposed modeling. The crosses in FIG.1.8 correspond to a zone (solid line in FIG.1.7) where the sample is deformed by the tip so the γ_{TE}-contribution of the optical phase is activated. The presence of a phase deviation from the previous line in the vicinity of the tip, shows the presence of the rotation field in the Y-direction. This phase map proves that the system allows one to measure the rotation field of localized phenomena (here, a few tens of micrometer). Let us assume that the situation corresponds to the problem of Boussinesq [180]. In this case the displacement w scales as $w(X_T,Y_T) = -P/(\pi E^* r)$ (with $r = \sqrt{X_T^2 + Y_T^2}$: the in-plane distance between the loading point and the point of interest, see FIG.1.7, P the loading force onto the sample and $E^* = E/(1-\nu^2)$ the biaxial Young's modulus of the sample) and the rotation θ as $\theta(X_T,Y_T) = P/(\pi E^* r^2)$. The measured rotation field scales as $\gamma_{TE}(X_T,Y_T) = PY_T/(\pi E^* r^3)$ and the contribution from the object scales as $\Delta Z(X_T,Y_T,d) = w(X_T,Y_T) - w(X_T,Y_T-d)$, because the measurement is only made in the

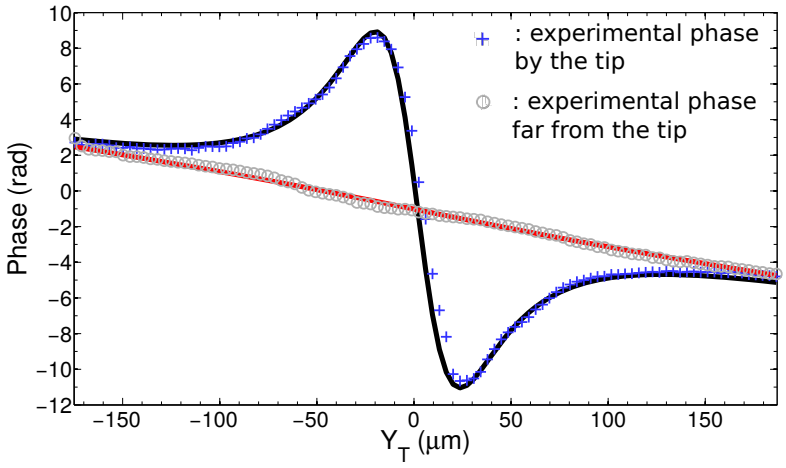

Figure 1.8: Phases along Y_T axis (see FIG.1.7). Solid lines: theoretical phases.

Y-direction. Finally, the phase equation reads

$$\phi_{\text{tip}} = \phi_{\theta_e} + \phi_\Delta + \phi_r + \phi_{\gamma_{TE}} + \phi_o \tag{1.51}$$

$$= \Psi_a Y + \Psi_b + \frac{\partial \phi}{\partial \gamma_{TE}} \gamma_{TE}(X_T, Y_T) + \frac{\partial \phi}{\partial \Delta Z} \Delta Z(X_T, Y_T, d) \tag{1.52}$$

The solution of Boussinesq's problem (solid line close to the tip in FIG.1.8) nicely fits the measured phase, thereby demonstrating the ability of the set-up to catch a localized phenomenon.

2.1.5 Optimal spectral domain

As detailed in Sect. 2.1.3, the described optical set-up is sensitive to both surface displacements and surface rotations. As these two quantities are not independent, a criterion has to be defined, for a given displacement field space, in order to make sure that the set-up is used at its best.

Let us use an approach very similar to the one used to study the spatial resolution of imaging devices, and consider the displacements family $w(Y)$ defined by

$$w(Y) = w_0(\kappa) \sin\left(\frac{2\pi}{\kappa} Y\right) \tag{1.53}$$

where $w_0(\kappa)$ is the amplitude for the wavelength κ.

Let us define $\phi_{\gamma_{TE_{RMS}}}$ as the RMS contribution of the surface rotation to the measured phase

$$\phi_{\gamma_{TE_{RMS}}} = \lim_{Y_0 \to +\infty} \sqrt{\frac{1}{2Y_0} \int_{Y=-Y_0}^{Y=Y_0} \left\{ s_{\gamma_{TE}} \frac{\partial w(Y)}{\partial Y} \right\}^2 \mathrm{d}Y} \tag{1.54}$$

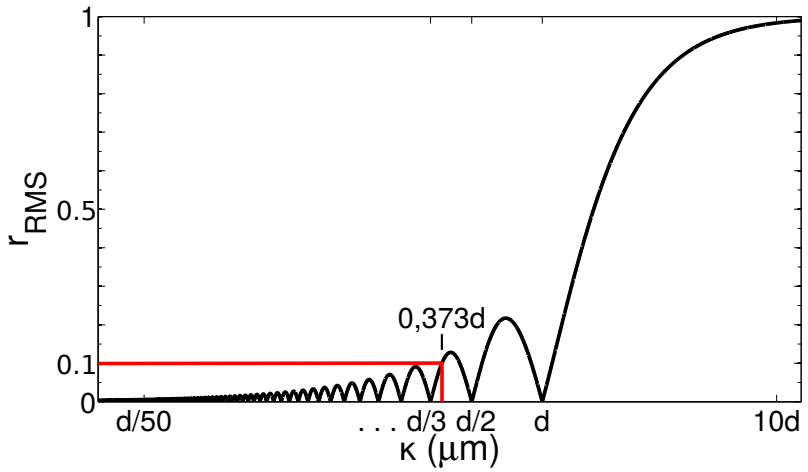

Figure 1.9: r_{RMS} as a function of the spatial wavelength κ.

and $\phi_{\Delta Z_{RMS}}$ the RMS contribution of the surface displacement to the measured phase

$$\phi_{\Delta Z_{RMS}} = \lim_{Y_0 \to +\infty} \sqrt{\frac{1}{2Y_0} \int_{Y=-Y_0}^{Y=Y_0} \{s_{\Delta Z}\,[w(Y) - w(Y-d)]\}^2 \,\mathrm{d}Y} \tag{1.55}$$

The ratio r_{RMS} thus compares the two contributions

$$r_{RMS} = \frac{\phi_{\Delta Z_{RMS}}}{\phi_{\gamma_{TE_{RMS}}}} \tag{1.56}$$

where $2Y_0$ is the considered length along Y, $s_{\gamma_{TE}} = \frac{\partial \phi}{\partial \gamma_{TE}}$ and $s_{\Delta Z} = \frac{\partial \phi}{\partial \Delta Z}$ are the phase sensitivities to γ_{TE} and ΔZ, respectively (see equations. (1.22) and (1.27)). Assuming that (see equation (1.26))

$$s_{\gamma_{TE}} s_{\Delta Z} \approx \frac{-\frac{4\pi}{\lambda} c_{TE} e f_o}{-\frac{4\pi}{\lambda}} \approx d \tag{1.57}$$

the ratio r_{RMS} reads

$$r_{RMS} = \frac{\kappa}{\pi d} \left| \sin\left(\frac{\pi d}{\kappa}\right) \right| \tag{1.58}$$

and is displayed as a function of the spatial wavelength κ in FIG.1.9.

It is clear from equation (1.58) that if $d = H\kappa$ with H an integer, then $r_{RMS} = 0$ so that the contribution from the displacement vanishes. The microscope thus only measures surface rotations, with a very useful sensitivity compared to other common-path imaging interferometers. For large κ values, r_{RMS} tends to 1, the two contributions are comparable so that a decoupling procedure has to be used to retrieve the underlying displacement field. Conversely, r_{RMS} tends to 0 for small wavelengths, making the proposed system particularly interesting. Keeping $r_{RMS} \in [0;0.1]$ allows one to define this optimal wavelength range as $\kappa \in [0;0.373d]$. This wavelength range thus depends on the shift d in

the object plane, which can be tailored, for a given application, by choosing the adequate prism (thickness e and index gradient c_{TE}) and the optimum objective focal length f_o.

2.1.6 Conclusion

The proposed set-up makes use of a birefringent prism whose fabrication procedure is presented. It allows one to have access to the rotation field of reflecting surfaces, projected onto a particular prism direction. It must be highlighted that the set-up is therefore well suited to localized phenomena. This method is particularly useful for situations where scale effects require the measurement of rotations instead of out-of-plane displacements. The noise on the phase measurement is estimated to be $\simeq 9\times10^{-3}$ rad without any image accumulation. As a consequence, it is thought to be useful to study the deformation of locally loaded samples. A detailed modeling including aperture effects is proposed, and a calibration procedure allows one to retrieve the parameters required by a quantitative use of the obtained phase maps. The ability of the set-up to catch localized mechanical phenomena is therefore demonstrated.

2.2 Surface patterning at the microscale

Whereas the set-up described in Sect. 2.1 is intended to map out-of-plane deformations, in-plane displacement fields may be of particular interest so that the translation of the patterning methods to reduced length scales has received some attention [133]. It should however be highlighted that MEMS devices are usually obtained as the result of successive additive/subtractive lithographic processes. As a consequence, and contrary to the macroscale for which random patterns are usually deposited, the lithographic nature of the process requires the deposited pattern to be user-defined. This section is therefore intended to show some of the key aspects of the measurement chain from the pattern processing to the DIC algorithm. Controlling this full measurement chain **may** be exploited to pattern the surface so that it will exhibit an optimal image when observed with the user-defined imaging device. The meaning of "optimal" in the previous sentence is application-specific, and is to be clarified after recalling the principles of DIC measurements and patterning methods.

2.2.1 DIC measurements

Let us consider that the displacement field $\mathbf{U}(\mathbf{x})$ is to be retrieved from two images of the device surface $f(\mathbf{x})$ (before loading) and $h(\mathbf{x})$ (during loading)

$$h(\mathbf{x}) = f(\mathbf{x}+\mathbf{U}(\mathbf{x})) \tag{1.59}$$

$\mathbf{U}(\mathbf{x})$ reads

$$\mathbf{U}(\mathbf{x}) = \mathbf{U_0}(\mathbf{x}) + \mathbf{u}(\mathbf{x}) \tag{1.60}$$

where $\mathbf{U_0}(\mathbf{x})$ is the previously determined, maybe large, displacement field. Assuming the amplitude of the displacement correction $\mathbf{u}(\mathbf{x})$ is small enough, Eq.(1.59) is rewritten:

$$h(\mathbf{x}) \simeq f(\mathbf{x}+\mathbf{U_0}(\mathbf{x})) + \nabla f(\mathbf{x}+\mathbf{U_0}(\mathbf{x})) \cdot \mathbf{u}(\mathbf{x}) \tag{1.61}$$

From Eq.(1.61) it is concluded that the displacement measurement is possible if the pattern gradient is nonzero along the displacement direction. A first rough attempt to optimize the used pattern $f(\mathbf{x})$ would then try to maximize the optical flow over the considered area Ω for a user-specified displacement field $\mathbf{U}_{test}(\mathbf{x})$, thus maximizing the indicator

$$\eta^2_{flow}(f(\mathbf{x}+\mathbf{U_0}(\mathbf{x})), \mathbf{U}_{test}) = \int_\Omega (\nabla f(\mathbf{x}+\mathbf{U_0}(\mathbf{x})) \cdot \mathbf{U}_{test}(\mathbf{x}))^2 d\mathbf{x} \tag{1.62}$$

This calls for three remarks:

- this calculation requires the user to define a specific displacement amplitude for which the pattern will be optimal;
- the optimization indicator should be insensitive to the initial position of the pattern in the field of view. This is easily achieved by considering the average

  $$\eta^2_{RBM}(f(\mathbf{x}), \mathbf{U}_{test}) = \left\langle \eta^2_{flow}(f(\mathbf{x}+\mathbf{U}_{RBM}(\mathbf{x})), \mathbf{U}_{test}) \right\rangle \tag{1.63}$$

  over the rigid body motions $\mathbf{U}_{RBM}$ spanning one pixel range in both directions;
- $f(\mathbf{x})$ results from the convolution of the pattern effectively deposited onto the surface $p(\mathbf{x})$ with the point-spread function of the imaging device, which has thus to be known.

2.2.2 Lithographic patterning process

The pattern $p(\mathbf{x})$ is typically to be obtained by locally depositing a metal layer to provide a locally higher surface reflectivity. This may be achieved by e-beam lithography (which is rather time-consuming) or by UV lithography. The latter is used for illustration purpose in the following. Slanted sidewalls are easily obtained using negative resists thus allowing for a lift-off deposition process. A positive resist can also be used for lift-off, provided a solvent gradient has been established through the resist thickness. Below is a recipe making use of such a positive resist and resulting from a rather crude optimization:

- Spin-coat a Ti-prime adhesion layer;
- Spin-coat S-1805 resist using 3000 rpm.s^{-1} and 4000 rpm.s^{-2};
- Soft bake for 1 min@ 80°C, using a hot-plate;
- Soak in toluene for 90s;
- Soft bake for 10 min@ 90°C, using the oven;

- Expose @ 35mJ.cm^{-2};
- Develop in M26A for 45s.

The full production process should be considered. 1 μm squares in the mask definition file yields 1.2 μm circular apertures in the mask (obtained using Heidelberg DWL200).

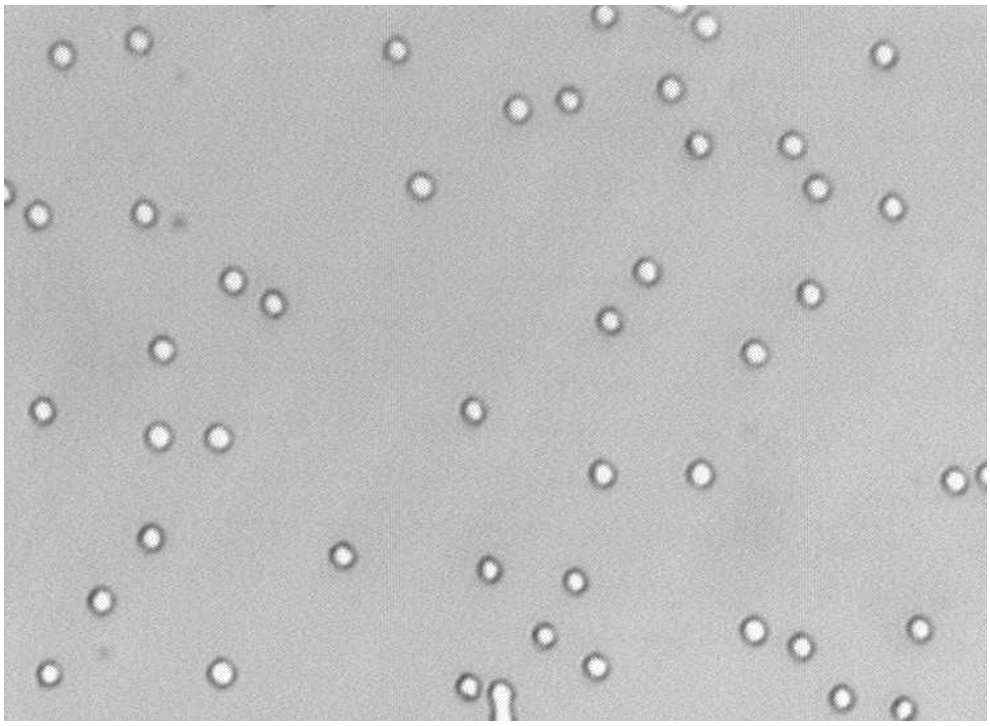

Figure 1.10: SEM image of 1.13μm gold spots obtained by lift-off with a positive resist.

FIG.1.10 shows an SEM image of gold spots obtained using such a mask with the above detailed recipe for a lift-off with a 100 nm thick Cr/Au layer. The average measured spots diameter is 1.13 μm. This diameter compares to the lateral resolution of optical microscopes in the visible range. This example thus illustrates the need to consider the full fabrication process, from the mask definition to the imaging system, in case this makes sense to optimize the deposited pattern.

2.2.3 Pattern optimization

As previously mentioned, MEMS devices differ from macroscopic mechanical devices by their ability to chemically interact with their environment. These interactions should not be altered by the deposited pattern, so that DIC measurements should be made for a minimal surface coverage. A trial and error approach is used to generate the pattern to be transferred. A master cell is first defined by computing the convolution of the elementary cell involved in building $p(\mathbf{x})$, *i.e.,* a 1.13 μm in diameter disk, with the point-spread

function corresponding to a diffraction-limited microscope, where the sample is illuminated with an optimal, partially coherent, monochromatic light source. Master cells are then randomly added to the mask definition, and guesses are kept so as to maximize the indicator η^2_{RBM} defined by Eq.(1.63) for instance. This may be achieved under various constrains, and one usually restricts the covered area to a user-defined fraction of the total area in order to minimize the hindrance of interactions with the environment. This thus defines the way patterns for DIC measurements are obtained in a microfabrication context.

3 Extended scanning microdeformation microscopy

Going back to the trade-off described in Sect. 1.2, the tools presented in the previous section are mainly intended to allow for displacement measurements on mechanical structures, which thus require some (maybe minimal) micro-sample manufacturing. One may conversely wish to very locally probe a larger, easy-handled specimen. Studying the relationships between deposition process parameters and material properties or controlling those in-line (just out of the furnace for instance) requires the characterization method to avoid any additional processing step.

Such approaches encompass acoustic microscopy [191], scanning probe microscopy [192, 193] and nanoindentation [194, 195]. Considering an isotropic material described by its Young's modulus E and Poisson's ratio ν, these techniques unfortunately only provide a combination of elastic parameters. Nanoindentation provides for example the measurement of the ratio $E/(1-\nu^2)$ (sometimes referred to as the indentation modulus), so that two techniques providing two different combinations of elastic parameters are necessary to determine both parameters. Bamber *et al.* [196, 197] for example combined acoustic microscopy and nanoindentation to estimate E and ν. Hurley *et al.* [198] proposed a method using atomic force microscope measurements obtained with flexural and torsional modes of vibration of the cantilever.

This section therefore describes the ways the scanning microdeformation microscope (SMM) [201, 202] has been extended to allow for a quantitative measurement of decoupled elastic constants of thin-film materials.

3.1 Scanning microdeformation microscope (SMM)

The scanning microdeformation microscope (SMM) [201, 202] is an AC-force contact microscope. The sensor is classically a micromechanical resonator composed of a rectangular silicon beam with a small sharp sapphire tip (curvature radius of severals tens of μm) at the end. The cantilever is glued onto a piezoelectric bimorph transducer at the other end. The transducer excites the vibration of the tip-sample system. The tip remains in contact with the sample and vibrates at several kHz with an amplitude in the nanometer

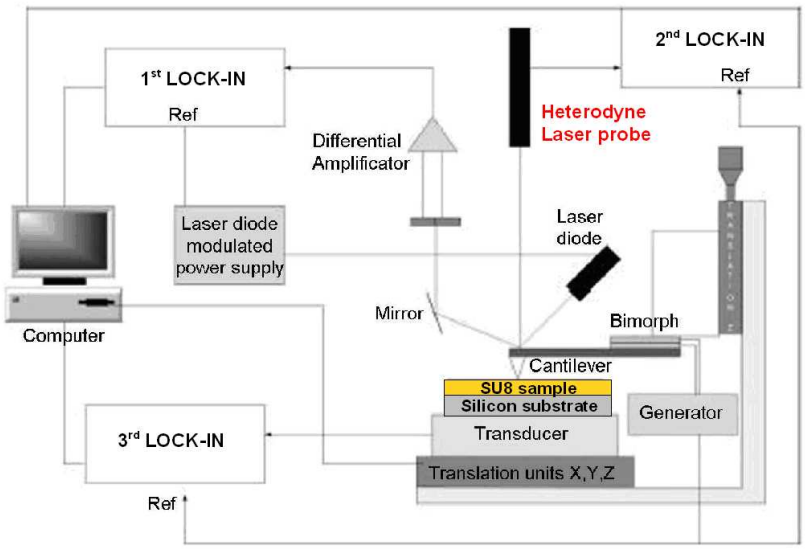

Figure 1.11: Schematic view of the SMM setup.

range. Amplitude and phase of the vibrating cantilever are measured with a high sensitivity heterodyne interferometer [203, 204] (FIG.1.11). The different components are described hereafter.

This arrangement has first been used to detect contact stiffness contrasts [202] or to measure the indentation modulus of the material under scrutiny by exploiting the first resonance frequency [205], and the conditions defining the optimal resonator stiffness for a given material to be probed have been derived [206].

3.1.1 Resonator

The resonator used herein is a 5.09 *mm* long silicon [100] cantilever beam with a trapezoidal cross-section. It is 125 μm thick, 431 μm in width on the tip side and 410 μm wide on the other side. Cyanoacrylate glue is used to assemble it to a sapphire tip whose dimensions are also measured by optical microscopy. The base cylinder is 398 μm in diameter and 265 μm long. The total tip length is 707 μm with a tip radius equal to 15 μm. The cantilever is also glued to a piezoelectric transducer (PSI-5H4E, Piezo System Inc) which is 0.86 *mm* thick, 8 *mm* long and 4 *mm* wide. The latter is glued to the support with a suspended length L_{PZT} (see FIG.1.12), which may be adjusted to tailor the first resonance frequency (typically a few kHz). It should be outlined that the overall resonator dimensions are larger than those found in contact-resonance atomic force microscopy, so that its geometry is much more controlled. It additionally results in a resonator stiffness which is well suited to materials whose Young's modulus ranges from few MPa to 10 GPa [206].

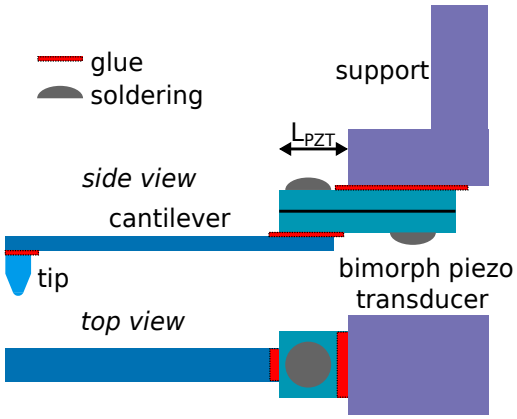

Figure 1.12: Schematic view of the SMM resonator.

3.1.2 Static deflection measurement

The resonator has to be put in contact with the sample under scrutiny in order to probe its mechanical properties. This is achieved in a controlled manner by using a laser diode, whose light is shined on the cantilever apex. The reflected light impinges on a 4 quadrants position-sensitive detector (PSD). The illumination is modulated at 10 kHz and the PSD output is analyzed through a lock-in amplifier. The resulting signals are first used to make sure the cantilever does not experience torsion when the tip is put in contact with the sample. It is also used to precisely detect the contact altitude when the sample is moved toward the resonator.

3.1.3 Vibration measurement

The vibration at the cantilever apex is measured using a heterodyne interferometer [203, 204] whose great stability arises from the use of a beam reflected on the mirror of the laser cavity as a reference beam (see FIG.1.13).

A 3mW He-Ne laser (wavelength λ_L and frequency f_L) is used to produce a linearly, horizontally (in FIG.1.13) polarized beam that goes through a quarter-wave plate whose fast axis is oriented at 0°, so that the polarization is not modified. The beam then goes through a half-wave plate which is oriented with an angle θ_H, so that the polarization is now at an angle $2\theta_H$. The polarizing beam-splitter then divides the incident beam into two orthogonally polarized beams. The transverse magnetic beam (TM) is directed to the photodetector and acts as a reference beam. The transverse electric beam (TE) goes through the Bragg cell and is reflected by the vibrating cantilever surface (frequency: f_a). Denoting $f_B = 81$MHz the Bragg cell frequency, the TE electric field oscillates at $f_L + 2f_B$ after traveling back through the Bragg cell. The TE beam thus goes through the polarizing beam-splitter and the plates. It is reflected back by the cavity mirror and, because of the plates, impinges on the polarizing beam-splitter with a TM polarization. It is thus reflected toward the photodetector, so that this probe beam may interfere with the reference beam (photodetector bandwidth: 350MHz). θ_H is adjusted in order to balance the intensities of

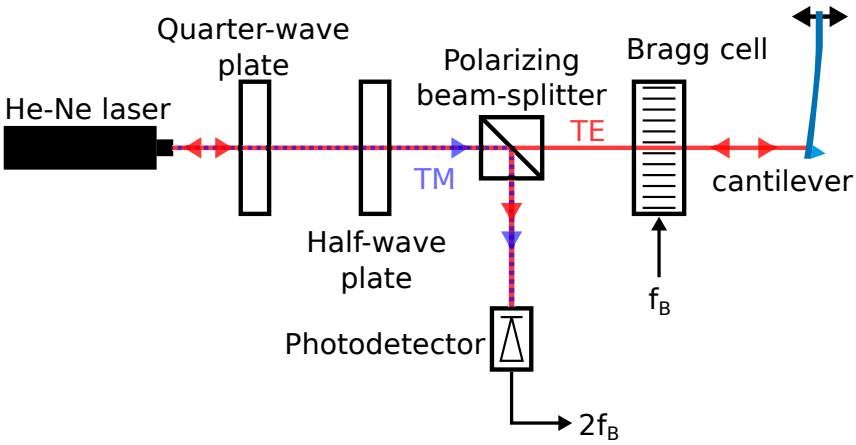

Figure 1.13: Schematic view of the heterodyne interferometer.

the reference and probe beams depending on the cantilever surface reflectivity. Denoting u the cantilever vibration amplitude, a thorough calculation would show that the current i at the photodetector reads

$$i(t) \propto \cos\left[4\pi f_B t + \frac{4\pi}{\lambda_L} u \cos\left(2\pi f_a t + \phi\right) + \phi_S\right] \tag{1.64}$$

where ϕ_S denotes the static phase and ϕ the phase of the cantilever oscillation with respect to the Bragg cell modulation. For a vanishing amplitude u, the current is linearized as

$$\begin{aligned} i(t) \quad \propto \quad & J_0\left(\frac{4\pi}{\lambda_L}u\right)\cos\left[4\pi f_B t + \phi_S\right] \\ & + J_1\left(\frac{4\pi}{\lambda_L}u\right)\cos\left[2\pi(2f_B + f_a)t + \phi_S + \phi\right] \\ & - J_1\left(\frac{4\pi}{\lambda_L}u\right)\cos\left[2\pi(2f_B - f_a)t + \phi_S + \phi\right] \end{aligned} \tag{1.65}$$

where J_0 and J_1 are the first two Bessel functions of the first kind. At the vanishing amplitude limit

$$J_0\left(\frac{4\pi}{\lambda_L}u\right) \simeq 1; J_1\left(\frac{4\pi}{\lambda_L}u\right) \simeq \frac{2\pi}{\lambda_L}u \tag{1.66}$$

so that comparing the current at $2f_B$ with the current at $2f_B \pm f_a$ simultaneously yields the photodetector sensitivity and the vibration amplitude. The interferometer is operated herein at conditions leading to a noise level of about 3.10^{-4} $\mathring{A}.Hz^{-1/2}$.

3.2 Multiple mode SMM (MM-SMM)

Following a preliminary study [199], this section describes a method using the first flexural modes of vibration of the cantilever in scanning microdeformation microscopy. The

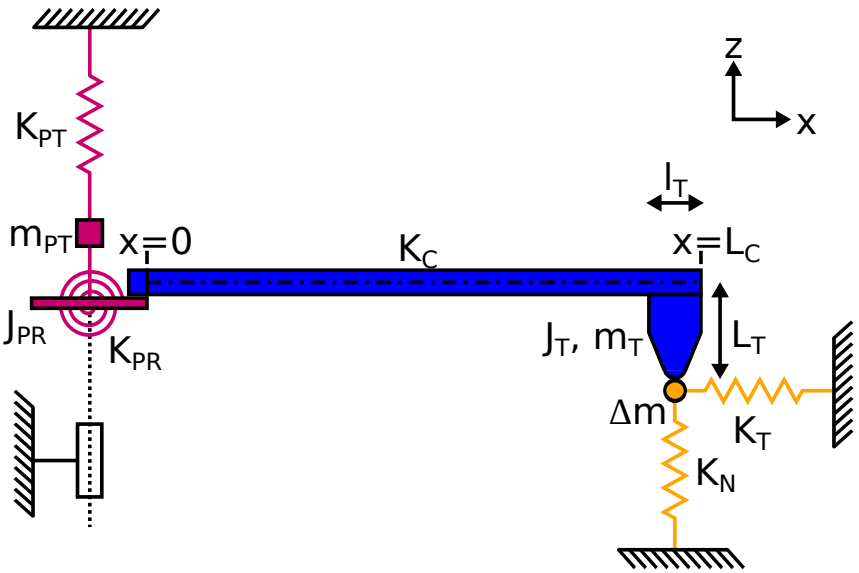

Figure 1.14: Model describing the SMM resonator.

experimental set-up is first presented together with its original mechanical description. The calibration procedure and the identification procedure proposed to achieve robust and quantitative measurements are then introduced. Experimental data have been acquired for an epoxy photoresist (SU-8) thin film to demonstrate the method and the results are compared to data available in the literature and to experimental data obtained on the same sample by nano-indentation.

3.2.1 Mechanical modeling of the resonator

A schematic view of the chosen modeling is displayed in FIG.1.14. The sapphire tip (mass m_T and rotary inertia J_T as calculated at the cantilever neutral fiber) is assumed to be rigid and perfectly glued to the cantilever beam. The dynamic behavior of the piezoelectric actuator is described through linear and rotational springs, whose spring constants are K_{PT} and K_{PR}, respectively. The effect of the actuator moving mass is modeled through the mass m_{PT} and the rotary inertia J_{PR}. When the resonator is brought into contact with a sample to be tested, a (small) mass Δm of tested material moves together with the sapphire tip. The mechanical reaction of the tested sample is described through normal and a tangential springs, whose spring constants are K_N and K_T, respectively.

The cantilever deflection $w(x,t)$ is derived from

$$E_C I_C \frac{\partial^4 w}{\partial x^4} + \rho_C A_C \frac{\partial^2 w}{\partial t^2} = 0 \tag{1.67}$$

where E_C is silicon's "Young's modulus" along the [100] direction, A_C and I_C are the cross-sectional area and the rotary cross-sectional inertia, respectively, ρ_C the silicon mass

density. Denoting L_C the cantilever length and f the frequency, the displacement $w(x,t)$ reads

$$w(x,t) = w_0 \left[C_1 C^+(x) + C_2 C^-(x) + C_3 S^+(x) + C_4 S^-(x) \right] e^{j\omega t} \tag{1.68}$$

with

$$C^+(x) = \cos\left(\frac{\mu}{L_C}x\right) + \cosh\left(\frac{\mu}{L_C}x\right) \quad ; \quad C^-(x) = \cos\left(\frac{\mu}{L_C}x\right) - \cosh\left(\frac{\mu}{L_C}x\right) \tag{1.69}$$

$$S^+(x) = \sin\left(\frac{\mu}{L_C}x\right) + \sinh\left(\frac{\mu}{L_C}x\right) \quad ; \quad S^-(x) = \sin\left(\frac{\mu}{L_C}x\right) - \sinh\left(\frac{\mu}{L_C}x\right) \tag{1.70}$$

and

$$\omega = 2\pi f = \sqrt{\frac{\mu^4 E_C I_C}{\rho_C A_C L_C^4}} \quad ; \quad \mu = \sqrt[4]{\frac{4\pi^2 f^2 \rho_C A_C L_C^4}{E_C I_C}} \tag{1.71}$$

The constants C_1 to C_4 are obtained from the boundary conditions at $x = 0$

$$E_C I_C \left(\frac{\partial^2 w}{\partial x^2}\right)_{x=0} = -K_{PR}\left(\frac{\partial w}{\partial x}\right)_{x=0} - J_{PR}\left(\frac{\partial^3 w}{\partial t^2 \partial x}\right)_{x=0} \tag{1.72}$$

$$E_C I_C \left(\frac{\partial^3 w}{\partial x^3}\right)_{x=0} = K_{PT} w(0,t) + m_{PT}\left(\frac{\partial^2 w}{\partial t^2}\right)_{x=0} \tag{1.73}$$

and at $x = L = L_C - \frac{l_T}{2}$

$$E_C I_C \left(\frac{\partial^2 w}{\partial x^2}\right)_{x=L} = -K_T L_T^2 \left(\frac{\partial w}{\partial x}\right)_{x=L} - \left(J_T + \Delta m L_T^2\right)\left(\frac{\partial^3 w}{\partial t^2 \partial x}\right)_{x=L} \tag{1.74}$$

$$E_C I_C \left(\frac{\partial^3 w}{\partial x^3}\right)_{x=L} = K_N w(L,t) + (m_T + \Delta m)\left(\frac{\partial^2 w}{\partial t^2}\right)_{x=L} \tag{1.75}$$

For the sake of brevity, the following parameters are introduced to describe the resonator

$$p_0 = \frac{\rho_C A_C L_C^4}{E_C I_C}; p_1 = \frac{m_T}{\rho_C A_C L_C} \quad ; \quad p_2 = L_C\sqrt{\frac{m_T}{J_T}}; p_3 = L_T\sqrt{\frac{6m_T}{J_T}}; p_4 = \frac{K_{PT}}{\rho_C A_C L_C}$$
$$p_5 = \frac{m_{PT}}{\rho_C A_C L_C}; p_6 = \frac{J_{PR}}{\rho_C A_C L_C^3} \quad ; \quad p_7 = \frac{K_{PR}}{\rho_C A_C L_C^3}; \quad p_8 = \frac{L}{L_C}; \qquad p_9 = \frac{\Delta m}{m_T} \tag{1.76}$$

and to describe the tested material

$$X = \frac{K_N}{K_C} \quad ; \quad Z = \frac{K_T}{2K_N} \tag{1.77}$$

where K_C refers to the overall cantilever's stiffness. Resonance occurs if the determinant of

$$\begin{bmatrix} 0 & 1 & -\Sigma & 0 \\ \theta & 0 & 0 & 1 \\ [C^-(L) + \beta S^-(L)] & [C^+(L) + \beta S^+(L)] & [S^-(L) - \beta C^+(L)] & [S^+(L) - \beta C^-(L)] \\ [S^+(L) - \alpha C^+(L)] & [S^-(L) - \alpha C^-(L)] & -[C^-(L) + \alpha S^+(L)] & -[C^+(L) + \alpha S^-(L)] \end{bmatrix}$$

vanishes, in which

$$\alpha = \frac{3X - p_1(1-p_9)\mu^4}{\mu^3} \quad ; \quad \beta = \frac{6XZp_3^2 - p_1\mu^4(6+p_9p_3^2)}{6\mu p_2^2} \tag{1.78}$$

$$\theta = \frac{p_0p_4}{\mu^3} - p_5\mu \quad ; \quad \Sigma = \frac{p_0p_7}{\mu} - p_6\mu^3 \tag{1.79}$$

The resonance condition may be written as a rather lengthy closed-form and will be denoted

$$\mathcal{R}(f, p_0, p_1, p_2, p_3, p_4, p_5, p_6, p_7, p_8, p_9, X, Z) = 0 \tag{1.80}$$

in the following. The detailed expression is given in the appendix.

3.2.2 Calibration procedure

As may be inferred from Eq.(1.80), retrieving the material parameters X and Z from resonance frequencies requires the 10 modeling parameters p_i to be accurately known. If some of them may be estimated using accurate geometrical measurements, it is particularly difficult to provide a good estimate for those describing the piezo-actuator. This section therefore proposes a procedure to retrieve the actual values of the modeling parameters, which may be seen as an extension of the one proposed in Ref. [200].

The more straightforward way to include experimental data without introducing uncertainties related to the tested material is to consider the free resonance frequencies, obtained when the resonator is allowed to vibrate without any contact with the sample. The corresponding resonance condition $\mathcal{R}_{free}$ is obtained by setting $X = 0$ and $p_9 = 0$ in the resonance condition (1.80). It can be seen from detailed expression (112), that it only involves the parameters p_0, p_1, p_2, p_4, p_5, p_6, p_7 and p_8. All the parameters except p_3 are thus potentially identifiable using these additional data. Considering a set $\mathbf{f_{free}}$ of n_f free resonance frequencies, one can write a set of n_f non-linear equations

$$\mathbf{R}_{free}(\mathbf{f_{free}}, p_0, p_1, p_2, p_4, p_5, p_6, p_7, p_8) = \mathbf{0} \tag{1.81}$$

the equality being obtained if the modeling is able to describe the actual system and if the measurements are not corrupted. Considering measured resonance frequencies $\tilde{\mathbf{f}}_{\mathbf{free}}$ obtained from a resonator which is inaccurately described by the modeling detailed in Sect. 3.2.1, the right-hand member

$$\mathbf{R}_{free}\left(\tilde{\mathbf{f}}_{\mathbf{free}}, p_0, p_1, p_2, p_4, p_5, p_6, p_7, p_8\right) \neq \mathbf{0} \tag{1.82}$$

is non-zero and one proposes to retrieve the modeling parameters by minimizing the L^2-norm of the left-hand member of Eq. (1.82), which is referred to as the residual in the following. It is then worth noting that Eq.(1.82) is linear with respect to (p_6, p_7) or with respect to (p_4, p_5) provided all the other parameters are fixed (see Eq.(112)). The minimization procedure thus takes advantage of these properties (under the constrain that all the parameters are positive) and is described in FIG.1.15.

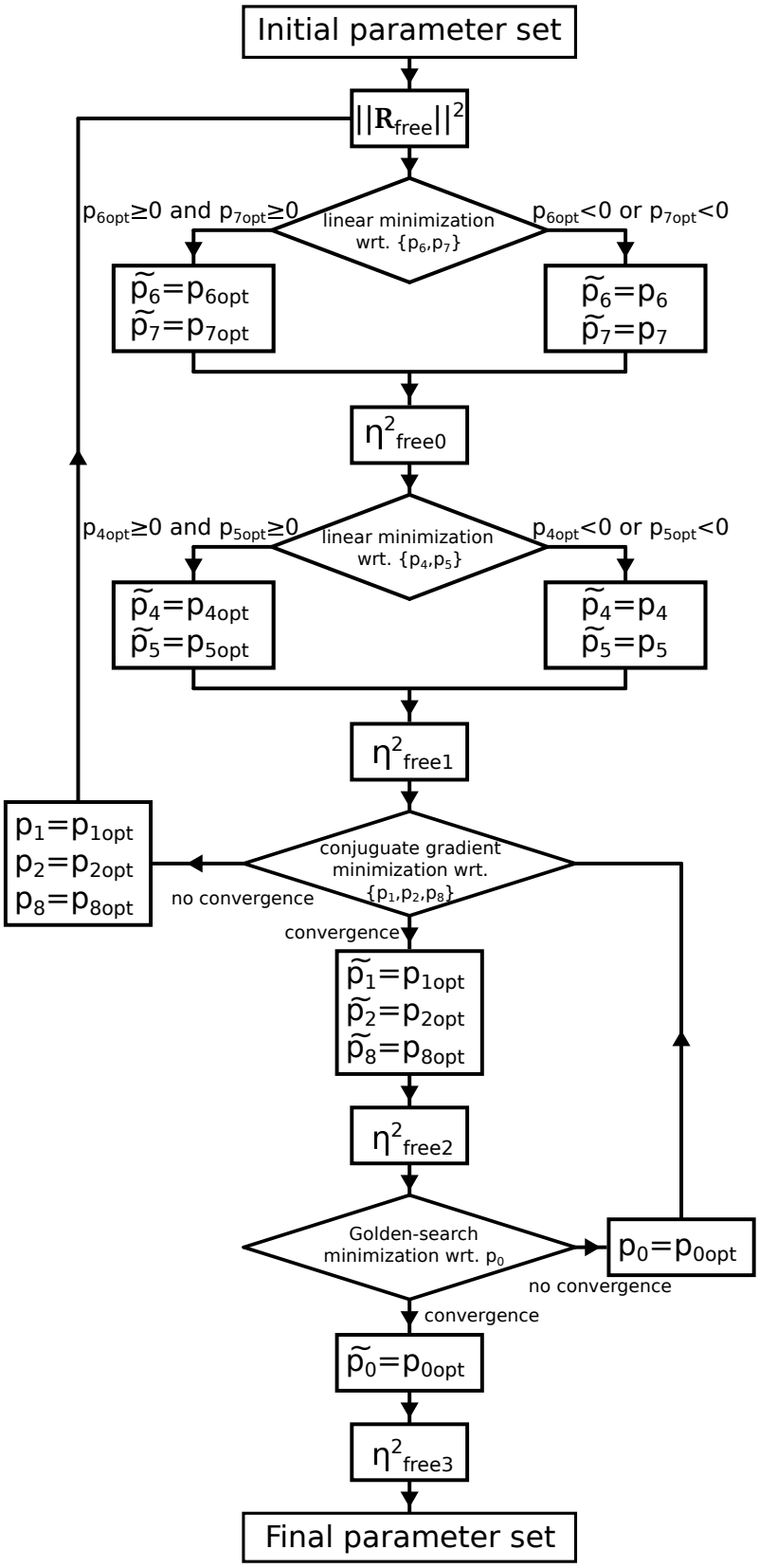

Figure 1.15: Minimization algorithm to retrieve the modeling parameters.

Let us first define $\eta^2_{free_0}$ as the residual norm obtained after the minimization with respect to p_6, p_7.

$$\begin{aligned}\eta^2_{free_0} &= \min_{p_6,p_7} \left\| \mathbf{R}_{free}\left(\tilde{\mathbf{f}}_{\mathbf{free}}, p_0, p_1, p_2, p_4, p_5, p_6, p_7, p_8\right)\right\|^2 \\ &= \left\| \mathbf{R}_{free}\left(\tilde{\mathbf{f}}_{\mathbf{free}}, p_0, p_1, p_2, p_4, p_5, \tilde{p_6}, \tilde{p_7}, p_8\right)\right\|^2 \end{aligned} \tag{1.83}$$

Since $\mathbf{R}_{free}$ is linear with respect to p_6, p_7 and assuming that more than 2 resonance frequencies are available, the optimal values $\tilde{p_6}, \tilde{p_7}$ are obtained as the Moore-Penrose pseudo-inverse, all the other values being fixed. The same procedure is then applied to get the optimal values $\tilde{p_4}, \tilde{p_5}$, thus defining the new residual norm $\eta^2_{free_1}$

$$\begin{aligned}\eta^2_{free_1} &= \min_{p_4,p_5} \left\| \mathbf{R}_{free}\left(\tilde{\mathbf{f}}_{\mathbf{free}}, p_0, p_1, p_2, p_4, p_5, \tilde{p_6}, \tilde{p_7}, p_8\right)\right\|^2 \\ &= \left\| \mathbf{R}_{free}\left(\tilde{\mathbf{f}}_{\mathbf{free}}, p_0, p_1, p_2, \tilde{p_4}, \tilde{p_5}, \tilde{p_6}, \tilde{p_7}, p_8\right)\right\|^2 \end{aligned} \tag{1.84}$$

by exploiting the linearity of $\mathbf{R}_{free}$. If one of these linear minimization steps is unsuccessful (*i.e.,* it yields a negative parameter value), the last available value is kept for the corresponding linear parameter. Such a non-optimal choice has been found to sufficiently penalize the cost function to constrain the linear parameters to be positive. $\eta^2_{free_1}$ is then minimized with respect to p_1, p_2, p_8 to define $\eta^2_{free_2}$.

$$\eta^2_{free_2} = \min_{p_1,p_2,p_8} \eta^2_{free_1}\left(\tilde{\mathbf{f}}_{\mathbf{free}}, p_0, p_1, p_2, \tilde{p_4}, \tilde{p_5}, \tilde{p_6}, \tilde{p_7}, p_8\right) \tag{1.85}$$

$$= \left\| \mathbf{R}_{free}\left(\tilde{\mathbf{f}}_{\mathbf{free}}, p_0, \tilde{p_1}, \tilde{p_2}, \tilde{p_4}, \tilde{p_5}, \tilde{p_6}, \tilde{p_7}, \tilde{p_8}\right)\right\|^2 \tag{1.86}$$

This non-linear minimization step makes use of a slightly modified version of the well-known conjugate-gradient method [207]. The required derivatives are obtained as closed-forms, and the one-dimensional minimization step is performed as a constrained minimization (Golden-search method) in order to always keep the parameters inside the range estimated from the uncertainties on the estimated parameters.In the case a minimizer is obtained, the minimization with respect to p_0 is performed using the Golden-search method to yield $\eta^2_{free_3}$

$$\eta^2_{free_3} = \min_{p_0} \eta^2_{free_2}\left(\tilde{\mathbf{f}}_{\mathbf{free}}, p_0, \tilde{p_1}, \tilde{p_2}, \tilde{p_4}, \tilde{p_5}, \tilde{p_6}, \tilde{p_7}, \tilde{p_8}\right) \tag{1.87}$$

$$= \left\| \mathbf{R}_{free}\left(\tilde{\mathbf{f}}_{\mathbf{free}}, \tilde{p_0}, \tilde{p_1}, \tilde{p_2}, \tilde{p_4}, \tilde{p_5}, \tilde{p_6}, \tilde{p_7}, \tilde{p_8}\right)\right\|^2 \tag{1.88}$$

which is an indicator of the identification quality. $\eta^2_{free_3}$ should be as low as possible, but its value is however difficult to interpret. The final set of parameters correspond to a set of computed frequencies $\bar{\mathbf{f}}_{\mathbf{free}}$ so that we also define

$$q_i = \frac{\left(\bar{f}_{i,free} - \tilde{f}_{i,free}\right)^2}{\tilde{f}^2_{i,free}} \tag{1.89}$$

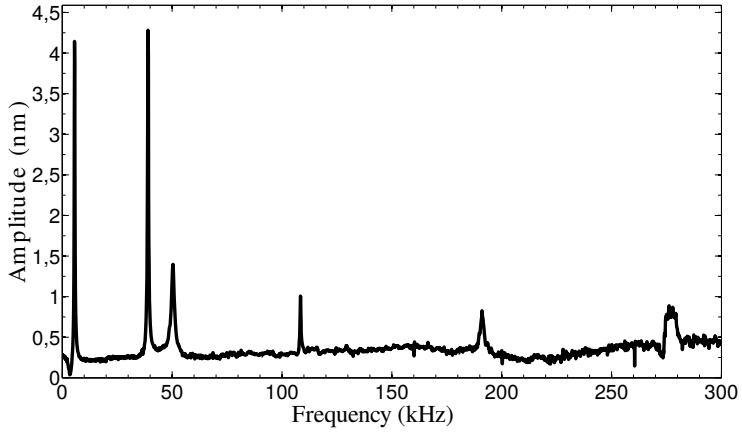

Figure 1.16: Measured amplitude spectrum for the resonator without contact.

Table 1.4: Extracted resonance frequencies without contact.

Modes	1	2	3	4	5	6
Frequencies (kHz)	5.41	38.8	49.6	108	190	274

the frequency error indicator for mode i and

$$Q = \frac{1}{l}\sum_{i=1}^{l} q_i \tag{1.90}$$

the global frequency error indicator.

FIG.1.16 displays the measured amplitude spectrum without contact. Six resonance frequencies are to be seen, and it should be highlighted that the second and the third resonance frequencies are rather close to each other. A fitting procedure in which the peaks are approximated by Gaussian curves is used to extract the resonance frequencies which are displayed in TAB.1.4. It has been found that the sensitivity to the initial parameter values increases with the number of resonance frequencies involved in the identification procedure. The procedure described in FIG.1.15 is thus first applied to the first three resonance frequencies. The set of final values is then used as an initial guess for the minimization using the first four resonance frequencies and so on, until a final set of parameters is obtained when using the 6 resonance frequencies. The resulting parameter values as well as their estimation (used to initiate the procedure) are displayed in TAB.1.5 together with the uncertainties on these estimates, which are used to define the accessible parameter range in the iterative minimization procedure (for the parameters p_0, p_1, p_2, p_8). The two indicators are obtained as $\eta^2_{free_3} = 2.04 \times 10^{15}$ and $Q = 1.04 \times 10^{-3}$, thereby proving the good identification quality, the larger contribution to Q being $q_5 = 6.24 \times 10^{-3}$. The computed resonance frequencies nicely match the experimental ones, so that the identified parameter values in TAB.1.5 are to be used for the measurement of the mechanical

Table 1.5: Estimated (with uncertainties) and identified parameters values.

Parameters	p_0	p_1	p_2	p_8
Estimated	$7.08 \times 10^{-9}\ s^2 \pm 31\%$	$0.336 \pm 24\%$	$15.2 \pm 16\%$	$0.961 \pm 4\%$
Identified	$5.76 \times 10^{-9}\ s^2$	0.275	14.8	0.964
Parameters	p_4	p_5	p_6	p_7
Identified	$1.35 \times 10^{12}\ s^{-2}$	0.607	0.960	$9.55 \times 10^{10}\ s^{-2}$

properties of the tested sample.

3.2.3 Elastic parameters measurement for isotropic materials

Most of the modeling parameters being set by using the above-described calibration procedure, this section is intended to detail the identification of the elastic material parameters of the tested sample from the resonance frequencies measured when the tip is in contact with the sample.

The procedure detailed in Sect. 3.2.2 allows one to identify the values for the parameters $p_0, p_1, p_2, p_4, p_5, p_6, p_7$ and p_8. The identification of the mechanical properties of the specimen thus requires the identification of the parameters p_3 and p_9 together with the material parameters X and Z which are related, using Hertz's relationships in the case of a rigid tip, to the sample's Young's modulus E_S and Poisson ratio ν_S through

$$X = \frac{\sqrt[3]{6(-F_0) r_T \left(\frac{E_S}{1-\nu_S^2}\right)^2}}{K_C} \quad ; \quad Z = \frac{1-\nu_S}{2-\nu_S} \tag{1.91}$$

where r_T is the tip radius and F_0 is the value of the static force applied to the sample [199]. As detailed in Sect. 3.1.2, the contact between the resonator and the sample to be tested is controlled through the static deflection of the cantilever. The contact is first detected, and the sample is then moved of the distance z toward the resonator using a servo-controlled stage. It is therefore possible to get measurements at the same location on the sample for different z values corresponding to different values of the indentation δ_t

$$\delta_t = -\frac{z}{1+\frac{K_N}{K_C}} \tag{1.92}$$

It should also be noted that the parameter p_3 only describes the tip geometry and is thus independent of the tested material. Depending on how much these remarks are considered as *a priori* known information, various identification procedures, corresponding to different sets of assumptions, may be devised. This section is intended to detail the choice leading to the most robust material parameter identification. It is however clear that it is possible to relax the corresponding constrains if necessary. It is thus assumed hereafter that n resonance frequencies have been measured at different locations (for instance A and

B) of the same sample for m different sample displacements ($z_{A_1},\dots,z_{A_m}$ and $z_{B_1},\dots,z_{B_m}$, respectively).

It is first assumed that the mass of the sample moving together with the tip is small compared to the tip mass, so that $p_9 \ll 1$. The resonance condition (87) is thus linearized with respect to p_9. It is also assumed that p_9 linearly depends on the activated volume as estimated by the contact radius a

$$p_9 = p_{9_0} + p_{9_a} a^3 \tag{1.93}$$

the constant term in Eq.(1.93) being added to account for a possible error in the contact detection. The contact radius is obtained

$$a = \sqrt[3]{\frac{3|F_0| r_T (1-\nu_S^2)}{4E_S}} \tag{1.94}$$

On the other hand, for given a resonator and material, the different X values corresponding to different z levels are directly obtained by solving

$$X\sqrt{1+X}K_C = 2\sqrt{\left(\frac{E_S}{1-\nu_S^2}\right)^2 r_T z} \tag{1.95}$$

so that the linearized resonance conditions in contact now read, for any location on the sample

$$\mathbf{R}_{LC}\left(\mathbf{f_{contact}}, \tilde{p_0}, \tilde{p_1}, \tilde{p_2}, p_3, \tilde{p_4}, \tilde{p_5}, \tilde{p_6}, \tilde{p_7}, \tilde{p_8}, \mathbf{p_9}, \mathbf{X}, Z\right) = \mathbf{0} \tag{1.96}$$

$\mathbf{f_{contact}}$ has $n \times m$ components, $\mathbf{p_9}$ and $\mathbf{X}$ have m components whereas p_3 and Z are scalar values, all together yielding $n \times m$ resonance conditions per location on the sample. Using an approach very similar to that introduced in Sect. 3.2.2, considering the measured contact resonance frequencies $\tilde{\mathbf{f}}_{\mathbf{contact}}$ with an estimate of the parameters $p_3, \mathbf{p_9}, \mathbf{X}$ and Z yields

$$\mathbf{R}_{LC}\left(\tilde{\mathbf{f}}_{\mathbf{contact}}, \tilde{p_0}, \tilde{p_1}, \tilde{p_2}, p_3, \tilde{p_4}, \tilde{p_5}, \tilde{p_6}, \tilde{p_7}, \tilde{p_8}, \mathbf{p_9}, \mathbf{X}, Z\right) \neq \mathbf{0} \tag{1.97}$$

so that it is suggested to retrieve p_3, $\mathbf{p_9}$ and the material parameters as the minimizers of $\left\|\mathbf{R}_{LC}\left(\tilde{\mathbf{f}}_{\mathbf{contact}}, \tilde{p_0}, \tilde{p_1}, \tilde{p_2}, p_3, \tilde{p_4}, \tilde{p_5}, \tilde{p_6}, \tilde{p_7}, \tilde{p_8}, \mathbf{p_9}, \mathbf{X}, Z\right)\right\|^2$.

The parameter p_3 is assumed to be identical for all measurements as it describes the tip geometry. The minimization procedure should thus alternate between local minimization steps (for parameters depending on the location) and global steps (for p_3). The proposed minimization algorithm is detailed in FIG.1.17. One first takes advantage of the linearized structure of $\mathbf{R}_{LC}$ with respect to $\mathbf{p_9}$. For each location, an initial set of parameters is used to build the residual norm $\|\mathbf{R}_{LC}\|^2$, which is minimized assuming that $m > 2$ with respect to p_{9_0} and p_{9_a} (see Eq.(1.93)). At location A

$$\begin{aligned}
\eta^2_{LC_0}(A) &= \min_{p_{9_0}, p_{9_a}} \left\|\mathbf{R}_{LC}\left(\tilde{\mathbf{f}}_{\mathbf{contact}}, \tilde{p_0}, \tilde{p_1}, \tilde{p_2}, p_3, \tilde{p_4}, \tilde{p_5}, \tilde{p_6}, \tilde{p_7}, \tilde{p_8}, p_{9_0} + p_{9_a}\mathbf{a}^3, \mathbf{X}, Z\right)\right\|^2 \\
&= \left\|\mathbf{R}_{LC}\left(\tilde{\mathbf{f}}_{\mathbf{contact}}, \tilde{p_0}, \tilde{p_1}, \tilde{p_2}, p_3, \tilde{p_4}, \tilde{p_5}, \tilde{p_6}, \tilde{p_7}, \tilde{p_8}, \tilde{p_{9_0}}(A) + \tilde{p_{9_a}}(A)\mathbf{a}^3, \mathbf{X}, Z\right)\right\|^2
\end{aligned}$$

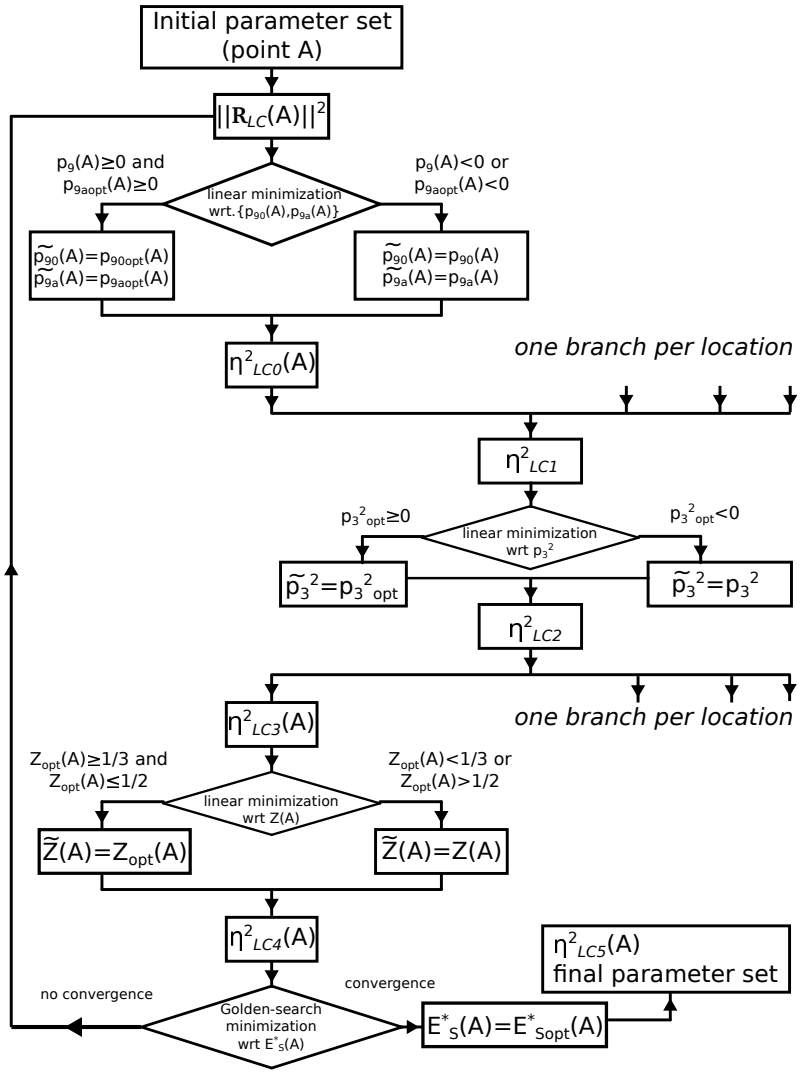

Figure 1.17: Minimization algorithm to retrieve the material parameters.

The optimal values $p\tilde{9}_0(A)$ and $p\tilde{9}_a(A)$ are easily obtained as the Moore-Penrose pseudo-inverse, provided $\tilde{p9}(A)$ and $p\tilde{9}_a(A)$ are positive. After these parameters have been retrieved at any considered location, the global indicator $\eta^2_{LC_1}$ is defined as the sum of the indicators $\eta^2_{LC_0}(P)$ over all the considered locations $\{P\}$

$$\eta^2_{LC_2} = \min_{p_3} \eta^2_{LC_1} = \min_{p_3} \sum_P \eta^2_{LC_0}(P) \tag{1.98}$$

$\mathbf{R}_{LC}$ is linear with respect to p_3^2 so that the optimal value $\tilde{p_3}^2$ is obtained as the minimizer of $\eta^2_{LC_1}$. Again, its value is obtained as a Moore-Penrose pseudo-inverse, owing to the linear structure of $\mathbf{R}_{LC}$, and is kept only if $\tilde{p_3}^2 > 0$. The algorithm then goes local again in order to retrieve the material parameters. The contribution $\eta^2_{LC_3}(P)$ of each location P to the indicator $\eta^2_{LC_2}$ is then minimized with respect to the material parameter Z

$$\begin{aligned}
\eta^2_{LC_4}(P) &= \min_Z \eta^2_{LC_3}(P) \\
&= \min_Z \left\| \mathbf{R}_{LC}\left(\tilde{\mathbf{f}}_{\mathbf{contact}}, \tilde{p_0}, \tilde{p_1}, \tilde{p_2}, \tilde{p_3}, \tilde{p_4}, \tilde{p_5}, \tilde{p_6}, \tilde{p_7}, \tilde{p_8}, p\tilde{9}_0(A) + p\tilde{9}_a(A)\mathbf{a}^3, \mathbf{X}, Z\right)\right\|^2 \\
&= \left\| \mathbf{R}_{LC}\left(\tilde{\mathbf{f}}_{\mathbf{contact}}, \tilde{p_0}, \tilde{p_1}, \tilde{p_2}, \tilde{p_3}, \tilde{p_4}, \tilde{p_5}, \tilde{p_6}, \tilde{p_7}, \tilde{p_8}, p\tilde{9}_0(A) + p\tilde{9}_a(A)\mathbf{a}^3, \mathbf{X}, \tilde{Z}(P)\right)\right\|^2
\end{aligned}$$

Again, $\mathbf{R}_{LC}$ is linear with respect to Z so that the optimal value $\tilde{Z}(P)$ is easily obtained. This optimal value is kept if it satisfies $1/3 \leq \tilde{Z}(P) \leq 1/2$ (corresponding to $0 \leq \nu_S \leq 1/2$). For a given location and provided the sample displacements $\mathbf{z}$ are known, it can be seen from Eq.(1.95) that $\mathbf{X}$ only depends on the indentation modulus E^*_S. Its value is thus retrieved as the minimizer of $\eta^2_{LC_4}(P)$

$$\begin{aligned}
&\eta^2_{LC_5}(P) \\
&= \min_{E^*_S} \left\| \mathbf{R}_{LC}\left(\tilde{\mathbf{f}}_{\mathbf{contact}}, \tilde{p_0}, \tilde{p_1}, \tilde{p_2}, \tilde{p_3}, \tilde{p_4}, \tilde{p_5}, \tilde{p_6}, \tilde{p_7}, \tilde{p_8}, p\tilde{9}_0(A) + p\tilde{9}_a(A)\mathbf{a}^3, \mathbf{X}(E^*_S, \mathbf{z}), \tilde{Z}(P)\right)\right\|^2 \\
&= \left\| \mathbf{R}_{LC}\left(\tilde{\mathbf{f}}_{\mathbf{contact}}, \tilde{p_0}, \tilde{p_1}, \tilde{p_2}, \tilde{p_3}, \tilde{p_4}, \tilde{p_5}, \tilde{p_6}, \tilde{p_7}, \tilde{p_8}, p\tilde{9}_0(A) + p\tilde{9}_a(A)\mathbf{a}^3, \mathbf{X}(\tilde{E^*_S}(P), \mathbf{z}), \tilde{Z}(P)\right)\right\|^2
\end{aligned}$$

The above-described procedure thus yields the modeling parameter p_3, and for all considered locations. The sample mass moving together with the tip as a function of the contact force (through p_{9_0} and p_{9_a}), the Poisson's ratio ν_S deduced from $\tilde{Z}$ and the indentation modulus $\tilde{E^*_S}$. It should be highlighted that it has been assumed that the material properties are identical throughout the probed frequency range.

The tested sample is a 20μm thick film of SU-8 (an epoxy-based photoresist) spin-coated on a silicon substrate and covered with 7nm of gold. Its behavior is expected to be isotropic linear elastic without any time-dependence, so that the constitutive description used in Sect. 3.2.3 is well suited. Two distinct data sets are to be used:

- $n = 4$ resonance frequencies have been measured for $m = 2$ sample displacements at two different locations (A and B);

Table 1.6: Measured resonance frequencies (resonator contacting the SU-8 sample).

Point	*A*	*A*	*B*	*B*	*C*	*C*	*C*	*C*
z, μm	0.5	0.75	0.5	0.75	0.1	0.189	0.307	0.42
mode 1, kHz	25.8	26.6	24.6	25.2	19.6	21.3	22.6	23.5
mode 2, kHz	45.0	45.7	43.5	44.1	42.8	43.7	44.4	44.8
mode 3, kHz	50.8	50.9	50.0	50.0	49.7	49.7	49.7	49.6
mode 4, kHz	113	114	113	113	110	110	109	109

Table 1.7: Identified parameters for the SU-8 sample.

	Point *A*	Point *B*	Point *C*
p_{9_0}	-3.21×10^{-3}	-2.33×10^{-2}	-2.0×10^{-3}
p_{9_a}	$3.76 \times 10^{17}\ m^{-3}$	$4.40 \times 10^{17}\ m^{-3}$	$4 \times 0.10^{17}\ m^{-3}$
E_S^*	7.04 *GPa*	6.65 *GPa*	6.36 *GPa*
Z	0.381	0.369	0.370
E_S	6.00 *GPa*	5.50 *GPa*	5.28 *GPa*
ν_S	0.384	0.416	0.413

- $n = 4$ resonance frequencies have been measured for $m = 4$ sample displacements at a single location (C)

, and they are reported in TAB.1.6.

The procedure described in Sect. 3.2.3 is then independently applied to the two data sets, using initial material parameter values obtained by few direct calculations. Again, the identification quality is assessed by the value of the indicators defined by Eqs.(1.89) and (1.90). For the first data set, the global values $Q = 1.64^{-3}$ (for point A) and $Q = 1.34 \times 10^{-3}$ (for point B) prove the good identification quality. p_3 identified value ($\tilde{p_3} = 5.40$) is very close to the estimated $p_3 = 5.41$. Similar comments hold for the second data set, for which the same p_3 value is retrieved and $Q = 1.29 \times 10^{-3}$. The corresponding identified parameters values are reported in TAB.1.7, and the identified elastic parameters are in good agreement with those obtained using different methods and reported in the literature [208, 209, 210, 211]. It is also worth noting that the identified p_{9_a} values are all similar. TAB.1.8 displays the identified geometrical parameters. It can be seen that the contact radius is small compared to the film thickness, thereby suggesting that the SU-8 properties are actually probed without any perturbation from the silicon substrate. It should be stressed that good practices require a trade-off regarding δ_t. On the one hand, probing small volumes calls for small δ_t values, whereas it should be large compared to the sample roughness in order to provide reliable values for the material parameters. The probed volume is driven by the contact radius a, which is a few hundreds of nanometers, thereby demonstrating the very local nature of the reported measurements. The identified p_9 values are also found to be small compared to 1, thus supporting the linearization

Table 1.8: Identified contact parameters for the SU-8 sample.

Point	A	A	B	B	C	C	C	C
z, μm	0.5	0.75	0.5	0.75	0.1	0.189	0.307	0.42
a, nm	514	589	524	600	305	379	447	498
p_9, 10^{-2}	4.78	7.37	3.98	7.18	0.966	2.03	3.45	4.83
δ_t, nm	-17.6	-23.1	-18.3	-24.0	-6.19	-9.57	-13.3	-16.5

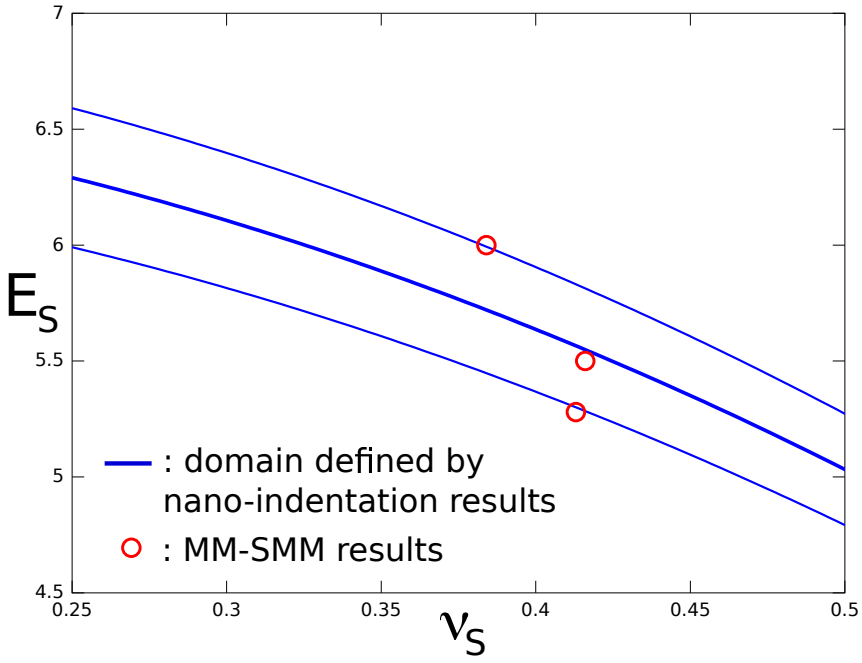

Figure 1.18: Comparison of the MM-SMM and nano-indentation results.

which has been assumed in Sect. 3.2.3.

The identified material parameters are compared to nano-indentation results obtained on the same sample (ultra-nanoindentation probe from CSM instruments) with comparable mean contact pressure and displayed in FIG.1.18. Averaging 28 nano-indentation tests performed on the same sample yields $E_S^* = 6.71 \pm 0.32$ GPa. This range thus defines an elastic parameter domain in between the lower and upper lines displayed in FIG.1.18. The elastic parameters obtained using the above-described procedure have also been reported and fit into the domain defined by the nano-indentation results, thus illustrating the good agreement between results and validating the proposed method.

The identification results may be furthermore post-processed to provide the contact force values. Combining Eq.(1.92) with the $F_0(\delta_t)$ relationship given by Hertz's theory

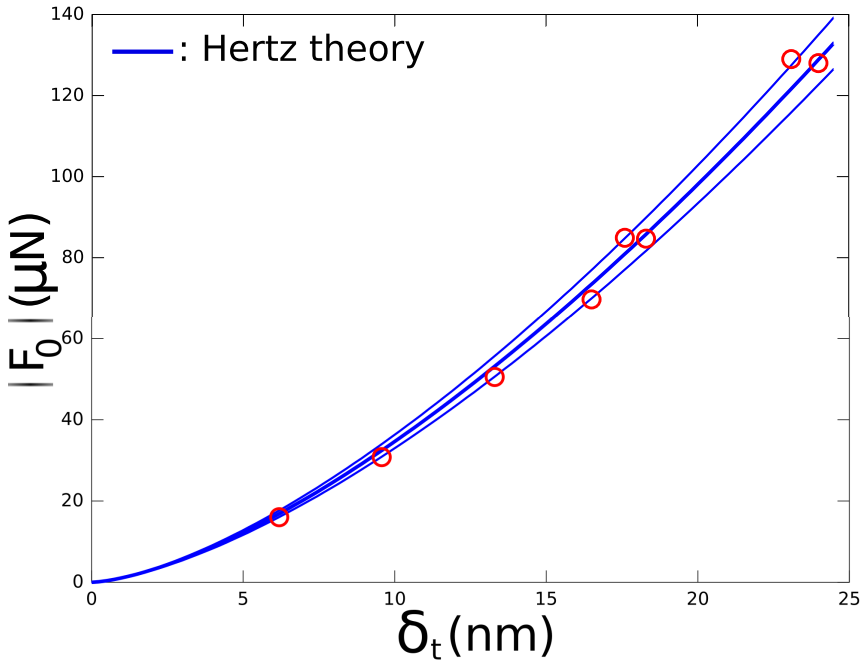

Figure 1.19: Identified F_0 (for all locations) and z values as a function of δ_t (points).

yields

$$\sqrt[3]{\frac{9F_0^2}{16r_T\left(\frac{E_S}{1-\nu_S^2}\right)^2}} = \frac{z}{1+\frac{\sqrt[3]{6(-F_0)r_T\left(\frac{E_S}{1-\nu_S^2}\right)^2}}{K_C}} \tag{1.99}$$

which is numerically solved for F_0. F_0 is thus retrieved for all locations and z values, and the results are reported in FIG.1.19. The retrieved contact force values match those predicted using Hertz's theory and the indentation modulus obtained by ultra-nanoindentation, thus supporting the assumption of a Hertzian contact. FIG.1.19 also illustrates the complementarity of the two data sets, with measurements at point C yielding data for a very low penetration. It should be outlined that including data over a large penetration range allows one to probe the force-penetration law, and that the proposed method may be easily adapted to any other force-penetration law resulting from a more complex material behavior (*e.g.,* plasticity, viscosity) or more complex interactions (*e.g.,* adhesion).

3.3 Towards a full-field SMM (FF-SMM)

The developments described in Sect. 2.1 and 3.2 allow one to imagine the combination of these devices so as to provide additional redundant data to be used in order to extend the range of behaviors that can be probed. Focusing on elasticity, it is believed that measuring the surface rotation field in the vicinity of the SMM tip (see FIG.1.7) will be useful to characterize isotropic or anisotropic materials.

3.3.1 Isotropic materials

It should be noted that the closed-form expression for the rotation field in Boussinesq theory scales as $\frac{P}{E_S^*}$, so that this ratio is likely to be identifiable from the sole full-field measurements. This quantity also appears in Eq.(1.99), so that the static component of the rotation field may allow to make sure the modeling is accurate and to identify the tip radius r_T (see Eq. (1.99)).

3.3.2 Anisotropic materials

The above-mentioned perspective particularly holds for transversely isotropic materials (*i.e.,* vanishingly small-grained materials with a fiber texture) with the isotropy plane parallel to the sample surface. A mismatch in $\frac{P}{E_S^*}$ in Eq. (1.99) and in the rotation field interpreted through Boussinesq's solution should probably be the primary indicator of a discrepancy in the used set of assumptions.

For less "symmetrical" elasticity tensors, it is clear that the measured kinematic field should at least provide an indication of the in-plane orientation of the elastic tensor, so that the perspective is to be able to develop a "mechanical EBSD" apparatus, providing maps of crystal orientations and elastic parameters.

Chapter 2

Surface effects

It has already been mentioned in the first chapter that micrometer-sized objects require a specific modeling effort since their ability to interact with their environment increases with their surface/volume ratio. The latter is much higher than for usual objects, and it has been shown to induce new drawbacks for engineers (fatigue of silicon for instance). This second chapter is devoted to the new capabilities that can be drawn from these chemo-mechanical surface couplings. The context of the development of micromechanical sensors based on these surface couplings is recalled and an overview of the possible ways to model such surface effects is presented together with the corresponding (experimental and/or theoretical) challenges. Several experimental developments addressing these challenges are described and two particularly promising description frameworks are detailed, together with approaches making use of multi-physical full-field measurements to identify the involved parameters.

Contents

1 Surface couplings: from the application back to the theory

Since the emergence of integrated circuits at the end of the 1950s as a response to the "tyranny of numbers", miniaturization has been a concern for the electrical engineering community, namely, being able to produce solid-state transistors was useless without the possibility to connect them efficiently and reliably. The wires between transistors were all soldered by hand, thus limiting both the increase in complexity and the reliability of the final device. The groundbreaking idea was to integrate the circuitry to the semi-conductor piece holding the transistors. It allowed the mass-production of reliable devices, and has been the starting point for successive technologies, all described by the "integration-level", measured as the number of transistors per chip, they allow: small-scale integration (early 60s), medium-scale integration (late 60s), large-scale integration (70s) and very-large-scale integration (80s). The technology was at that time mature enough to allow for other communities to benefit from the miniaturization possibilities. Non-electronic functions thus started to be integrated to the chips, and restricting to mechanical applications, this yielded devices such as pressure sensors, accelerometers, gyroscopes, microphones or ink-jet printer cartridges that are now on the market. The motivation was then mainly the same as for electronic devices, namely, integration (all the above-mentioned mechanical devices are electrically read or driven), reliability and mass production.

It should thus be outlined that none of these products exploit any scaling effect on the mechanical behavior of the used structures, and that issues related to the miniaturization of the mechanical structures mostly arise with the (unexpectedly crucial) role of the environment on the product reliability (see [33] for instance). It is however well established that downsizing structures make their surface-over-volume ratio much larger than for usual objects, so that their ability to interact with their environment is significantly augmented. This chapter is thus devoted to mechanical devices that readily exploit this scaling effect. This section thus focuses on micromechanical sensors that have been devised in the last decades and on the way the observed effects challenge the available modeling frameworks.

1.1 Micromechanical sensors

The early 80s have actually seen the emergence of an increasing interest in micromechanical techniques for sensor technologies [212], the iconic device being a cantilever structure whose deformation is measured using the optical lever technique as for atomic force microscopy (AFM) [213] (see Fig. 2.1). The rapid development of the latter provided a sensing platform to be tailored in order to make the cantilever bend when the phenomenon under scrutiny occurs. As AFM cantilevers are usually made of a silicon(-based) material and are usually coated with a metallic layer in order to increase their reflectivity, they are naturally subjected to the bimetallic effect. This property has thus been exploited to turn an AFM set-up into a micro-calorimeter [214], a photothermal spectrometer [215] or a

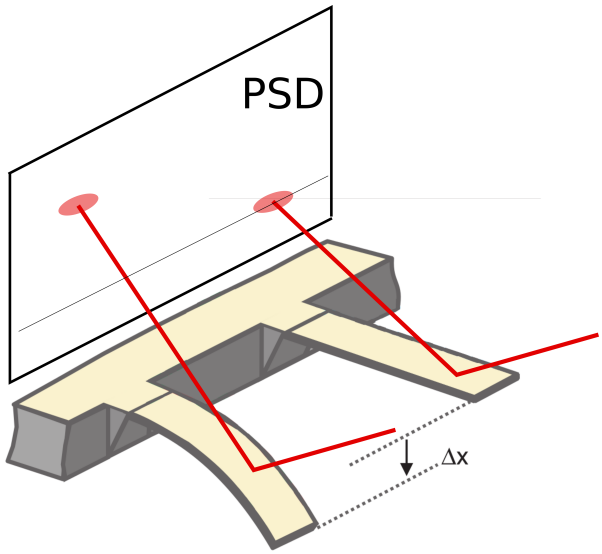

Figure 2.1: Schematic view of the iconic read-out principle.

radiation dosimeter [216]. A significant effort has then been put on the development of infrared optical sensors much more efficient and cost-effective than the available bolometers at that time [217, 218, 219]. Simultaneously, the versatility of the cantilever-sensor platform was exploited to analyze minute amounts of materials locally deposited onto the cantilever. The mass of the added material could be measured by monitoring the cantilever resonance frequency change, and as the surrounding temperature was swept, both the heat flux on the cantilever and the volume change of the added material could be monitored [220]. This pioneering work was somehow emblematic of both the promises and the difficulties of the chemical analysis based on cantilever sensors:

- Monitoring both the dynamic and the static response of the cantilever yields complementary data on the actual modification of the probed structure. Even though many of the groups that will jump into the field afterward will focus on either the dynamic or the static detection mode, this is the measurement of **both** static and dynamic responses that makes the cantilever sensor quantitative.

- The difficulty is that phase transitions, absorption or adsorption are rather complex phenomena. In the above-mentioned example, the triggered phase transition simultaneously generates a heat flux and a volume change, resulting in opposite contributions to the cantilever bending. Monitoring the sole apex displacement would have lead to a cruel misinterpretation (nicely circumvented by the authors), which highlights the fact the cantilever static bending may originate from different and convolved sources.

It is also worth mentioning that the resonance frequency change may also result from both stiffness and mass changes, so that these contributions have in general to be clearly identified and distinguished [221].

It is therefore clear that a robust interpretation of the monitored (static and/or dynamic) response requires a clear understanding of the activated phenomena. Contrary to the above-mentioned studies relying on well identified chemically or thermally induced volume changes, Berger *et al.* [222, 223] had to attribute the effects they observed using alkanethiols on gold to the "surface stress" generated by assembling a monolayer at the gold surface. The quotes result here from the different definitions in use in the concerned communities and from the controversy attached to this definition in some of these communities. Even though this point is to be more specifically addressed in Sect.1.2, it should already be made clear that this is the prototype of surface effects which do not reduce to any volume change of a material layer and which therefore are under the scope of this chapter.

These findings however demonstrated that micromechanical structures could be used to detect another chemical signature, independent of the above-mentioned thermal effects and volume changes. Measuring and decoupling these different contributions would allow the identification of chemical species, and the integration of a large number of micromechanical structures on a single chip would then make an "artificial nose" possible [224, 225, 226]. The development of measurement systems able to address cantilever arrays [227] actually allowed the use of multiple chemical sensors in parallel [228].

From that point, most of the efforts have been put on the extension of the applicability range of the iconic cantilever sensor (one of its surfaces is chemically modified by the reaction under scrutiny and its mean curvature is read-out using the optical lever technique) [229]. This required to move from gas to liquid phase. The need for DNA sequencing tools without PCR amplification [230, 231, 232, 233] and the need for biochemical tests requiring minute amounts of material [234] or minimal molecule labeling [235] have been driving some of these efforts [236]. It is worth noting that for DNA hybridization as for alkanethiols, it has been proven that the observed deformations arise neither from bimetallic effect nor a cantilever volume change, so that it has been ascribed to a "surface stress" whose origin has been some source of debate [237, 238] since DNA may be seen as a highly charged polymer thus contributing to both the electrostatic and entropic parts of the monolayer free energy. The counterpart is that DNA-modified surfaces make cantilever sensors sensitive to a wide range of parameters, which in turn allows one to monitor a wide range of effects [239, 240, 241, 242, 243, 244].

Homeland security [245, 246, 247] and biological applications also motivated the development of dynamic sensors [248] with an improved mass sensitivity [249, 250] allowing for the detection of mass changes corresponding to a single virus [251] and less [252]. Most of the biological applications however require liquid samples, which usually drastically damp these resonators and degrade their mass sensitivity [253]. An alternative is to make the liquid flow inside the cantilever, which however makes the fabrication process rather challenging [254, 255].

Pushing toward new applications for cantilever sensors requires to integrate the full set-up, including the measurement device to read-out the cantilever curvature. Integrated

alternatives to the optical lever technique include embedded piezoelectric transducers [256] or piezoresistors [257, 258, 259, 260, 261] or waveguides [262]. Whatever the read-out principle, considering static and/or dynamic modes allowed for the development of devices able to monitor various pathogenic agents [263, 264, 265, 266, 267, 268]. Detecting the human immunodeficiency virus has also been challenged [269, 270] and some efforts have been made to monitor some key human bodies functions using cantilever sensors [271, 272, 273]. In the meantime, pharmaceutical research has been facing the need for high-throughput affinity testing, and cantilever sensors take advantage of possibly high integration levels to offer cost-effective perspectives [274, 275]. Recent results have also shown the possibility to detect RNA mutations [276], and there is no doubt that functionalizing cantilevers using aptamers [277, 278] may significantly enlarge the applications spectrum.

1.2 Modeling surface effects

It may however be surprising to see how few of these potentialities have turned into products or devices usable outside of research labs. The first reason may be that even operated under well controlled conditions, the above-described iconic set-up yields somehow controversial results for key systems such as those intended to monitor DNA hybridization [279]. Good practices required to avoid artifacts resulting from thermal drifts and refractive index changes near the chemically modified surface of the cantilever did spread rather lately [280, 281], so that it may be for now very difficult to draw conclusions of the published controversial experimental material.

Another major difficulty arises from the fact that real-life measurements often requires to probe trace amounts of a target chemical in a complex mixture which may contain interfering species at much higher concentrations [282]. Even if the difference in affinity of the modified cantilever surface is good for proof-of-concept experiments with limited interfering species, relying on the sole surface modification do not seem sufficient to make the sensor specific enough for a use without any pre-concentration or purification step.

In addition, the mechanical deflections to be measured are usually very low and establish very slowly (typically tens of nanometers in tens of minutes), so that enhancing the mechanical deformation to be measured for a given target concentration has been stimulating some developments. The first path is purely chemical and aims at optimizing the probe density at the cantilever surface [283, 284, 285, 286, 287]. The second one evidenced that modifying the surface topography significantly affects the measured deflection, thus suggesting that there is room on the mechanical side for optimization [288, 289, 290].

This puts the focus on the need for a robust mechanical framework to describe the chemo-mechanical coupling that should take into account the surface and some of its geometrical details. If this surely challenges solid mechanics (whose initial statement is usually to consider an elementary **volume**), electrochemistry studies have early on been

facing the need to describe electrocapillarity, understood as the dependence of the surface quantity of a metallic domain to the surface electrical potential. It is worth noting that even though the pioneers focused on mercury (which is liquid at room temperature) [291, 292], similar effects have been observed for solids with an experimental arrangement strikingly resembling the above-described iconic set-up [293, 294]. It is thus not surprising that cantilever-based set-ups have quickly been used to investigate electrochemically-induced mechanical effects [295]. The electrochemistry community then rapidly made metal-coated cantilevers the platform to translate the early studies on mercury to solid electrodes [296, 297, 298, 299]. The thermodynamic framework developed for liquid electrodes however proved to yield some controversy, mainly as a result of the different deformation mechanisms [300, 301, 302, 303, 304]. Similar systems allowed to envision sensors whose affinity toward a user-defined ion is driven by the surface electrical potential of the microcantilever [305, 306, 307]. Electrochemistry clearly yields additional information that is very useful for the identification of species, and this has been used for rather different targets [308, 309, 310, 311], including molecules involved in biochemical processes [312, 313, 314]. Besides sensor applications, the electro-elastic coupling may be exploited for actuation purposes with dedicated functionalization [315]. Varying the potential in the double-layer regime allows to reversibly move anions or cations close by the surface, and the measured charge density and mechanical deflection have been shown to indicate the surface accessibility to these ions, thus allowing to probe the structure of the electrode surface [316, 317].

The electrochemical control of the active cantilever's surface is thus extremely interesting since it may benefit:

- from the previous discussions on the thermodynamic framework to describe the electro-chemically induced mechanical effects;

- from the well established know-how relying on extensive and detailed studies of the interphase structure for a wide range of systems. The implementation of these surface functionnalizations is now well documented and a rather vast amount of experimental data is available in the literature.

Cantilever devices featuring a metallic surface whose electric potential is user-controlled are therefore good model systems for the study of chemo-mechanical couplings. They are thus good candidates to study the transduction mechanisms, and a representative example is provided by redox-terminated self-assembled monolayers. The oxidation/reduction of the redox end-group is exploited to generate the microcantilever deformation, and it has been shown with ferrocenylundecanethiolate monolayers that the measured deformations seem to be driven by the correlation of the positions of the grafted molecules instead of the sole mean grafting density [318, 319]. This stresses the need for detailed field descriptions of the chemical species at the electrode surface under scrutiny. Again, the electro-chemistry community developed early on such set-ups [320, 321], especially when investigating microelectrodes [322]. It is worth noting that these set-ups make use

of interferometric imaging techniques, the measured phase changes resulting from the refractive index profiles and thus from the concentration profiles at the surface. Very similar interferometric imaging techniques have interestingly been exploited to access the full surface displacement field of microcantilevers, thus yielding much richer mechanical data compared to the iconic, optical lever-based, set-up [323, 324, 325, 326, 327, 328]. Spatially resolved mechanical data may also be retrieved by including scanning stages in the iconic set-up [329, 330], and it should be noted that considering point-wise measurements, the optical lever arrangement allows for the combination with an ellipsometer to simultaneously provide the deformation and the chemical state of the active cantilever surface [331]. The twofold nature of the phase measured with the interferometric imaging set-ups suggests that these chemical and mechanical contributions to the optical phase have to be decoupled to yield unbiased fields [332]. These interferometric imaging techniques thus potentially provide a huge amount of data, but the decoupling procedure relies on several assumptions that are difficult to assess [332]. If there is clearly room for some improvements here, it should be highlighted that these redundant kinematic measurements may be expected to provide key information to those interested in building a robust mechanical framework suited to these surface effects. It is clear that Stoney's equation (relating the cantilever bending to the tension in a deposited layer) [333] is well suited to single-point measurements, since it relates a scalar tension to a scalar (measured) curvature under few assumptions:

- shear stresses are not taken into account;
- the deposited layer is thin compared to the cantilever thickness;
- the layer material stiffness is similar to those of the cantilever.

This really simple relation approximates the cantilever deformation and may be enriched when the considered system departs from the above assumptions [334, 335]. It should however be noted that it is assumed that the curvature is measured far from the cantilever ends (St-Venant's principle) and that the layer undergoes a volume change. Dealing with such transformations, shear-stresses may be taken into account and the stress and strain fields may be computed [336, 337, 338, 339, 340, 341].

The proper description of **surface** effects is however much more challenging to continuum mechanics, and the barrier to overcome is twofold:

- Surface and volume local quantities (such as kinematic or associated variables) are to be established in a way that allows the derivation of field equations;
- As several forms of energy are concerned in the coupled phenomena under scrutiny, a suited framework must allow for a clear thermodynamic definition of the involved mechanical parameters.

The surface science community as well as the electrochemistry community (following the pioneering work by Grahame on liquid electrodes [291, 292]) have for instance been

hosting debates on the proper thermodynamic definition of a "surface stress" [342, 343, 344, 345, 346, 347, 348, 302, 349, 350] but none of these works have established a clear connection between the "surface stress" and the stress tensor in the underlying solid so that no field equation on the "surface stress" could be derived. Moving in an opposite direction (*i.e.* regardless to any thermodynamic consideration) consists for instance of considering stresses in a cantilever as distributions with the "surface stress" being described as a Dirac centered on the cantilever surface. The resulting kinematic fields are then derived with a kinematic enrichment (compared to usual beam theories) to properly account for boundary conditions [351].

In addition to this difficulty to describe surface (chemical) loadings in a solid mechanics framework, one has to account for the reported increasing role of surfaces in elasticity as the object size decreases [352, 353, 354]. Conversely, the frameworks developed to account for size-dependent elastic behaviors are sound starting points for the description of surface effects. Gurtin and Murdoch proposed a general framework [355, 356] to account for surface effects (including non-linearity), featuring a membrane with surface elasticity parameters (*i.e.* Lamé parameters for surfaces, which are different from those describing the bulk material) and a surface stress tensor. The latter has to satisfy an equilibrium condition which results in field equations for the surface variables. This theory was initially developed for industrial products with modified surfaces (such as those resulting from a shot-peening process for instance), and received a renewed interest with the availability of vanishingly small objects [357]. This framework however suffers from several drawbacks:

- The surface elastic parameters may be negative, which makes their thermodynamic definition questionable;

- It has been demonstrated by Steigmann and Ogden [358, 359] that the response of a solid experiencing compressive surface stresses cannot be correctly obtained from Gurtin-Murdoch theory, which does not account for the membrane flexural stiffness.

An alternative route to describe size-dependent elasticity is to use higher-order elasticity theories, that is to assume the local free energy density depends on the local strain as well as on the local strain gradient [360, 361, 362]. As most of the experimental results exhibiting size-dependent elasticity have been obtained with cantilever beams [363], beam theories have been developed under both the Euler-Bernoulli [364, 365, 366, 367] and Timoshenko [368, 369, 370] kinematic assumptions.

Several frameworks are thus available to describe surface effects and their increasing role with the decreasing size of the objects under scrutiny. The goal is to be able to describe surface, chemically-induced, mechanical **loadings**, that is a strong chemo-mechanical coupling (a chemically-driven source term in the mechanical equilibrium equations). Two classes of approaches may then be envisioned:

- One may wish to separate the task of modeling the detail of the chemical (or electrostatic, entropic, steric) interactions involved in the chemically-modified layer (see [371, 372, 373, 374] for this particular point) from that of calculating the response of a micro-fabricated structure to such a surface loading. Begley *et al.* [375] proposed such a framework which resembles the one proposed by Gurtin and Murdoch. The surface elastic parameters (which mimic an effective film stiffness) and the initial surface stress are deduced from thermodynamic arguments and these mechanical variables are used to describe the mechanical consequences of the chemical surface modification. Such approach allows to compute the deformation of the micro-fabricated structure under a chemical loading with a clear thermodynamic definition of the involved parameters and taking the boundary conditions into account [376]. Such framework thus tackles the above-mentioned weaknesses of the Gurtin-Murdoch theory, except the one evidenced by Steigmann and Ogden [358, 359].

- A family of alternative approaches consists of simultaneously simulating the details of the surface modification (at the molecular level) and the deformation of the underlying material. In order to limit the computation costs, such approaches typically mix a continuum description of the structure with an atomistic description of the surface layers undergoing a chemical transformation. The computation cost usually restricts the simulation to a small portion of the structure under scrutiny so that the boundary conditions are not taken into account. The spatial distribution of the chemical modifications is also often assumed to be homogeneous (see [238, 377] for instance). The different mechanical descriptions one may use for the structure material then differentiates one framework from another:

  - Most of these frameworks use standard elasticity, and it has been shown that the use of such a simple description yields two scaling regimes when the structure thickness is reduced [378];
  - The Gurtin-Murdoch theory may be used for the structure itself, thus rendering the thickness-dependent elasticity when simulating physisorption [379] or chemisorption [380, 381] phenomena.

  The main difficulty with this set of approaches arises from their multiscale nature. These approaches make use of the so-called Cauchy-Born localization rule [382, 383] to translate at the atomistic scale the continuum deformation. The atoms are assumed to undergo the same transformation than the continuum. It has however been shown to yield inconsistent results since the atom positions should be allowed to relax, thus yielding a heterogeneous strain field [384, 385]. This is particularly true when dealing with material surfaces [386], which are known to undergo large surface relaxations over very small distances (typically few atomic layers). Interestingly, it has been proposed to use higher-order elasticity to overcome this difficulty [384, 387], which was also mentioned above as a way to describe size-dependent elasticity.

It has been shown at a very early stage of the development of higher-order elasticity theories that these could provide a continuum counterpart to lattice dynamics studies [388]. Using a strain gradient theory, Toupin has shown that the introduced hyper-stresses could render the above-mentioned surface relaxation. This was however possible only in non-centrosymmetric materials, and considering a symmetric material slab of a cubic material was resulting in a non-symmetrical displacement field [388]. Soon later, Mindlin demonstrated that additionally considering the second strain gradient allows to circumvent these weaknesses [389]. Among the introduced material parameters, one is called **cohesion modulus** and is shown to be analogous to the surface tension in liquids. This cohesion modulus is thus a material property (contrary to the above-described extrinsic surface stresses) and controls the surface relaxation. A surface chemical modification is thus expected to affect this material parameter, therefore resulting in a mechanical deformation. Though particularly promising, using such a framework requires to have access to numerical values of the numerous material parameters. Besides lattice dynamics [390, 391, 392], inelastic neutron scattering [393] and picosecond laser ultrasound measurements [394] yield some higher-order elasticity parameters at a very high frequency (typically 1 THz), thus making the meaning of these values for quasi-static applications questionable.

This highlights the need for experimental methods able to provide the material parameters involved in the above-mentioned frameworks, which meets the possibility to access extremely rich data sets on micro-cantilever structures. The following of this chapter is thus organized as follows: Sect. 2 describes experimental tools developed to provide both a testing platform for chemo-mechanical couplings and full-field data necessary to retrieve the necessary modeling parameters. Sect. 3 then presents two distinct frameworks together with the adequate identification procedure exploiting the full-field measurements as obtained with the set-up described in Sect. 2.

2 Experimental developments

Building a modeling of chemo-mechanical couplings first requires a model system for which the implementation of the coupling is easy and the required know-how is widespread. Electrochemistry provides such a way to chemically control surfaces, and significant efforts have already been put on the development of thermodynamically relevant frameworks to describe the observed effects (see Sect. 1.2). The focus is on one-dimensional mechanical systems for the sake of simplicity. Studying such chemo-mechanical couplings additionally requires a set-up providing access to both kinematic and chemical descriptions of the surface under scrutiny.

This section thus focuses on two specific experimental developments. Sect. 2.1 describes some micro-fabrication efforts to obtain arrays of cantilevers one surface of which is electrically-controlled. Sect. 2.2 then describes a multiple-wavelength microscope intended to simultaneously provide kinematic and chemical field data of surfaces under scrutiny.

2.1 Electrochemically-controlled cantilever sensors

This section details a new design and fabrication process of a multiple-thickness electrochemical cantilever sensor as reported in [395]. Each cantilever can act not only as a functionalized cantilever, but also as an independent working electrode (WE) for electrochemical measurements. As mentioned in Sect.1.2, the way the chemically-induced mechanical deformation scales with the cantilever thickness is expected to be discriminant among modeling frameworks. It is thus desirable for modeling purposes to have cantilevers featuring different thicknesses simultaneously available. The different thicknesses of the silicon nitride layer are achieved by successive masking and reactive ion etching of partially overlapping openings at a low etch rate (few tens of nanometers per minute). Small thickness gaps ($< 30nm$) are then successfully obtained. One advantage of this fabrication process is that the thickness distribution of cantilevers can be altered and broadened by combination of different RIE recipes or modification of the etching time. In addition, the integration of the cantilever chip with a fluidic cell, a printed circuit board (PCB) and a temperature-controlled plate to form a hybrid system is also addressed.

2.1.1 Configuration of the hybrid system

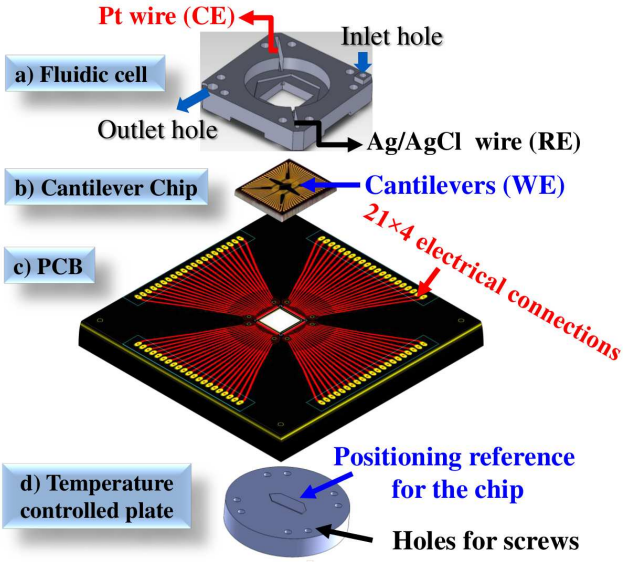

Figure 2.2: Overview of the full assembly.

The proposed hybrid system is depicted in Fig. 2.2, integrating a fluidic cell, the cantilever chip, a printed circuit board (PCB), and a temperature-controlled plate. The fluidic cell is designed to hold liquid and to set an electrochemical cell (3 electrodes arrangement). It provides fluidic inlet and outlet, and includes two channels for inserting a reference electrode (RE) and a counter electrode (CE). The cantilever chip includes four identical cantilever arrays. Each cantilever array houses 20 cantilever beams featuring

different thicknesses. Each cantilever is used as an independent working electrode (WE). A home-made PCB is designed to electrically connect the cantilever chip by wire bonding. A square hole (12.8mm $\times$ 12.8mm) in the middle of the PCB allows the backside of the cantilever chip to directly contact a temperature-controlled plate. A positioning reference is used to achieve a reproducible positioning of the chip with respect to the temperature-controlled plate.

2.1.2 Fluidic cell

The fluidic cell is designed by using a CAD software and fabricated using a 3D printer (3D Systems ProJet^{TM} SD 3500). The obtained poly-(methyl-methacrylate) (PMMA) fluidic cell is shown in Fig. 2.2. It is 3.8 mm thick, 22 mm wide, and 22 mm long. A 0.5 mm-thick hexagon step around the cavity is designed to glue a pyrex cover-glass (10 mm diameter, 0.17 mm thick, not shown in Fig. 2.2). The whole fluidic chamber volume is 37μL when using the cover glass. 8 holes are used to insert 4 rods for positioning the fluidic cell with respect to the front side of the cantilever chip, and 4 screws are used to tighten the full assembly.

2.1.3 Cantilever chip

The proposed chip features: a) a positioning reference on the backside, b) multiple cantilever thicknesses on the front side, c) an electrode layer, d) an electrical connection layer, and e) an insulation layer. In the following, the fabrication process is described by using two cross sections and by focusing on cantilever No. 9, shown in Fig. 2.3.

- In Fig. 2.3b, low-stress silicon nitride is first deposited onto both sides of a 4-inch, 500μm thick, silicon (100) wafer with by Low Pressure Chemical Vapor Deposition (LPCVD) (NH3/SiH2Cll2:18/60 sccm, temperature: 820°C, pressure: 200 mTorr, time: 180 min). The final silicon nitride thickness is measured to be about 805 nm. After baking the wafer for 10 min at 120°C, the wafer is spin-coated with a 2.4μm thick layer of SPR 220-3.0 positive photoresist. Then, the photoresist is exposed to UV irradiation (365 nm, 300 mJ.cm^{-2}) through a mask with the designed alignment reference pattern. After developing the photoresist with the MF-26A developer for 75 s, the exposed silicon nitride is reactive ion etched at a 26 nm/min etch rate (Pressure: 60μbar, CHF_3/C_2F_6: 10/5 sccm, DC bias: 245 V; RIE PLASSYS). Afterwards, the photoresist is stripped.

- The cantilever beams (15μm wide and 80μm long) are similarly patterned on the front side of the wafer by using double-side EVG 620 alignment system. The cantilever beams are then defined by reactive ion etching (RIE) of the exposed silicon nitride layer (shown in Fig. 2.3c). The whole etching time (40 min) is divided into two 20 min etching steps, with a 30 s oxygen surface cleaning process (20 sccm, 60μbar, 95 W, 410 V) in-between. The photoresist is then stripped.

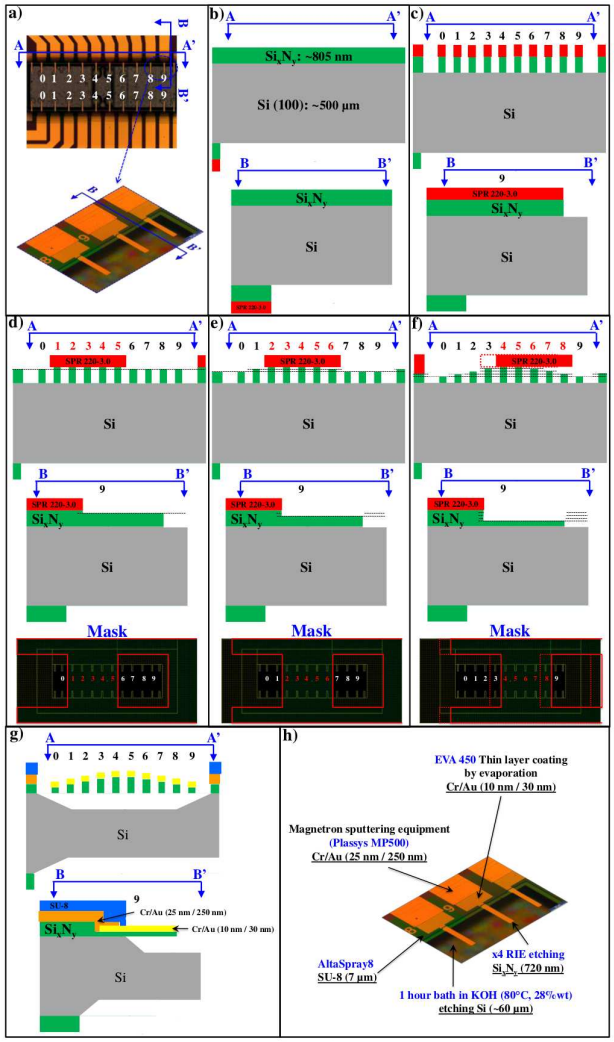

Figure 2.3: Overview of the process flow.

- To achieve different cantilever thicknesses, a single mask is specially designed and successively used with different alignment marks. Using this mask referring to alignment mark 1 (shown in Fig. 2.3d), some of the cantilever beams are firstly covered by photoresist (SPR 220-3.0, 2.4 μm thick). The photoresist pattern is used as an etching mask in the RIE etching process with a low etch rate (10.8 nm/min, 15.8 nm/min, 20.1 nm/min, or 26.5 nm/min) for 1 min. Shifting the mask by referring to mark 2 (shown in Fig. 2.3e), partially overlapping openings are photo-patterned and etched by another 1 min RIE step. In Fig. 2.3f, this step is repeated twice by shifting the mask referring to mark 3 and mark 4, successively. By repeating the photo-patterning and etching of partially overlapping openings, different thicknesses are thus achieved.

- As displayed in Fig. 2.3g, a Cr/Au (10 nm / 30 nm) electrode layer is deposited

Table 2.1: Process parameters for reaction ion etching (RIE).

Recipe	N. 1	N. 2	N. 3	N. 4
Pressure (μbar)	60	60	60	60
Power (W)	40	40	40	45
CHF_3 flow rate (sccm)	10	10	10	15
C_2F_6 flow rate (sccm)	5	5	5	5
DC bias voltage (V)	230	238	245	253
Etch rate at center (nm/min)	10.8	15.8	20.1	26.5
Standard deviation (nm/min)	1.06	0.68	0.86	0.71

by electron beam evaporation (EVA 450, Alliance Concept), and then lifted-off in selected areas by dissolving the underlying photoresist. In order to independently bridge the electrode layer to electrode pads on borders of the chip, one electrical connection layer is added. This connection layer (Cr/Au: 20 nm / 250 nm) is sputtered (MP 500, PLASSYS) and also shaped by lift-off process. A potassium hydroxide (KOH) solution (28 % wt., 1 hour at 80°C) is used to etch 60 μm of silicon on both sides of the wafer, thus releasing the cantilevers and defining the alignment reference. Finally, the electrical connections are insulated by spray coating (AltaSpray 8) a 7 μm thick SU-8 layer.

2.1.4 Experimental validation

The repeatability and stability of RIE The repeatability and stability of RIE is critical to obtain well-defined thickness gaps. By using the RIE PLASSYS machine, we have developed four recipes (shown in TAB.2.1). Keeping the same pressure and the same gas flow rates, we can obtain four different etch rates by changing the DC bias voltage. As shown in TAB.2.1, the scatter on the etch rates are low enough to allow for a precise control of the thickness gaps.

The produced cantilever chip As seen in Fig. 2.4a, a produced chip (12.55mm $\times$ 12.55mm) includes four identical cantilever arrays. Each cantilever array houses 20 cantilever beams serving both as a functional cantilever and also as an independent WE. These cantilevers are divided into 4 groups. Each group contains cantilevers having five different thicknesses. In addition, there is a large opening on the backside, which is the alignment reference for achieving a reproducible positioning of the chip with respect to the temperature-controlled plate. Fig. 2.4b shows an SEM picture of one group of cantilevers with 5 different thicknesses of silicon nitride (t_1, t_2, t_3, t_4 or t_5). Fig. 2.4c is an SEM picture of a single cantilever. The cantilever is measured to be 14.7 μm wide and 80.7 μm long. These values are very close to our design (15μm wide and 80μm long). Fig. 2.4d is a cross-section of a 780 nm thick cantilever.

One can observe that a thin layer of Cr/Au is above the silicon nitride layer. To observe

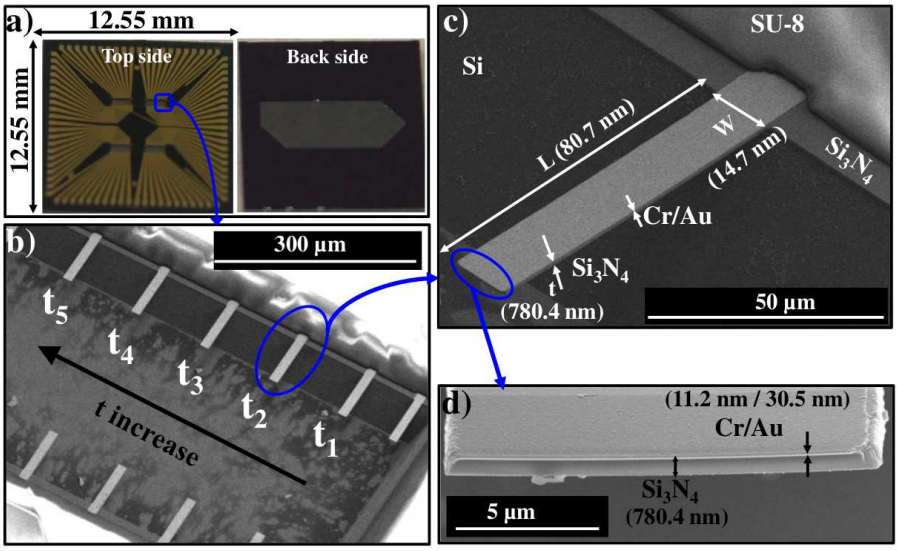

Figure 2.4: Views of the produced cantilever arrays.

the resulting diversity of silicon nitride thicknesses, focused ion beam (FIB) is used to cut the tip of the cantilever. A Cr layer is firstly deposited to protect the top layer ($\sim$ 120 nm, Fig. 2.5a). After using FIB tool (Helios NanoLab 600i), SEM pictures of the cross-section can be obtained for each cantilever. Fig. 2.5b shows an example of the thickness distribution obtained by using different RIE recipes. The thickness t_5 is defined by the LPCVD deposition process. RIE recipe No.4 is used for 1 min to get a 26 nm difference between t_4 and t_5 and thus achieve t_4. We similarly use Recipes No.3 and No.2 to obtain t_3, t_2 and t_1. The results are close to the target values. It should be highlighted that it is also possible to get different thickness distributions by using the same RIE recipe with different etching times.

Assembly of the hybrid system The hybrid system assembly is depicted in Fig. 2.6. First, the cantilever chip is glued to the PCB. The electrical interconnection between gold contact pads on the chip and copper connections on the PCB is established by wire bonding (ball-wedge bonder) with an Au wire ($50-60\,\mu$m thick, $25\,\mu$m diameter). Then, four rods are used to mount the fluidic cell onto the PCB, and the fluidic cell is bonded to the front face of the chip with SU-8 photoresist applied on its backside. The PMMA fluidic cell holds two Teflon tubings, one platinum wire and one silver-silver chloride wire, used for pouring solutions and for setting an electrochemical cell, respectively. Finally, the full assembly is mounted on the temperature-controlled plate with screws (not shown).

2.2 Multiple wavelengths microscopy

In order to obtain spatially resolved data, it was proposed in [396] to use multiple wavelengths imaging reflection microscopy, which provides both local surface modifications

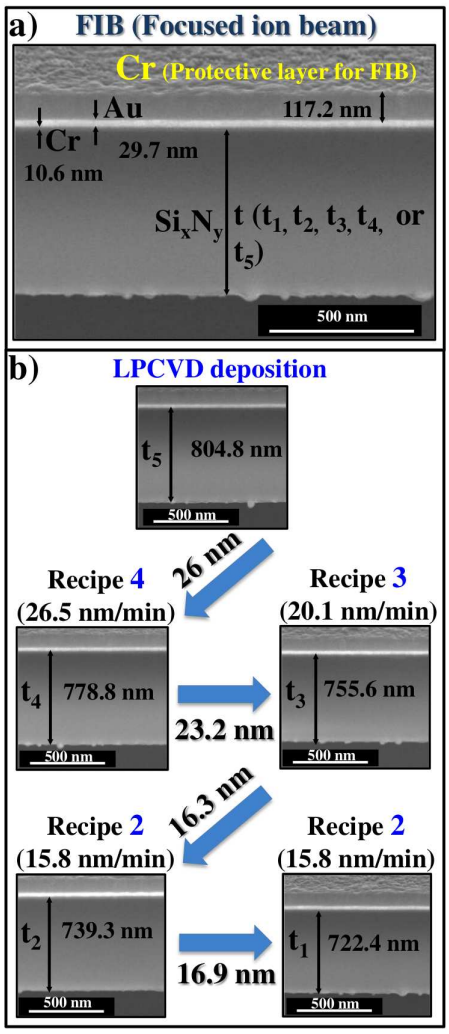

Figure 2.5: Typical etching sequence.

and kinematic field measurements. A decoupling method is presented to distinguish wavelength-dependent and -independent (*i.e.,* kinematic) contributions to the collected intensity. The method is exemplified by monitoring the electro-elastic coupling on a cantilever beam, allowing one to simultaneously obtain an electroreflectance mapping and a field related to the local surface rotation of micrometer-sized structures.

Monitoring the differential reflectance of surfaces has already proven to provide access to various observable thermodynamic variables describing surfaces. Differential reflectance changes detections have for instance been achieved to perform sensitive electroreflectance [397] and thermoreflectance [398] measurements, providing access to electrochemically induced effects at substrate-electrolyte interfaces and surface temperature fields. This section thus describes a set-up simultaneously providing the surface deformation and surface differential reflectance.

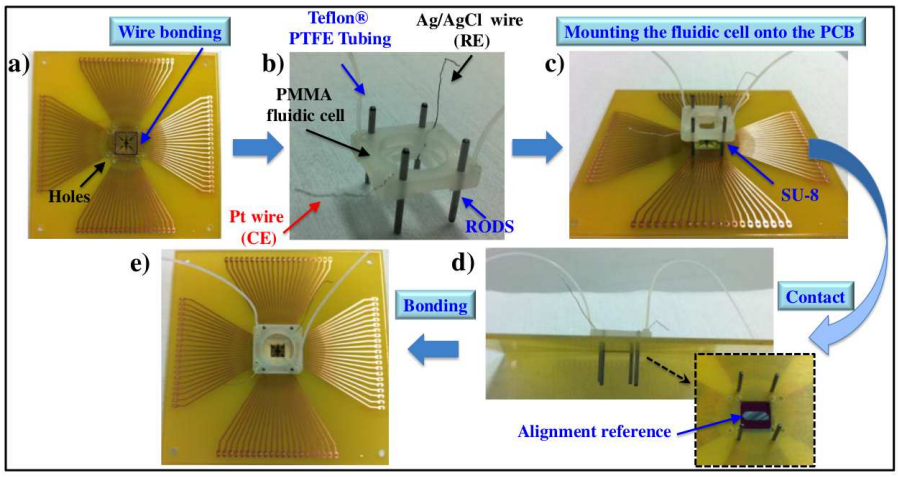

Figure 2.6: Assembly procedure.

Using a microscope, the reflected intensity fields are recorded for two different illumination wavelengths. Decoupling the wavelength-independent and -dependent contributions to the measured relative intensity changes then yields the sought fields.

2.2.1 Set-up

To study coupled surface phenomena at the micrometer scale, deformable mechanical microcantilevers are subjected to time dependent actuation. The objects under scrutiny are observed with an objective lens and imaged on a CCD array (Dalsa 1M30, 12 bits, 1024 $\times$ 1024 pixels) using focusing optics (focal length 180 mm, see Fig. 2.7a). Reflected intensity changes arise either from surface reflectivity or from collection efficiency changes. The former is usually wavelength-dependent (as with electro- or thermoreflectance) while the latter is wavelength-independent since it depends on the surface orientation and on the numerical aperture of the objective lens, which is corrected for chromatic aberrations (Fig. 2.7b). In order to distinguish the wavelength-dependent and -independent contributions, the sample is illuminated with a green and a red light emitting diode (LEDs) of different wavelengths, namely λ_G=505 nm and λ_R=625 nm. These diodes are sequentially triggered by a 1.8 s period signal, provided by a function generator (Fig. 2.7c) and N sums of 10 images are acquired for each illumination wavelength. The intensity I_m collected by the pixel P reads

$$I_m(P,\lambda,t_n) = I_i(P,\lambda)R(P,\lambda,t_n)\zeta(\theta(P),t_n) \tag{2.1}$$

where $I_i(P,\lambda)$ is the intensity impinging on the surface conjugated with pixel P at wavelength λ, $R(P,\lambda,t_n)$ the reflectivity of the surface, *i.e.,* the ratio of the reflected and incident intensities, depending on a local parameter $X(P,t_n)$ (such as electrical charge, temperature, etc.) at the time step t_n. $\zeta(\theta(P),t_n)$ is the collection rate related to the local surface orientation $\theta(P)$. The influence of $X(P,t_n)$ on the reflectivity is assumed to be small, so

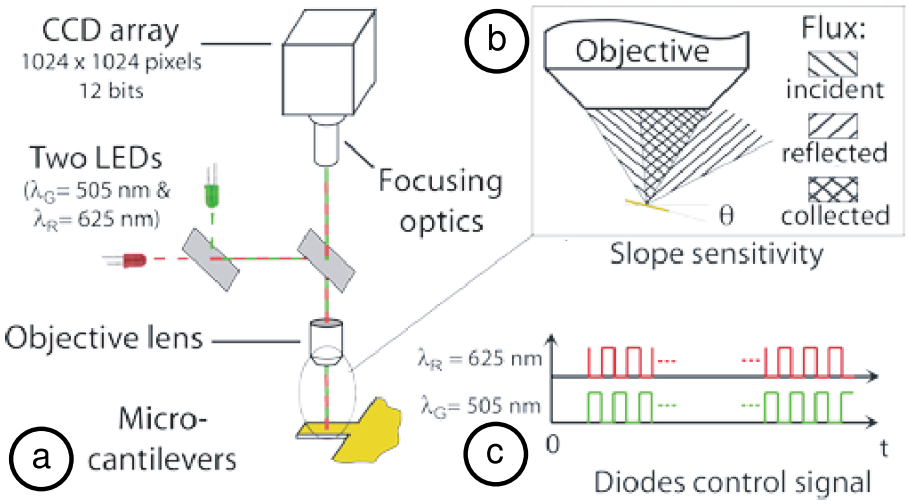

Figure 2.7: a: Experimental set-up with two sequentially triggered sources, b: Sensitivity of the collected intensity to the surface orientation, c: Light sources timing.

that R is linearized

$$R(P,\lambda,t_n) = R_0(P,\lambda)[1 + r(\lambda)X(P,t_n)] \tag{2.2}$$

with $r(\lambda) = \frac{1}{R_0}\frac{\partial R}{\partial X}$ the relative reflectance sensitivity to the controlled parameter X. The geometrical effect $\zeta(\theta(P),t_n)$ is linearized in the case of small surface rotations about the initial orientation $\theta_0(P)$

$$\begin{aligned}\zeta(\theta(P),t_n) &= \\ &\varepsilon_0(\theta_0(P))\,[1 + d_{\theta_0}(P)(\theta(P,t_n) - \theta_0(P))]\end{aligned} \tag{2.3}$$

with $d_{\theta_0}(P) = \frac{1}{\zeta_0}\frac{\partial \zeta}{\partial \theta}$ the local slope sensitivity. Finally, the measured intensity linearly depends on the wavelength-independent and -dependent relative intensity changes $R_{wi}(P,t)$ and $R_{wd}(\lambda,P,t)$, respectively

$$\begin{aligned}I_m(P,\lambda,t_n) &= \\ &I_a(P,\lambda)\,[1 + R_{wd}(\lambda,P,t_n) + R_{wi}(P,t_n)]\end{aligned} \tag{2.4}$$

with

$$\begin{aligned} I_a(P,\lambda) &= I_i(P,\lambda)R_0(P,\lambda)\zeta_0(\theta_0(P)) \\ R_{wd}(\lambda,P,t_n) &= r(\lambda)X(P,t_n) \\ R_{wi}(P,t_n) &= d_{\theta_0}(P)(\theta(P,t_n) - \theta_0(P)) \end{aligned}$$

2.2.2 Decoupling procedure

For a given (P,t_n), Eq.(2.4) is recast as a linear system

$$\begin{bmatrix} I_m(\lambda_R) - I_a(\lambda_R) \\ I_m(\lambda_G) - I_a(\lambda_G) \end{bmatrix} = \begin{bmatrix} I_a(\lambda_R) & I_a(\lambda_R) \\ k\, I_a(\lambda_G) & I_a(\lambda_G) \end{bmatrix} \begin{bmatrix} R_{wd}(\lambda_R) \\ R_{wi} \end{bmatrix} \tag{2.5}$$

where the ratio $k = r(\lambda_G)/r(\lambda_R)$ is assumed to be different from 1. The scalar k and the initial intensity fields $I_a(P,\lambda)$ are obtained by pre-processing the data. Over the rigid substrate Ω_s, the local charge density $X(P,t_n)$ is assumed to be equal to the mean charge density $X_i(t_n)$, so that at a given location, $I_a^{sol}(P,\lambda)$ is obtained as a minimizer (for a given set $\{c_q\}$) of the objective function $\eta^2(P,\lambda,I_a(P,\lambda),\{c_q\})$

$$\eta^2(P,\lambda,I_a(P,\lambda),\{c_q\}) = \sum_{n=1}^{N} \left(I_m(P,\lambda,t_n) - I_a(P,\lambda) f(X_i,\{c_q\})\right)^2 \tag{2.6}$$

with

$$f(X_i,\{c_q\}) = 1 + \sum_{q=1}^{Q} c_q X_i^q(t_n) \tag{2.7}$$

The coefficients $\{c_q\}$ are obtained as the minimizers of the sum κ^2 over Ω_s of the minimal η^2

$$\kappa_R^2(\lambda,\{c_q\}) = \sum_{P\in\Omega_s} \eta^2(P,\lambda,I_a^{sol}(P,\lambda),\{c_q\}) \tag{2.8}$$

The ratios $r(\lambda)$ are then obtained as the coefficient c_1 identified when considering a large area Ω_s. Repeating this procedure over the cantilever surface Ω_c (instead of Ω_s) gathering all the pixels at a given abscissa along the cantilever axis then yields $I_a(P,\lambda)$ for these points. Values of Q above 6 have been found to provide r values independent of Q. Solving Eq. (2.5) then yields the relative intensity change contributions. The local slope sensitivity field $d_{\theta_0}(P)$ is obtained by a calibration procedure.

2.2.3 Example

The used mechanical structures are silica microcantilevers ($70\times20\times0.77\ \mu m^3$), covered with a 20 nm titanium adhesion layer and a 50 nm gold layer. These devices are placed in a cell and observed with an immersion objective lens ($\times$20, Numerical Aperture 0.5). We focus here on the electromechanical effects induced by charging the gold surface. The cantilevers are immersed in a KCl electrolyte ($10^{-2}\ mol.l^{-1}$), and the electrical potential of their surface is controlled by an electrochemical workstation (CHI 660A) with respect to an Ag/AgCl reference electrode [332]. A total area of $A \simeq 50\,mm^2$ is in constant contact with the electrolytic solution. The gold surface is cleaned by varying its potential U_g from

0.1 to 0.8 V during three cycles at 12 $mV.s^{-1}$. Reference images are acquired and the potential is then swept between 0.1 to 0.46 V at 4 $mV.s^{-1}$ while recording the electrode charge $A \times X_i$. $N = 50$ sums of 10 images are sequentially acquired for each wavelength during the cycle.

The above-detailed pre-processing and decoupling procedure is applied to the recorded images $I_m(P, \lambda, t_n)$. The pre-processing yields $r(\lambda_R) = -162$ cm^{2}C^{-1} and $k = 2.03$, which is consistent with known results [399]. The calibration procedure exploits the bimaterial effect and also provides $d_{\theta_0}(P) \simeq 1$ rad^{-1} everywhere along the cantilever, so that the R_{wi} and $R_{wd}(\lambda_R)$ fields are easily converted in a surface rotation (and thus surface displacement) and local charge density fields respectively. The signal-to-noise ratio can be improved by averaging R_{wi} and $R_{wd}(\lambda_R)$ across the width of the beam. FIG.2.8 shows the change of the averages $\widetilde{R_{wi}}$ and $\widetilde{R_{wd}}(\lambda_R)$ as functions of time (vertical axis) along the axis of the beam (horizontal axis) which is anchored at $x = 0$.

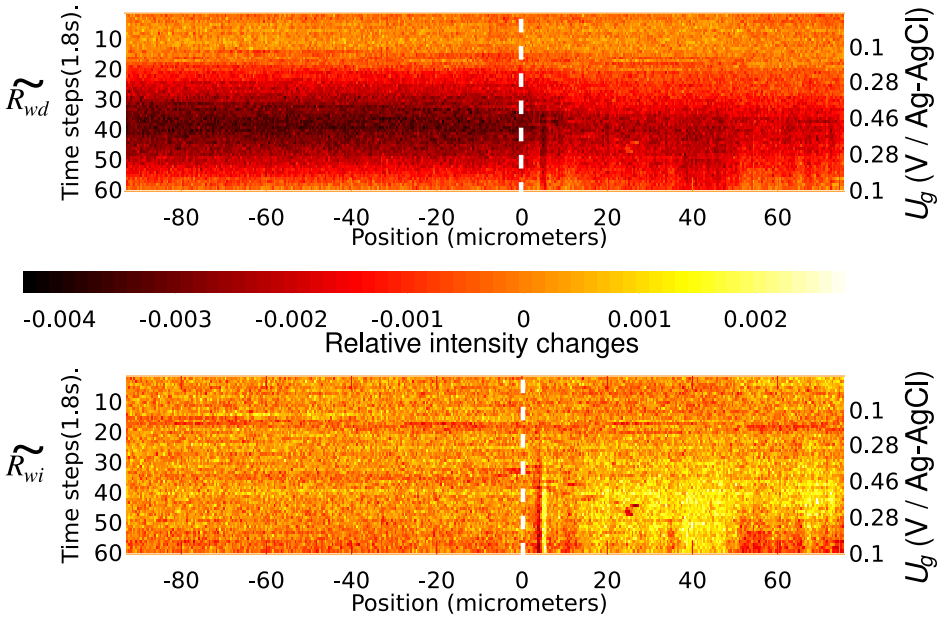

Figure 2.8: Relative intensity changes $\widetilde{R_{wd}}(\lambda_R)$ (top) and $\widetilde{R_{wi}}$ (bottom) identified along the substrate ($x \leq 0$) and the beam ($x \geq 0$) during the loading cycle (time along the vertical axis). The cantilever is anchored at $x = 0$ (dashed line).

$\widetilde{R_{wi}}$ does not vary on the substrate during the charging process, but increases up to 2×10^{-3} since the cantilever bends. This agrees with a mechanical effect acting only on deformable structures. $R_{wd}(\lambda_R, P, t_n)$ is related to the local charge density $X(P, t_n)$ and $\widetilde{R_{wd}}(\lambda_R)$, which is heterogeneous, decreases down to -4×10^{-3} on the substrate. In order to prove the electrochemical origin of the observed phenomena, FIG.2.9 depicts the changes of R_{wi} and R_{wd} averaged on the whole substrate and at the edge of the cantilever

(30% of its surface) as functions of the electrode charge $A \times X_i(t_n)$. Again, R_{wi} does

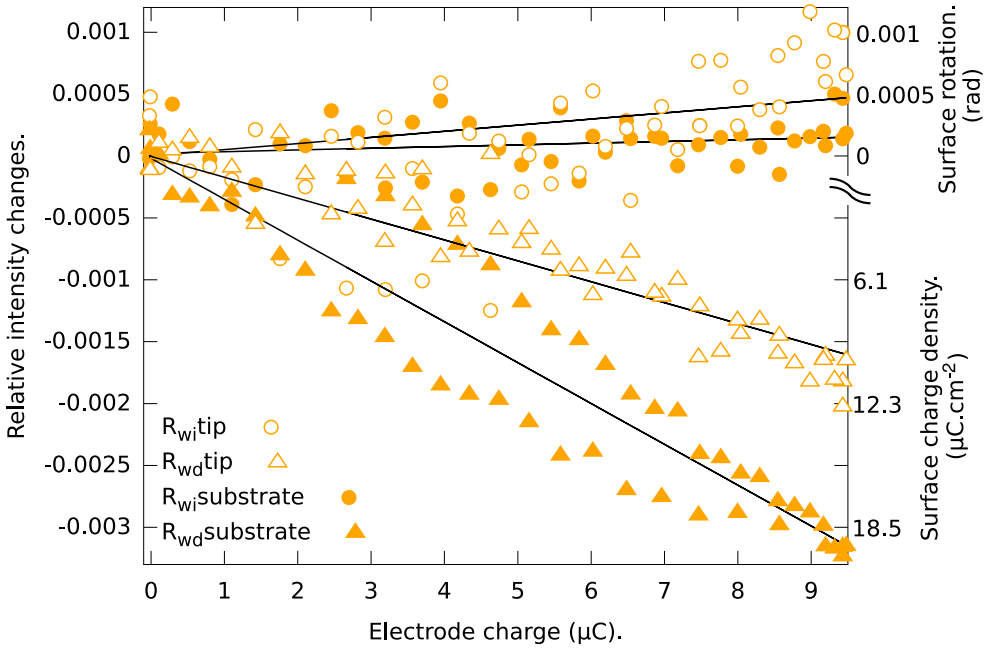

Figure 2.9: Averages of R_{wi} and R_{wd} on the substrate and at the end of the beam versus the electrode charge $A \times X_i$. The solid lines are linear fits to each data set. Calibrated values of the surface charge density (triangles) and surface rotation (circles) can be read on the right ordinate axis.

not significantly change on the substrate (FIG.2.9), which confirms its mechanical origin. All other evolutions are quasi-linear functions of the electrode charge, showing that the electrical charge density governs the mechanical effects and that the expansion (2.2) is valid. The R_{wd} contribution is twice larger on the substrate than at the cantilever tip (FIG.2.9), thereby proving that the charging process occurs heterogeneously along the cantilever. The deviation of R_{wd} obtained from the reference images yields an estimate of the standard deviation on the relative intensity changes: $\sigma_{R_{wd}} \simeq 10^{-2}$ for a single pixel, which is reduced by spatial averaging to $\sigma_{\widetilde{R_{wd}}} \simeq 10^{-4}$.

The technique described herein makes use of a standard reflection microscope with a CCD array and two sources of different wavelengths. Multi-physical phenomena occurring at their surface result in wavelength-dependent and -independent collected intensity variations, so that a procedure is proposed to decouple these contributions from intensity images at two different wavelengths. This method has been applied to microcantilevers under electrochemical actuation by varying the electrical potential of a substrate-aqueous electrolyte interface. The local charge density and rotation fields are obtained with a measurement reproducibility within the 10^{-4} range, thereby providing a powerful and simple way to study the multi-physical behavior of MEMS devices.

3 Surface effects modeling

This section presents two distinct frameworks together with the adequate identification procedure exploiting the full-field measurements provided by the multiple-wavelength microscope described in Sect. 2.2. For both approaches, the focus is put on calculating the response of a micro-fabricated structure subjected to a surface loading, without particular attention to the involved interactions at the molecular scale.

3.1 Asymptotic analysis

This section recalls an approach initially proposed in Ref. [400] and resembling the one proposed in Ref. [375]. The main difference is that instead of considering the Gurtin-Murdoch framework, and focusing on cantilever sensors, the chemical environment effect is represented by a mechanical layer, referred to as "the membrane" (bonded to the cantilever surface), whose thickness tends to zero. The mechanical parameters of this membrane are set using thermodynamic arguments (Sect. 3.1.1) so that the membrane is said to be a thermodynamic-equivalent layer (TEL). The solution for the interfacial shear-stress field is obtained by using the asymptotic expansion method [401, 402, 403].

3.1.1 Definition of the accompanying mechanical modeling

This section describes the accompanying mechanical modeling intended to render the chemical part of the system free energy and its dependence on the surface amount. Let us consider a representative interface element whose size is:

- small enough to satisfy the definiteness of partial derivatives involved in continuum mechanics;
- large enough to provide a representative description of the surface mechanical behavior.

These requirements are referred to as scale separation conditions in the following. For polycrystalline thin films, a representative element should then include at least 100 grains. Three phases are classically distinguished inside this interfacial element:

- a liquid phase, whose volume is V at pressure p. Several other state variables, denoted by the set $\{n_L^\alpha\}$, represent the amount of species α in the liquid phase, and thus describe its composition;
- the interphase, whose surface is S_i and composition is described by the set $\left\{n_S^\alpha\right\}$;
- the solid phase, whose surface is S_i, described by its stress field σ.

This system is assumed to be closed, in equilibrium with an external thermostat. The system is described by its Gibbs' free enthalpy $\mathcal{G}$. If the scale separation conditions are met, then the state variables set $\left\{T, p, \left\{\frac{n_L^\alpha}{V}\right\}, \left\{\frac{n_S^\alpha}{S_i}\right\}, \sigma\right\}$ describes the local interfacial

state. In particular, the initial state corresponds to the sets $\left\{n^{\alpha}_{L,0}\right\}$ and $\left\{n^{\alpha}_{S,0}\right\}$. As one deals with a closed system, the conservation conditions lead to

$$dn^{\alpha}_{L} = -\beta^{\alpha} \tag{2.9}$$
$$dn^{\alpha}_{S} = \beta^{\alpha} \tag{2.10}$$

where β^{α} is the processed quantity for species α by the reaction

$$\alpha_{liquid} \xrightarrow{\beta^{\alpha}} \alpha_{interphase}$$

The system free enthalpy $\mathcal{G}$ reads

$$\mathcal{G} = \mathcal{G}_L + \mathcal{G}_S + \mathcal{G}_m = \mathcal{G}_c + \mathcal{G}_m \tag{2.11}$$

where $\mathcal{G}_L$ is the liquid phase contribution, $\mathcal{G}_S$ is the interphase one and $\mathcal{G}_m$ arises from the solid substrate. The first two terms are formally merged into $\mathcal{G}_c$, which represents the chemical part in $\mathcal{G}$. Each free enthalpy contribution is expressed as a function of the state variables:

- the liquid phase is assumed to be an ideal solution, so that considering a unit volume, $\mathcal{G}_L$ reads

$$\mathcal{G}_L\left(p,T,\left\{\frac{n^{\alpha}_{L}}{V}\right\}\right) = \sum_{\alpha}\frac{n^{\alpha}_{L}}{V}\left[\mu^{\alpha}_{L,0}(p,T) + RT\log\left(\frac{n^{\alpha}_{L}}{V}\right)\right] \tag{2.12}$$

  where $\mu^{\alpha}_{L,0}(p,T)$ is the reference chemical potential at temperature T and pressure p for species α, R the molar gas constant.

- For the sake of generality, the following form for an elementary interphase portion is considered

$$\mathcal{G}_S\left(p,T,\left\{\frac{n^{\alpha}_{S}}{S_i}\right\}\right) = g\left(T,\left\{\frac{n^{\alpha}_{S}}{S_i}\right\}\right) + \sum_{\alpha}\left[\frac{n^{\alpha}_{S}}{S_i}\mu^{\alpha}_{S,0}(p,T)\right] \tag{2.13}$$

  where the function $g\left(T,\left\{\frac{n^{\alpha}_{S}}{S_i}\right\}\right)$ has to be chosen to represent the evolution of the adsorbate free enthalpy as a function of the surface concentration. For instance, a non-interacting adsorbate would lead to choose an expression g_{ni} for g similar to the one used in equation (2.12)

$$g_{ni}\left(T,\left\{\frac{n^{\alpha}_{S}}{S_i}\right\}\right) = RT\sum_{\alpha}\frac{n^{\alpha}_{S}}{S_i}\log\left(\frac{n^{\alpha}_{S}}{S_i}\right) \tag{2.14}$$

Setting $S_i = S_0 + dS$, the chemical part of the overall free enthalpy reads

$$\begin{aligned}\mathcal{G}_c(S_i) &= \sum_\alpha \left[\frac{n^\alpha_{L,0} - \beta^\alpha}{V} \left[\mu^\alpha_{L,0}(p,T) + RT \log\left(\frac{n^\alpha_{L,0} - \beta^\alpha}{V} \right) \right] \right. \\ &\quad \left. + \frac{n^\alpha_{S,0} + \beta^\alpha}{S_0 + dS} \mu^\alpha_{S,0}(p,T) \right] + g\left(T, \left\{ \frac{n^\alpha_{S,0} + \beta^\alpha}{S_0 + dS} \right\} \right) \end{aligned} \tag{2.15}$$

The chemical contribution to the free enthalpy depends on the available surface amount. Considering small area variations

$$\begin{aligned}\mathcal{G}_c(S_i) \simeq \mathcal{G}_c(S_0) + \frac{1}{S_0} \sum_\alpha \left[- \left((n^\alpha_{S,0} + \beta^\alpha) \mu^\alpha_{S,0}(p,T) + \frac{\partial g}{\partial \left(\frac{n^\alpha_S}{S_i} \right)} \right) \frac{dS}{S_0} \right. \\ \left. + \left((n^\alpha_{S,0} + \beta^\alpha) \mu^\alpha_{S,0}(p,T) + \frac{\partial g}{\partial \frac{n^\alpha_S}{S_i}} + \frac{1}{2S_0} \frac{\partial^2 g}{\partial \left(\frac{n^\alpha_S}{S_i} \right)^2} \right) \left(\frac{dS}{S_0} \right)^2 \right] + o\left(\frac{dS}{S_0} \right)^3 \end{aligned} \tag{2.16}$$

Finally, both $\mathcal{G}_c$ and $\mathcal{G}_m$ depend on the available surface area. To include this shared dependence in the mechanical modeling of cantilevers, it is assumed that there is a thermodynamically equivalent layer (TEL) bonded to the surface under scrutiny, so that this surface and the TEL are constrained to deform together.

Moreover, it is considered that the TEL is subjected to a free strain ε_L. This local free strain value is identified by minimizing the free enthalpy assuming that no mechanical constrain is acting on the TEL, that is by minimizing the chemical term $\mathcal{G}_c$ with respect to the surface variation dS. Assuming that expansion (2.16) holds, ε_L satisfies

$$\begin{aligned} 2 \times \varepsilon_L \times \sum_\alpha \left[(n^\alpha_{S,0} + \beta^\alpha) \mu^\alpha_{S,0}(p,T) + \frac{\partial g}{\partial \left(\frac{n^\alpha_S}{S_i} \right)} + \frac{1}{2S_0} \frac{\partial^2 g}{\partial \left(\frac{n^\alpha_S}{S_i} \right)^2} \right] \\ - \sum_\alpha \left[(n^\alpha_{S,0} + \beta^\alpha) \mu^\alpha_{S,0}(p,T) + \frac{\partial g}{\partial \left(\frac{n^\alpha_S}{S_i} \right)} \right] = 0 \end{aligned} \tag{2.17}$$

If one prescribes, by any external mean, the TEL strain to be $\varepsilon_L + \delta\varepsilon$, its free enthalpy variation reads

$$\Delta \mathcal{G}_c = \left((n^\alpha_{S,0} + \beta^\alpha) \mu^\alpha_{S,0}(p,T) + \frac{\partial g}{\partial \left(\frac{n^\alpha_S}{S_i} \right)} + \frac{1}{2S_0} \frac{\partial^2 g}{\partial \left(\frac{n^\alpha_S}{S_i} \right)^2} \right) (\delta\varepsilon)^2 \tag{2.18}$$

By analogy with the strain energy of a membrane, one is able to represent chemical effects by a bonded thermodynamically equivalent membrane, whose thickness is denoted by e_v,

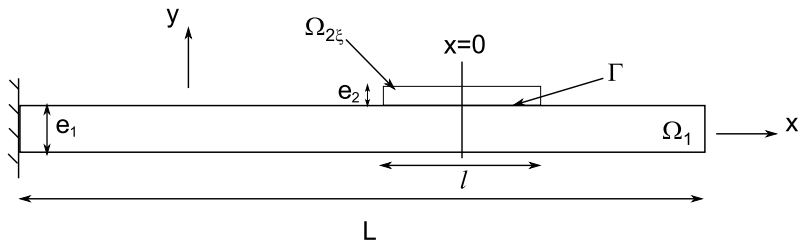

Figure 2.10: Schematic view of the accompanying mechanical model.

whose Young's modulus E_v reads

$$E_v = \frac{2}{e_v S_0}\left((n^{\alpha}_{S,0}+\beta^{\alpha})\mu^{\alpha}_{S,0}(p,T)+\frac{\partial g}{\partial\left(\frac{n^{\alpha}_S}{S_i}\right)}+\frac{1}{2S_0}\frac{\partial^2 g}{\partial\left(\frac{n^{\alpha}_S}{S_i}\right)^2}\right) \tag{2.19}$$

and whose free-strain satisfies (2.17). Eqs (2.17) and (2.19) thus define, for a given membrane thickness e_v, an energetically equivalent mechanical modeling for the chemical effects. In addition to this energy equivalence, to account for the 2D nature of the phenomena under scrutiny, it is assumed that the thermodynamically equivalent membrane thickness is small compared with that of the considered substrate. Consequently, the chemical effects are described by a thermodynamically equivalent membrane whose thickness is small compared with the others, and which is constrained to deform together with the substrate surface, thus defining an accompanying mechanical modeling.

3.1.2 Initial problem

The system is modeled as described in FIG.2.10. The parameters related to the beam are denoted with the subscript $_c$, whereas those related to the thin layer (the membrane) are denoted with the subscript $_l$. The behavior of both phases is assumed to be linear elastic. The beam obeys an Euler-Bernoulli kinematics, has a Young's modulus E_c, width b, length L and thickness e_c. This beam is then subjected to an axial free strain $\varepsilon_{L1}(x)$. A thin membrane (whose Young's modulus is E_l, width b, length $l < L$ and thickness e_l) is constrained to deform together with beam along the interface Γ when subjected to a free strain field $\varepsilon_{L2}(x)$, $(-\frac{l}{2}) < x < (\frac{l}{2})$ (one sets $x = 0$ at the center of the membrane area). Denoting by σ_c the Cauchy stress tensor in the cantilever, the interactions between the two beams are then represented by the scalar field $\tau(x)$ (shear-stress)

$$\sigma_c \mathbf{y} = \tau(x)\mathbf{x} \tag{2.20}$$

where $\mathbf{x}$ denotes the unit vector in the cantilever's direction and $\mathbf{y}$ the outgoing normal to its upper surface. The equilibrium conditions read

$$\frac{dN_c}{dx}+\tau b = 0 \tag{2.21}$$

$$\frac{dM_c}{dx}-\tau b\frac{e_c}{2} = 0 \tag{2.22}$$

for the cantilever and

$$\frac{dN_l}{dx} - \tau b = 0 \tag{2.23}$$

for the membrane, where N_i is the normal force in phase i and M_i the bending moment. It should be noted that the proposed modeling is expected to somehow fail to represent the mechanical effect induced by adsorbates subjected to strong in-plane interactions such as electrostatic interactions, since this would require to take the adsorbate's bending stiffness into account. The tension and bending problems are assumed to be decoupled for the cantilever, so that the constitutive law reads

$$M_c = E_c I_c \frac{d^2 w}{dx^2} \tag{2.24}$$

where $E_c I_c$ is the bending stiffness for the cantilever in the middle of the cross-section (homogeneous cantilever), $w(x)$ the out-of-plane displacement field of the assembly. At this point, it should be underlined that using a beam or membrane theory corresponds to specific forms for the Cauchy stress tensor and displacement (strain) fields inside the phases. According to St-Venant's principle, the computed fields will then be correctly predicted "far enough" from the loading application points, that is, in the described case, "far enough" from the interface. As a consequence, to describe the displacement at the interface, it is required to take into account the "local" contribution of the displacement field (*i.e.,* close to the interface) in addition to the long-range displacement field provided by beam or membrane theories. A closed-form solution to this local contribution is obtained using Kolossov-Muskhelishvili potentials [404] and expanding the shear-stress field onto a Legendre polynomial basis [400].

For the sake of simplicity, let us consider uniform free strain fields

$$\varepsilon_{Li}(x) = \varepsilon_{Li} \qquad i \in \{1,2\} \tag{2.25}$$

The plane displacement on the interface for both the cantilever and the membrane read

$$\begin{aligned} u_c(x) - u_c\left(-\frac{l}{2}\right) &= \varepsilon_{L1} \times \left(x + \frac{l}{2}\right) + \int_{-\frac{l}{2}}^{x} \frac{N_c(\zeta)}{b e_c E_c} d\zeta \\ &\quad - \frac{e_c}{2} \int_{-\frac{l}{2}}^{x} \frac{d^2 w}{d\zeta^2}(\zeta) d\zeta + \sum_{k=0}^{\infty} \tau_k v_k(x) \end{aligned} \tag{2.26}$$

$$\begin{aligned} u_l(x) - u_l\left(-\frac{l}{2}\right) &= \varepsilon_{L2} \times \left(x + \frac{l}{2}\right) + \int_{-\frac{l}{2}}^{x} \frac{N_l(\zeta)}{b e_l E_l} d\zeta \\ &\quad + \frac{e_l}{2} \int_{-\frac{l}{2}}^{x} \frac{d^2 w}{d\zeta^2}(\zeta) d\zeta \end{aligned} \tag{2.27}$$

The kinematic compatibility condition at the interface reads

$$u_c(x) - u_c\left(-\frac{l}{2}\right) = u_l(x) - u_l\left(-\frac{l}{2}\right) \tag{2.28}$$

and has to be satisfied $\forall x, -\frac{l}{2} < x < \frac{l}{2}$. Deriving equation (2.28) three times yields

$$-\left(\frac{1}{e_c E_c}+\frac{1}{e_l E_l}+\frac{be_c(e_c+e_l)}{4I_c E_c}\right)\frac{d\tau(x)}{dx}+\sum_{k=0}^{\infty}\tau_k v_k'''(x)=0 \tag{2.29}$$

so that from equation (2.29), it is proved that neglecting the local contribution to the interface plane displacement leads one to prescribe $\frac{d\tau(x)}{dx}=0$. Consequently, the equilibrium of the membrane would be satisfied if and only if the shear stress field vanishes. This result underlines the fact that it is necessary to describe the mechanical fields close to the interface in a much more detailed manner than classical phenomenological methods (see for instance Ref. [346]).

3.1.3 Variational formulation and asymptotic analysis

The aim of this section is to provide a suitable formulation of the problem to be solved to get the shear-stress field representing the environmental effect on the cantilever.

The shear-stress field is found as the minimizer of the complementary energy of the overall structure. By assuming that there is no mechanical action on the membrane except the interaction with the beam, the set $\mathcal{V}$ of statically admissible shear-stress fields reads

$$\mathcal{V}=\left\{\phi\in L^2\left(\left[-\frac{l}{2},\frac{l}{2}\right]\right),\int_{-\frac{l}{2}}^{\frac{l}{2}}\phi(\zeta)d\zeta=0\right\} \tag{2.30}$$

Denoting by ξ the ratio between the thicknesses of the membrane and the beam

$$\xi=\frac{e_l}{e_c} \tag{2.31}$$

one defines the family of initial problems P_ξ as finding the shear-stress field $\tau_s(x)$ minimizing the complementary energy I_ξ

$$P_\xi:\left\{\begin{array}{ll}\tau_s(x)\in\mathcal{V}\\ I_\xi(\tau_s)\leq I_\xi(\phi) & \forall\phi\in\mathcal{V}\end{array}\right. \tag{2.32}$$

with

$$I_\xi(\phi)=\Delta\Theta_c(\phi)+\Delta\Theta_{l,\xi}(\phi) \tag{2.33}$$

where $\Delta\Theta_c(\phi)$ and $\Delta\Theta_{l,\xi}(\phi)$ are the complementary energies for the cantilever and membrane, respectively, given by

$$\begin{aligned}\Delta\Theta_c(\phi) &= \frac{1}{2}\int_{\Omega_c}\sigma_{1,xx}(\phi)\varepsilon_{1,xx}(\phi)dV\\ &\quad-\int_\Gamma\phi(\zeta)\left(u_l(\zeta,z)-u_l\left(-\frac{l}{2},z\right)\right)dS+E_{d\tau}(\phi)\end{aligned} \tag{2.34}$$

$$\begin{aligned}\Delta\Theta_{l,\xi}(\phi) &= \frac{1}{2}\int_{\Omega_{l,\xi}}\sigma_{l,xx}(\phi)\varepsilon_{l,xx}(\phi)dV\\ &\quad-\int_\Gamma\phi(\zeta)\left(u_c(\zeta,z)-u_c\left(-\frac{l}{2},z\right)\right)dS\end{aligned} \tag{2.35}$$

where $\varepsilon_{i,xx}$ is the linearized xx strain component in phase i ($i = l$ or $i = c$) and $E_{d\tau}(\phi)$ the strain energy in the localized deformation mode. It should be underlined that $I_\xi(\phi)$ (through the $\Delta\Theta_{l,\xi}$ term) is defined over a domain that depends on ξ. $I_\xi(\phi)$ is rewritten as

$$I_\xi(\phi) = a_\xi(\phi,\phi) - L(\phi) \tag{2.36}$$

where the quadratic (resp. linear) forms a_ξ and L read

$$\begin{aligned} a_\xi(\phi,\phi) &= \left(\xi^{-1}\frac{1}{2E_l be_c} + \frac{1}{2E_c be_c} + \frac{2}{E_c be_c}\right)\int_{-\frac{l}{2}}^{\frac{l}{2}} N_c^2(\phi)dx \\ &\quad + \left(\xi^{-1}\frac{1}{e_c E_l} + \frac{1}{e_c E_c} + \frac{be_c^2(1+\xi)}{E_c I_c}\right)\int_{-\frac{l}{2}}^{\frac{l}{2}} \phi \int_{-\frac{l}{2}}^{x} N_c(\phi)d\zeta dx \\ &\quad + 3E_{d\tau}(\phi) \end{aligned} \tag{2.37}$$

$$L(\phi) = b(\varepsilon_{L2} - \varepsilon_{L1})\int_{-\frac{l}{2}}^{\frac{l}{2}} \phi\left(x + \frac{l}{2}\right)dx \tag{2.38}$$

The coercivity condition on the quadratic form a_ξ is lost when $\xi \to 0$. Consequently,

- from a practical point of view, the initial problem cannot be accurately solved by standard (*i.e.,* 3D) finite element formulations;
- from a theoretical point of view, formulation (2.32) falls out of the framework of the Lax-Milgram theorem, meaning that existence and uniqueness of its solution cannot be directly ensured.

Formulation (2.32) thus needs to be modified to get a reliable solution for the shear-stress field. To transform P_ξ into a new problem defined on a fixed domain [402, 403] (*i.e.,* independent of ξ), one maps the domain

$$\Omega_{l,\xi} = \{\mathbf{x}_\Gamma + \xi y\mathbf{y}, y \in [0, e_c], \mathbf{x}_\Gamma \in \Gamma\} \tag{2.39}$$

onto

$$\Omega_l = \{\mathbf{x}_\Gamma + \tilde{y}\mathbf{y}, \tilde{y} \in [0, e_c], \mathbf{x}_\Gamma \in \Gamma\} \tag{2.40}$$

The displacement fields in both phases, as well as the interfacial shear-stress field remain unscaled. It is then straightforward to check that if τ_s is a solution for (2.32), then $\tau_{s,\xi}$ is a solution to problem $\widehat{P}$

$$\widehat{P}: \begin{cases} \tau_{s,\xi}(x) \in \mathcal{V} \\ \widehat{I_\xi}(\tau_{s,\xi}) \leq \widehat{I_\xi}(\phi) \qquad \forall \phi \in \mathcal{V} \end{cases} \tag{2.41}$$

where $\widehat{I_\xi}$ reads

$$\widehat{I_\xi}(\phi) = \widehat{a_\xi}(\phi,\phi) - L(\phi) \tag{2.42}$$

with the new quadratic form

$$\begin{aligned}\widehat{a_\xi}(\phi,\phi) &= \left(\xi\frac{1}{E_l be_c}+\frac{1}{E_c be_c}+\frac{4e_c^2}{E_c I_c}\right)\frac{1}{2}a_N(\phi,\phi)\\ &\quad+\left(\frac{\xi^{-1}}{e_c E_l}+\frac{1}{e_c E_c}+\frac{(1+\xi)be_c^2}{E_c I_c}\right)\frac{1}{2}a_d(\phi,\phi)+\frac{3b}{2}\times\frac{1}{2}a_\tau(\phi,\phi)\end{aligned} \quad (2.43)$$

where

$$a_N(\tau,\phi) = \int_{-\frac{l}{2}}^{\frac{l}{2}} N_c(\tau)N_c(\phi)dx \quad (2.44)$$

$$\frac{1}{2}a_d(\tau,\phi) = \frac{1}{2}\left\{\int_{-\frac{l}{2}}^{\frac{l}{2}}\tau\int_{-\frac{l}{2}}^{x}N_c(\phi)d\zeta dx+\int_{-\frac{l}{2}}^{\frac{l}{2}}\phi\int_{-\frac{l}{2}}^{x}N_c(\tau)d\zeta dx\right\} \quad (2.45)$$

$$\frac{1}{2}a_\tau(\tau,\phi) = \frac{1}{2}\left\{\int_{-\frac{l}{2}}^{\frac{l}{2}}\phi(x)v(\tau)(x)dx+\int_{-\frac{l}{2}}^{\frac{l}{2}}\tau(x)v(\phi)(x)dx\right\} \quad (2.46)$$

According to equation (2.19) it is assumed that the product ξE_l tends to a finite value K_l when ξ tends to 0

$$E_l = K_l\xi^{-1} \quad (2.47)$$

so that this new quadratic form $\widehat{a_\xi}$ satisfies the Lax-Milgram conditions, and solving problem $\widehat{P}$ consists of finding the solution $\tau_{s,\xi}(x)\in\mathcal{V}$ for the linear system

$$\begin{aligned}&\left(\xi^2\frac{1}{K_l be_c}+\frac{1}{E_c be_c}+\frac{4e_c^2}{E_c I_c}\right)a_N(\tau_{s,\xi},\phi)+\left(\frac{1}{e_c K_l}+\frac{1}{e_c E_c}+\frac{(1+\xi)be_c^2}{E_c I_c}\right)a_d(\tau_{s,\xi},\phi)\\ &\qquad+\frac{3b}{2}a_\tau(\tau_{s,\xi},\phi)-L(\phi)=0 \qquad \forall\phi\in\mathcal{V}\end{aligned} \quad (2.48)$$

The solution $\tau_{s,\xi}$ is then sought as a formal asymptotic expansion [401]

$$\tau_{s,\xi} = {}^0\tau+\xi\times{}^1\tau+\xi^2\times{}^2\tau+\ldots \quad (2.49)$$

Putting equation (2.49) into the stationarity conditions (2.48) leads to a separate linear system for each ξ order. The leading term ${}^0\tau\in\mathcal{V}$ is found to satisfy

$$a_0({}^0\tau,\phi)-L(\phi)=0 \qquad \forall\phi\in\mathcal{V} \quad (2.50)$$

with

$$\begin{aligned}a_0(\tau,\phi) &= \left(\frac{1}{E_c be_c}+\frac{4e_c^2}{E_c I_c}\right)a_N(\tau,\phi)\\ &\quad+\left(\frac{1}{e_c K_l}+\frac{1}{e_c E_c}+\frac{be_c^2}{E_c I_c}\right)a_d(\tau,\phi)+\frac{3b}{2}a_\tau(\tau,\phi)\end{aligned} \quad (2.51)$$

A finite dimension space $\mathcal{V}$ has to be chosen (described by the orthogonal basis of Legendre polynomials $P_n, n \in \{1,\dots N\}$ in Ref.[400]) so that,

$$^0\tau(x) = \sum_{k=1}^{N} {}^0\tau_k P_k\left(\frac{2x}{l}\right) \tag{2.52}$$

System (2.50) then yields a square linear system, which is solved to provide the shear-stress field $^0\tau(x)$ along the interface Γ as its expansion (2.52) (see [400]). The surface coupling is thus described by the mechanical parameters of the TEL: K_l and ε_{L2}.

3.1.4 Identification

These two parameters can be experimentally estimated using the multiple wavelength reflection microscope described in Sect. 2.2, which provides a wavelength-dependent reflectivity field $R_{wd}(x)$ (related to the chemical surface modification) and a wavelength-independent reflectivity field $R_{wi}(x)$, which is related to the surface rotation $\frac{dw}{dx}$ where $w(x)$ denotes the out-of-plane cantilever displacement field and x is the cantilever beam axis (the beam corresponds to $-\frac{l}{2} \leq x \leq \frac{l}{2}$). Assuming that $\varepsilon_{L1} = 0$ and that the TEL eigenstrain is related to the wavelength-dependent reflectivity change field through

$$\varepsilon_l(x) = \varepsilon_{L2} = F R_{wd}(x) \tag{2.53}$$

the in-plane displacement of the lower side of the TEL may be easily calculated. The in-plane displacement of the upper side of the cantilever is derived from the out-of-plane displacement $w(x)$, so that the displacement continuity at the interface reads, at equilibrium

$$\begin{aligned} -\frac{t_c}{2}\int_{-\frac{l}{2}}^{x} \frac{d^2w}{dx^2} d\eta \;\; = \\ F\int_{-\frac{l}{2}}^{x} R_{wd}(\eta) d\eta + \frac{t_c}{6}\left(1+\frac{E_c}{K_l}\right)\int_{-\frac{l}{2}}^{x}\int_{-\frac{l}{2}}^{\eta} \frac{d^3w}{dx^3} d\tau d\eta \end{aligned}$$

for any x (pixels) along the beam. E_c denotes the cantilever Young's modulus. Assuming the cantilever is in equilibrium, the continuity condition is recast as

$$\begin{aligned} F\int_{-\frac{l}{2}}^{x} R_{wd}(\eta) d\eta + \frac{t_c}{6}\left(4+\frac{E_c}{K_l}\right)\left(\frac{dw}{dx}(x) - \frac{dw}{dx}\left(-\frac{l}{2}\right)\right) \\ -\left(\frac{t_c}{6}\left(4+\frac{E_c}{K_l}\right) - \frac{t_c}{2}\right)\left(x+\frac{l}{2}\right)\frac{d^2w}{dx^2}\left(-\frac{l}{2}\right) = 0 \end{aligned} \tag{2.54}$$

It should be highlighted that Eq.(2.54) can be written for any position x along the beam. Dealing with full-field data, Eq.(2.54) is written for any pixel along the cantilever beam, thus providing an over-determined linear system, whose main unknowns are the strain-reflectivity coefficient F and the characteristic length $\frac{t_c}{6}\left(4+\frac{E_c}{K_l}\right)$. The other terms ($R_{wd}$,

$\frac{dw}{dx}$) are obtained from the measured fields. It should be highlighted that the curvature at the base $\frac{d^2w}{dx^2}\left(-\frac{l}{2}\right)$ is rather difficult to measure since it requires a fairly rich kinematic description. Instead of solving Eqs.(2.54) in a least-squares sense to get access to the TEL stiffness parameter K_l, it is proposed to filter Eq.(2.54) by making use of an orthonormal polynomial basis $\{P_n(x)\}$. $P_n(x)$ is of order n and satisfies

$$\int_{-\frac{l}{2}}^{\frac{l}{2}} P_n(x)P_m(x)dx = \delta_{mn} \tag{2.55}$$

where δ_{mn} stands for the Kronecker symbol. Let us denote

$$J(x) = F\int_{-\frac{l}{2}}^{x} R_{wd}(\eta)d\eta + \frac{t_c}{6}\left(4+\frac{E_c}{K_l}\right)\left(\frac{dw}{dx}(x) - \frac{dw}{dx}\left(-\frac{l}{2}\right)\right) \tag{2.56}$$

$$a_0 = \int_{-\frac{l}{2}}^{\frac{l}{2}} J(x)P_0(x)dx \tag{2.57}$$

$$a_1 = \int_{-\frac{l}{2}}^{\frac{l}{2}} J(x)P_1(x)dx \tag{2.58}$$

Filtering out the 0 and 1 order terms in Eq.(2.54) yields

$$J(x) - a_0P_0(x) - a_1P_1(x) = 0 \tag{2.59}$$

for any x along the beam, so that the poorly measured term vanishes. The left-hand side of Eq.2.59 is linear with respect to F and $\frac{t_c}{6}\left(4+\frac{E_c}{K_l}\right)$ so that gathering all the equations obtained for all the pixels yields an over-determined linear system featuring one equation per pixel for only 2 unknowns. As one is looking for a non-trivial solution, the resulting system is solved using a singular value decomposition to provide an estimate for the ratio

$$r_a = \frac{F}{\frac{t_c}{6}\left(4+\frac{E_c}{K_l}\right)} \tag{2.60}$$

The associated singular value should vanish, thus providing a quality estimator for the solution. It should be highlighted that the situation with a homogeneous R_{wd} would make r_a disappear from the projected equation.

The above-described procedure is applied to reflectivity fields obtained using gold-coated silicon-nitride cantilevers ($80\times15\times0.75\mu$m) placed in a 3-electrodes arrangement with a KCl (5×10^{-3}M) electrolyte. The gold layer is used as the working electrode. Every cantilever is electrically addressed independently, and its potential is swept in the double-layer regime ($0.04\text{V}\leq V\leq 0.4\text{V}$ vs Ag/AgCl) at 4mV/s after an electrochemical cleaning. 160 images are recorded for each wavelength during three potential cycles, and the obtained reflectivity change fields are presented in FIG.2.11. The cantilever base is at the top of the figure, and the cantilever tip is at the bottom. The wavelength-dependent field R_{wd} is averaged across the cantilever width and is displayed in FIG.2.11a. The R_{wd}

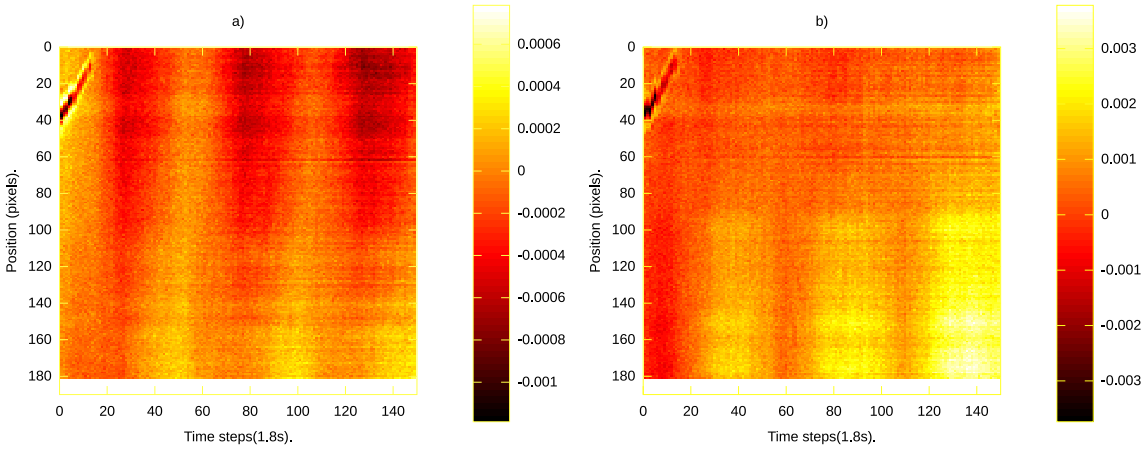

Figure 2.11: Measured reflectivity changes measured when sweeping the potential: a) wavelength-dependent (red) reflectivity change, b) wavelength-independent reflectivity change.

field, which is assumed to translate the local chemical activity, is heterogeneous, thus highlighting the need for full-field measurements. The R_{wi} field, which is assumed to represent the mechanical surface rotation, is plotted after width-averaging in FIG.2.11b and denotes an upward (gold-side) bending of the cantilever when the potential is increased. A slight strain accumulation can be noticed during the 3 potential cycles. The sensitivity field is obtained from a calibration procedure to translate the R_{wi} field into a rotation field $\frac{dw}{dx}$. The R_{wd} and rotation fields are then used to identify the r_a ratio, using the identification procedure detailed above for each time step, independently. The identified r_a ratio is displayed in FIG.2.12. This ratio is found to be independent of the time step and is equal to $r_a \simeq -7 \times 10^{-6} \mu\text{m}^{-1}$. The larger deviations from this value occur for the first steps, where a bubble travels near the cantilever base, as seen in FIG.2.11, and at the time steps the sweeping direction changes, leading to sharp changes in the cantilever electrical state so that the equilibrium condition can no longer be ensured. This tends to indicate that a single reaction occurs at the cantilever surface, and that the chosen modeling is adequate to describe the involved effects.

Considering that full-field set-ups are now available to investigate chemo-mechanical couplings at the micrometer scale, a modeling based on an asymptotic analysis (and thus resembling the Gurtin-Murdoch theory) as well as a suited identification procedure have been proposed to describe chemo-mechanical couplings. It is demonstrated that parameters (thermodynamically) describing the reaction occurring on a micro-cantilever surface may be retrieved using fields obtained from the multiple-wavelength reflection microscope described in Sect. 2.2. This first attempt also clearly shows that the traditional cantilever geometry with a homogeneous reaction is not the most adequate to yield reliable parameters, thus highlighting the need to deal with heterogeneous chemical modifications.

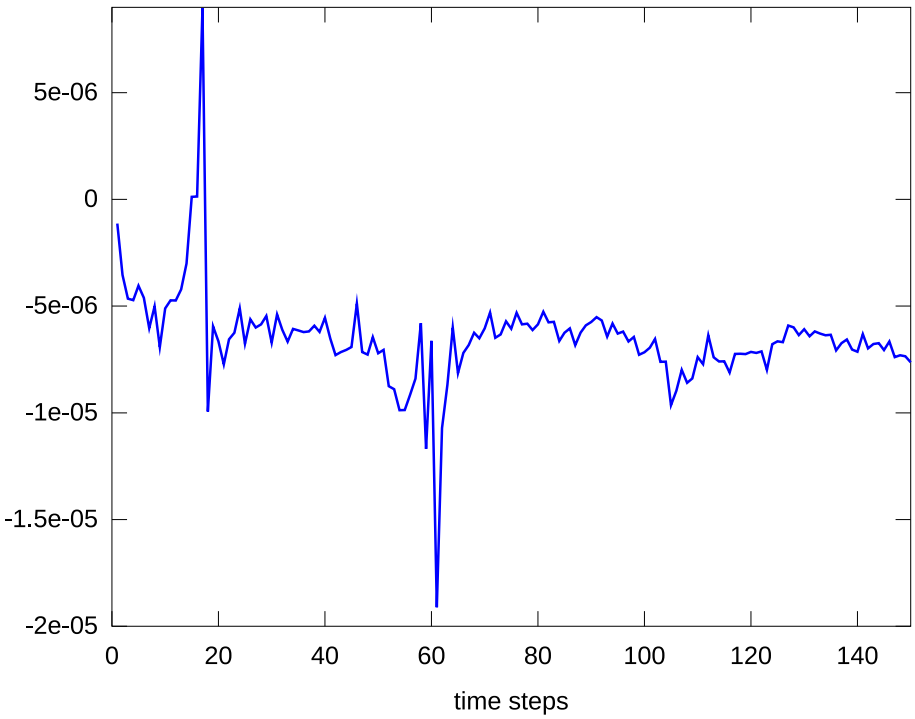

Figure 2.12: Identified ratio r_a along the experiment.

3.2 Second strain-gradient elasticity

Besides Gurtin-Murdoch-like theories that explicitly consider the chemical effects as extrinsic, it has been shown in Sect.1.2 that higher-order elasticity may also provide an interesting framework. The second-strain gradient theory proposed by Mindlin [389] has actually been shown to possibly render both size-dependent elasticity and the equivalent of surface tension for solids as intrinsic material parameters.

This section derives an Euler-Bernoulli beam theory for isotropic elastic materials based on a second strain gradient description [405]. As such a description has been proved to allow for the definition of surface tension for solids, the equations satisfied by a beam featuring a through-thickness cohesion modulus gradient are established in order to describe the behavior of micro-cantilever sensors. Closed-form solutions are given for chemical loadings. It is then shown that the involved material parameters may be identified from full-field measurements and that the shape of the displacement field resulting from a chemical loading depends on the cantilever thickness as well as on the material parameters. This makes such a theory potentially able to explain some of the experimental results found in the literature.

A linear theory of deformation of elastic beams in which the strain-energy density is a function of strain and its first and second gradients is adopted, and this section is intended to derive a tractable beam theory based on such a higher order material description. This

contribution may therefore be seen as an extension of the recent propositions to describe the behavior of tiny Euler-Bernoulli [363, 364, 365, 366, 367] or Timoshenko [368, 369, 370] beams. The basic assumptions regarding the beam behavior are first presented. The virtual work principle [362] is then applied to yield the differential equations governing the mechanical behavior of chemically-modified isotropic beams. These equations are solved for cases of interest and an identification procedure based on the data provided by the multiple-wavelength microscope described in Sect. 2.2 is proposed.

3.2.1 Basic assumptions

Considering a beam lying along the **x** direction and using the Euler-Bernoulli assumption, the displacement **d** for a loading in the $(\mathbf{x},\mathbf{y})$ plane reads

$$d_x = u(x) - y\frac{\mathrm{d}v(x)}{\mathrm{d}x} \quad ; \quad d_y = v(x)$$

Following Mindlin [389], the free energy density is assumed to depend on the classical infinitesimal strain ε^1, as well as on the triadic $\varepsilon^2 = \nabla\nabla\mathbf{d}$ (symmetric in the first two positions) and on $\varepsilon^3 = \nabla\nabla\nabla\mathbf{d}$ (symmetric in the first three positions). ε^1 has therefore a single non-vanishing component

$$\varepsilon_{xx} = -y\frac{\mathrm{d}^2v}{\mathrm{d}x^2} + \frac{\mathrm{d}u}{\mathrm{d}x}$$

The non-zero components of ε^2 read

$$\varepsilon_{xxx} = -y\frac{\mathrm{d}^3v}{\mathrm{d}x^3} + \frac{\mathrm{d}^2u}{\mathrm{d}x^2} \quad ; \quad \varepsilon_{xxy} = \frac{\mathrm{d}^2v}{\mathrm{d}x^2} = -\varepsilon_{xyx} = -\varepsilon_{yxx}$$

The components of ε^3 read

$$\varepsilon_{xxxx} = -y\frac{\mathrm{d}^4v}{\mathrm{d}x^4} + \frac{\mathrm{d}^3u}{\mathrm{d}x^3} \quad ; \quad \varepsilon_{xxxy} = \frac{\mathrm{d}^3v}{\mathrm{d}x^3} = -\varepsilon_{yxxx} = -\varepsilon_{xyxx} = -\varepsilon_{xxyx}$$

The elastic behavior is assumed to be isotropic and is modeled according to the constitutive law derived by Mindlin [389]. The elastic behavior is thus described by five coefficients a_n (found in Toupin's theory describing surface effects for non-centrosymmetric materials [388]), a cohesion modulus b_0, seven coefficients b_n and three coefficients c_n in addition to Lamé's coefficients λ and μ. The ratios a_n/μ, b_0/μ and c_n/μ scale as a squared length, and the other b_n/μ as a length raised to the fourth power.

3.2.2 Virtual work principle for a beam featuring a through-thickness modulus of cohesion gradient

Mindlin demonstrated that the cohesion modulus b_0 contributes to the free energy density through a term $b_0\varepsilon_{iijj}$ which is then linear with respect to the kinematic variables. It thus

defines a surface energy (without any external loading), so that one will assume in the following that all the material parameters are uniform in the cantilever beam, except the cohesion modulus b_0 which is considered to possibly depend on y in order to describe the chemical modification of one cantilever side compared to the other. Considering a virtual displacement field $\mathbf{d}^\star$, the virtual change in the potential energy density $W(\mathbf{d}^\star)$ reads [362]

$$\begin{aligned} W(\mathbf{d}^\star) &= \tau_{xx}\varepsilon^\star_{xx} + \tau_{xxx}\varepsilon^\star_{xxx} + 2\tau_{yxx}\varepsilon^\star_{yxx} + \tau_{xxy}\varepsilon^\star_{xxy} + \tau_{xxxx}\varepsilon^\star_{xxxx} \\ &\quad + 3\tau_{yxxx}\varepsilon^\star_{yxxx} + \tau_{xxxy}\varepsilon^\star_{xxxy} \end{aligned}$$

with

$$\begin{aligned} \tau_{xx} &= (\lambda+2\mu)\,\varepsilon_{xx} + (c_1+c_2+c_3)\,\varepsilon_{xxxx} \\ \tau_{xxx} &= 2\,(a_1+a_2+a_3+a_4+a_5)\,\varepsilon_{xxx} \\ \tau_{yxx} &= (a_1+2a_4+a_5)\,\varepsilon_{yxx} + \left(\frac{a_2}{2}+a_5\right)\varepsilon_{xxy} \\ \tau_{xxy} &= (a_2+2a_5)\,\varepsilon_{yxx} + 2\,(a_3+a_4)\,\varepsilon_{xxy} \\ \tau_{xxxx} &= 2\,(b_1+b_2+b_3+b_4+b_5+b_6+b_7)\,\varepsilon_{xxxx} \\ &\quad + \frac{b_3}{2}\,(\varepsilon_{xxyx}+\varepsilon_{xxxy}) + (c_1+c_2+c_3)\,\varepsilon_{xx} + b_0(y) \\ \tau_{yxxx} &= \frac{2}{3}\,(2b_2+b_3+b_5+3b_6+2b_7)\,\varepsilon_{yxxx} + \frac{1}{3}\,(b_3+2b_4+2b_7)\,\varepsilon_{xxxy} \\ \tau_{xxxy} &= (b_3+2b_4+2b_7)\,\varepsilon_{yxxx} + 2\,(b_5+b_6)\,\varepsilon_{xxxy} \end{aligned}$$

Making use of the following substitutions

$$A = a_1+a_2+a_3+a_4+a_5 = (\lambda+2\mu)\,l_A^2 \geq 0 \tag{2.61}$$

$$B = b_1+b_2+b_3+b_4+b_5+b_6+b_7 = (\lambda+2\mu)\,l_B^4 \geq 0 \tag{2.62}$$

$$C = c_1+c_2+c_3 = (\lambda+2\mu)\,l_C^2 \geq 0 \tag{2.63}$$

$$\tilde{A} = a_1-a_2+a_3+3a_4-a_5 = (\lambda+2\mu)\,l_{\tilde{A}}^2 \tag{2.64}$$

$$\tilde{B} = b_2-b_4+b_5+2b_6 = (\lambda+2\mu)\,l_{\tilde{B}}^4 \tag{2.65}$$

and integrating $W(\mathbf{d}^\star)$ over a cross-section defined by $-\frac{t}{2} \leq y \leq \frac{t}{2}$ and $-\frac{h}{2} \leq z \leq \frac{h}{2}$ and integrating the result by parts yields

$$
\begin{aligned}
h^{-1}t^{-1}\int_0^L \int_{-\frac{h}{2}}^{\frac{h}{2}} \int_{-\frac{t}{2}}^{\frac{t}{2}} W(\mathbf{d}^\star)\mathrm{d}y\mathrm{d}z\mathrm{d}x \quad = \\
-\int_0^L \left(2B\frac{\mathrm{d}^6u}{\mathrm{d}x^6} + 2\left(C-A\right)\frac{\mathrm{d}^4u}{\mathrm{d}x^4} + \left(\lambda+2\mu\right)\frac{\mathrm{d}^2u}{\mathrm{d}x^2}\right)u^\star(x)\mathrm{d}x \\
+\left[u^\star(x)\left(2B\frac{\mathrm{d}^5u}{\mathrm{d}x^5} + 2\left(C-A\right)\frac{\mathrm{d}^3u}{\mathrm{d}x^3} + \left(\lambda+2\mu\right)\frac{\mathrm{d}u}{\mathrm{d}x}\right)\right]_0^L \\
-\left[\frac{\mathrm{d}u^\star(x)}{\mathrm{d}x}\left(2B\frac{\mathrm{d}^4u}{\mathrm{d}x^4} + \left(C-2A\right)\frac{\mathrm{d}^2u}{\mathrm{d}x^2}\right)\right]_0^L \\
+\left[\frac{\mathrm{d}^2u^\star(x)}{\mathrm{d}x^2}\left(2B\frac{\mathrm{d}^3u}{\mathrm{d}x^3} + C\frac{\mathrm{d}u}{\mathrm{d}x} + t\bar{b_0}\right)\right]_0^L \\
+\int_0^L \left(\frac{Bt^2}{6}\frac{\mathrm{d}^8v}{\mathrm{d}x^8} + \left(t^2\frac{C-A}{6} - 4\tilde{B}\right)\frac{\mathrm{d}^6v}{\mathrm{d}x^6} + \left(2\tilde{A} + \left(\lambda+2\mu\right)\frac{t^2}{12}\right)\frac{\mathrm{d}^4v}{\mathrm{d}x^4}\right)v^\star(x)\mathrm{d}x \\
-\left[v^\star(x)\left(\frac{Bt^2}{6}\frac{\mathrm{d}^7v}{\mathrm{d}x^7} + \left(t^2\frac{C-A}{6} - 4\tilde{B}\right)\frac{\mathrm{d}^5v}{\mathrm{d}x^5} + \left(2\tilde{A} + \left(\lambda+2\mu\right)\frac{t^2}{12}\right)\frac{\mathrm{d}^3v}{\mathrm{d}x^3}\right)\right]_0^L \\
+\left[\frac{\mathrm{d}v^\star(x)}{\mathrm{d}x}\left(\frac{Bt^2}{6}\frac{\mathrm{d}^6v}{\mathrm{d}x^6} + \left(t^2\frac{C-A}{6} - 4\tilde{B}\right)\frac{\mathrm{d}^4v}{\mathrm{d}x^4} + \left(2\tilde{A} + \left(\lambda+2\mu\right)\frac{t^2}{12}\right)\frac{\mathrm{d}^2v}{\mathrm{d}x^2}\right)\right]_0^L \\
-\left[\frac{\mathrm{d}^2v^\star(x)}{\mathrm{d}x^2}\left(\frac{Bt^2}{6}\frac{\mathrm{d}^5v}{\mathrm{d}x^5} + \left(t^2\frac{C-2A}{12} - 4\tilde{B}\right)\frac{\mathrm{d}^3v}{\mathrm{d}x^3}\right)\right]_0^L \\
+t\left[\frac{\mathrm{d}^3v^\star(x)}{\mathrm{d}x^3}\left(\frac{Bt}{6}\frac{\mathrm{d}^4v}{\mathrm{d}x^4} + \frac{Ct}{12}\frac{\mathrm{d}^2v}{\mathrm{d}x^2} - \acute{b_0}\right)\right]_0^L
\end{aligned}
\tag{2.66}
$$

where the through-thickness b_0 distribution appears through its projections:

$$\int_{-\frac{t}{2}}^{\frac{t}{2}} b_0(y)\mathrm{d}y = t\bar{b_0} \quad ; \quad \int_{-\frac{t}{2}}^{\frac{t}{2}} b_0(y)y\mathrm{d}y = t^2\acute{b_0}$$

The chosen description calls for two remarks:

- Looking at Eq.(2.66) it should be highlighted that the chosen parametrization yields decoupled bending and tension problems. It should however be kept in mind that most of the cantilever sensor applications reported in the literature keep one side of the cantilever unmodified, so that these situations should be described by a change in both $\bar{b_0}$ and $\acute{b_0}$. As cantilever sensors are commonly based on the detection of the out-of-plane displacement, the tension problem will be discarded in the following.

- The chosen kinematic does not allow for the Poisson effect to develop. As a consequence, the Lamé's coefficients appear only through the combination

$$\lambda + 2\mu = E\frac{1}{1-\frac{2\nu^2}{1-\nu}}$$

where E and ν stand for Young's modulus and Poisson's ratio, respectively. In order to approach the Poisson effect without mixing kinematic and static assumptions (as for classical beam theories), it is proposed for the sake of simplicity to replace the combination $\lambda + 2\mu$ by the Young's modulus E everywhere in the following, the identity being obtained for $\nu = 0$ [368]. Mixing kinematic and static assumptions makes here the resulting description useless, especially if one wishes to get closed-form solutions. Any enrichment should therefore be motivated by experimental results.

3.2.3 Solutions for the bending problem of a cantilever beam

General solution For a cantilever beam clamped at $x = 0$, Eq. (2.66) (restricted to the tension part) should be satisfied for any test field $v^\star$ [362] so that

$$v^\star(x) \in \mathcal{V}_{ad}\ ,\ \mathcal{V}_{ad} = \left\{ v(x) \in H^1\left([0,L]\right) \backslash v(0) = 0, \frac{\mathrm{d}v}{\mathrm{d}x}(0) = 0 \right\}$$

The displacement field should therefore satisfy $\forall x \in [0,L]$

$$\frac{Bt^2}{6}\frac{\mathrm{d}^8 v}{\mathrm{d}x^8} + \left(t^2\frac{C-A}{6} - 4\tilde{B} \right)\frac{\mathrm{d}^6 v}{\mathrm{d}x^6} + \left(2\tilde{A} + E\frac{t^2}{12} \right)\frac{\mathrm{d}^4 v}{\mathrm{d}x^4} = 0 \tag{2.67}$$

Looking for solutions of the form

$$v(x) = \exp\left(\Gamma \frac{x}{l_B} \right)$$

and making use of the characteristic lengths defined by Eqs.(2.61-2.65) and setting $\tau = \frac{t^2}{6l_B^2}$ the characteristic polynomial in Γ obtained from Eq.(2.67) reads

$$l_B^2 \tau \Gamma^4 + \left(\tau\left(l_C^2 - l_A^2 \right) - 4\frac{l_{\tilde{B}}^4}{l_B^2} \right)\Gamma^2 + 2l_{\tilde{A}}^2 + \frac{\tau l_B^2}{2} = 0 \tag{2.68}$$

The general solution for Eq. (2.67) therefore reads

$$v(x) = \sum_{i=0}^{3} q_i \left(\frac{x}{L} \right)^i + \sum_{j=1}^{4} \gamma_j \exp\left(\Gamma_j \frac{x}{l_B} \right) = \sum_{i=0}^{3} q_i \left(\frac{x}{L} \right)^i + z(x) \tag{2.69}$$

where the four unknowns Γ_j are the solutions of Eq. (2.68). The coefficients are to be obtained from the boundary conditions (obtained from the known displacements and Eq. (2.66)). The nature (real or complex) of the solutions Γ_j is dictated by the sign of

$$\Delta = \left(\left(l_C^2 - l_A^2 \right)^2 - 2l_B^4 \right)\tau^2 - 8\left(l_{\tilde{B}}^4 l_B^{-2}\left(l_C^2 - l_A^2 \right) - l_{\tilde{A}}^2 l_B^2 \right)\tau + \frac{16 l_{\tilde{B}}^8}{l_B^4}$$

and thus depends on the cantilever thickness. It should be highlighted that whatever the material parameters, $\lim_{\tau\to 0}\Delta = \frac{16 l_{\tilde{B}}^8}{l_B^4} > 0$, so that the zero-thickness limit always corresponds to real solutions for Γ^2. The sign of Δ for a non-vanishing thickness is discussed in Sect. 3.2.4. One should keep in mind that for a given material, the shape of the general solution may therefore depend on the cantilever thickness.

Pure chemical loading Let us now consider a cantilever beam (clamped at $x=0$) under the action of a heterogeneous chemical surface modification. Eq. (2.66) yields at $x=L$

$$\begin{aligned}
\frac{l_B^4 t^2}{6}\frac{\mathrm{d}^7 v}{\mathrm{d}x^7} + \left(t^2\frac{l_C^2 - l_A^2}{6} - 4l_{\tilde{B}}^4\right)\frac{\mathrm{d}^5 v}{\mathrm{d}x^5} + \left(2l_{\tilde{A}}^2 + \frac{t^2}{12}\right)\frac{\mathrm{d}^3 v}{\mathrm{d}x^3} &= 0\\
\frac{l_B^4 t^2}{6}\frac{\mathrm{d}^6 v}{\mathrm{d}x^6} + \left(t^2\frac{l_C^2 - l_A^2}{6} - 4l_{\tilde{B}}^4\right)\frac{\mathrm{d}^4 v}{\mathrm{d}x^4} + \left(2l_{\tilde{A}}^2 + \frac{t^2}{12}\right)\frac{\mathrm{d}^2 v}{\mathrm{d}x^2} &= 0\\
\frac{l_B^4 t^2}{6}\frac{\mathrm{d}^5 v}{\mathrm{d}x^5} + \left(t^2\frac{l_C^2 - 2l_A^2}{12} - 4l_{\tilde{B}}^4\right)\frac{\mathrm{d}^3 v}{\mathrm{d}x^3} &= 0\\
\frac{l_B^4 t}{6}\frac{\mathrm{d}^4 v}{\mathrm{d}x^4} + t\frac{l_C^2}{12}\frac{\mathrm{d}^2 v}{\mathrm{d}x^2} &= \frac{\acute{b_0}}{E}
\end{aligned}$$

Using at $x=0$

$$\frac{l_B^4 t^2}{6}\frac{\mathrm{d}^5 v}{\mathrm{d}x^5} + \left(t^2\frac{l_C^2 - 2l_A^2}{12} - 4l_{\tilde{B}}^4\right)\frac{\mathrm{d}^3 v}{\mathrm{d}x^3} = 0 \quad ; \quad \frac{l_B^4 t}{6}\frac{\mathrm{d}^4 v}{\mathrm{d}x^4} + t\frac{l_C^2}{12}\frac{\mathrm{d}^2 v}{\mathrm{d}x^2} = \frac{\acute{b_0}}{E}$$

the displacement field reads

$$\begin{aligned}
v(x) &= q_0 + q_1\frac{x}{L} + \\
&\frac{\acute{b_0}\left(a_1\sinh\left(\frac{\Gamma_1 L}{2l_B}\right)\cosh\left(\Gamma_2\frac{2x-L}{2l_B}\right) - a_2\sinh\left(\frac{\Gamma_2 L}{2l_B}\right)\cosh\left(\Gamma_1\frac{2x-L}{2l_B}\right)\right)}{tE\left(a_1 b_2\sinh\left(\frac{\Gamma_1 L}{2l_B}\right)\cosh\left(\frac{\Gamma_2 L}{2l_B}\right) + a_2 b_1\sinh\left(\frac{\Gamma_2 L}{2l_B}\right)\cosh\left(\frac{\Gamma_1 L}{2l_B}\right)\right)}
\end{aligned} \tag{2.70}$$

where q_0 and q_1 result from the clamping condition at $x=0$ and where

$$a_i = \frac{l_B^4 t^2}{6}\left(\frac{\Gamma_i}{l_B}\right)^5 + \left(t^2\frac{l_C^2 - 2l_A^2}{12} - 4l_{\tilde{B}}^4\right)\left(\frac{\Gamma_i}{l_B}\right)^3 ; b_i = \frac{l_B^4}{6}\left(\frac{\Gamma_i}{l_B}\right)^4 + \frac{l_C^2}{12}\left(\frac{\Gamma_i}{l_B}\right)^2$$

The closed-form solution (2.70) for the out-of-plane displacement field induced by the chemical modification of one cantilever side calls for several comments:

- It should first be highlighted that this solution, in its generality, may significantly depart from the field resulting from Stoney's assumptions (uniform curvature). Besides the rigid-body motion, it may be decomposed into the sum of two hyperbolic cosines with length scales depending on the higher-order elasticity constants. As setting $b_n = c_n = 0$ yields a trivial solution ($q_i = 0$, $\gamma_i = 0$), it is confirmed that a

first strain gradient theory is not sufficient to describe surface effects for isotropic materials. This pleads for the use of Mindlin's description, similarly to the elastic fluid described in Ref. [406].

- These higher-order elasticity constants necessarily reflect the length scales characterizing the material under scrutiny, and are thus expected to strongly depend on grain size or degree of crystallinity, or more generally, on the processing conditions. The proposed framework therefore seems particularly suited to include the observed dependence on surface morphology [288].

- The role of the cantilever thickness is much more complicated than it could be anticipated from simple beam theories. Besides the t^{-1} scaling factor, the thickness drives the shape of the displacement field through the solutions of the characteristic polynomial (2.68), possibly switching the field from hyperbolic to oscillatory (for imaginary solutions). One could easily imagine that such a situation experimentally observed using the (single-point) optical lever technique could lead to some data misinterpretation or ambiguity.

- Besides the thickness, the solution (2.70) highlights the role of the ratio l_B/L , thus indicating that the cantilever length could act as a filtering parameter in order to control the amplitude of the component added to the displacement field.

3.2.4 Large thickness regime

As seen from Eq. (2.67), the solution for the chemically-induced bending problem is driven by the cantilever thickness so that the induced displacement field has an oscillatory component depending on the sign of Δ (see Eq. (2.70)). Defining the characteristic material lengths as

$$\lambda^4 = \left(l_C^2 - l_A^2\right)^2 - 2l_B^4 \tag{2.71}$$

$$\lambda_\Lambda^2 = l_C^2 - l_A^2 + l_{\tilde{A}}^2 \frac{l_B^4}{l_{\tilde{B}}^4} \tag{2.72}$$

and the threshold thickness

$$t_\pm^2 = 24 \frac{l_{\tilde{B}}^4}{\lambda_\Lambda^2} \tag{2.73}$$

the discussion of the sign of Δ is summarized by FIG.3.2.4.

It is worth noting that for a given characteristic material length, changing the cantilever thickness may be enough to switch between hyperbolic and oscillatory displacement fields, thus demonstrating the rather complex role of the cantilever thickness. The role of the cantilever thickness however simplifies when it becomes large enough to make the t^2 terms in Eq. (2.67) dominant. Discarding the terms arising from the tension problem and keeping the higher order terms in the bending problem, Eq. (2.66) may be rewritten for any chemical loading field and approximated by

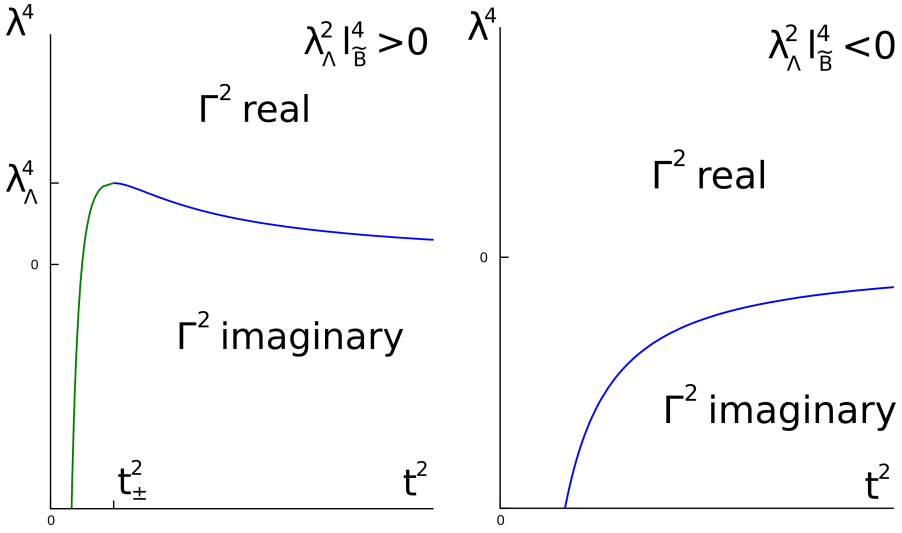

Figure 2.13: Sign of Δ as a function of the material parameters and of the cantilever thickness.

$$
\begin{aligned}
(Eh)^{-1}t^{-3}\int_0^L\int_{-\frac{h}{2}}^{\frac{h}{2}}\int_{-\frac{t}{2}}^{\frac{t}{2}} W(\mathbf{d}^\star)\mathrm{d}y\mathrm{d}z\mathrm{d}x \quad &\simeq \\
&+\int_0^L\left(\frac{l_B^4}{6}\frac{\mathrm{d}^8 v}{\mathrm{d}x^8}+\frac{l_C^2-l_A^2}{6}\frac{\mathrm{d}^6 v}{\mathrm{d}x^6}+\frac{1}{12}\frac{\mathrm{d}^4 v}{\mathrm{d}x^4}-\frac{\mathrm{d}^4}{\mathrm{d}x^4}\left(\frac{b_0^{'}}{Et}\right)\right)v^\star(x)\mathrm{d}x \\
&+\left[v^\star(x)\left(-\frac{l_B^4}{6}\frac{\mathrm{d}^7 v}{\mathrm{d}x^7}-\frac{l_C^2-l_A^2}{6}\frac{\mathrm{d}^5 v}{\mathrm{d}x^5}-\frac{1}{12}\frac{\mathrm{d}^3 v}{\mathrm{d}x^3}+\frac{\mathrm{d}^3}{\mathrm{d}x^3}\left(\frac{b_0^{'}}{Et}\right)\right)\right]_0^L \\
&+\left[\frac{\mathrm{d}v^\star(x)}{\mathrm{d}x}\left(\frac{l_B^4}{6}\frac{\mathrm{d}^6 v}{\mathrm{d}x^6}+\frac{l_C^2-l_A^2}{6}\frac{\mathrm{d}^4 v}{\mathrm{d}x^4}+\frac{1}{12}\frac{\mathrm{d}^2 v}{\mathrm{d}x^2}-\frac{\mathrm{d}^2}{\mathrm{d}x^2}\left(\frac{b_0^{'}}{Et}\right)\right)\right]_0^L \\
&+\left[\frac{\mathrm{d}^2 v^\star(x)}{\mathrm{d}x^2}\left(-\frac{l_B^4}{6}\frac{\mathrm{d}^5 v}{\mathrm{d}x^5}-\frac{l_C^2-2l_A^2}{12}\frac{\mathrm{d}^3 v}{\mathrm{d}x^3}+\frac{\mathrm{d}}{\mathrm{d}x}\left(\frac{b_0^{'}}{Et}\right)\right)\right]_0^L \\
&+\left[\frac{\mathrm{d}^3 v^\star(x)}{\mathrm{d}x^3}\left(\frac{l_B^4}{6}\frac{\mathrm{d}^4 v}{\mathrm{d}x^4}+\frac{l_C^2}{12}\frac{\mathrm{d}^2 v}{\mathrm{d}x^2}-\frac{b_0^{'}}{Et}\right)\right]_0^L
\end{aligned}
\tag{2.74}
$$

The displacement may then be obtained (under the large thickness assumption) by applying the procedure detailed in Sect. 3.2.3 and 3.2.3 starting from the approximate virtual work Eq. (2.74). It is worth noting that under this assumption, the displacement field is fully determined by l_A^2,l_B^4 and l_C^2, definitely making the number of driving parameters reasonably low.

FIG.2.14 displays the displacement and rotation fields computed using $l_A^2 = 10^{-3}$, $l_B^4 =$

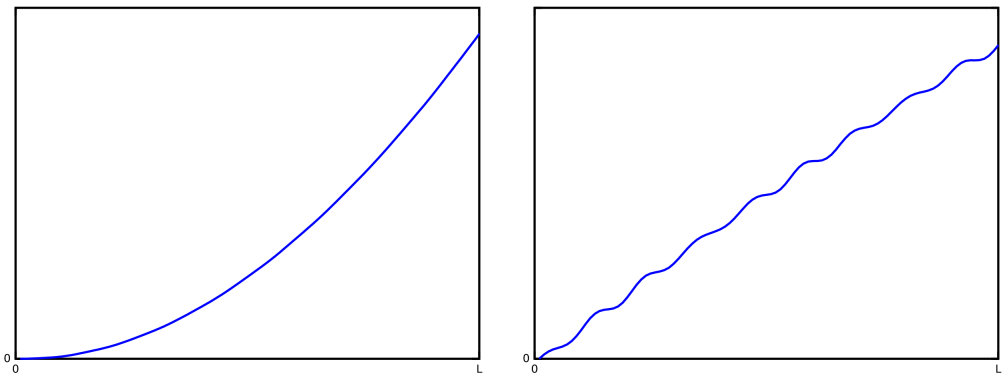

Figure 2.14: Displacement (left) and rotation (right) fields obtained using $l_A^2 = 10^{-3}$, $l_B^4 = 10^{-6}$, $l_C^2 = 3 \times 10^{-3}$, $L = 2$ and a uniform chemical loading.

10^{-6}, $l_C^2 = 3 \times 10^{-3}$, $L = 2$ and assuming a uniform chemical loading. If the displacement field seems mainly polynomial, the rotation field shows this polynomial contribution is "decorated" with an oscillating term with a rather short wavelength. This example thus illustrates that an identification procedure targeting the material parameters involved in the large thickness regime should probably rely on measured rotation fields instead of displacement fields.

3.2.5 Identification

This section thus describes an identification procedure developed to retrieve the main material parameters l_A^2, l_B^4 and l_C^2 from the fields obtained with the set-up presented in Sect. 2.2. The measured wavelength-independent contribution $R_{wi}(x)$ translates the surface rotation $\frac{dv}{dx}(x)$ through a sensitivity field $d_\theta(x)$ that is obtained by a suited calibration procedure. The measured wavelength-dependent contribution $R_{wd}(x)$ describes the surface chemical modification.

For the sake of generality, the R_{wd} field is expanded on a user-defined functional basis $\langle \Psi_w(x) \rangle_{w=0,1,\ldots}$. It is further assumed that it translates the intensity of the local chemical modification, so that one assumes

$$\frac{\acute{b_0}}{Et} = \alpha \sum_w \gamma_w \Psi_w(x) \tag{2.75}$$

where $\langle \gamma_w \rangle_{w=0,1,\ldots}$ are the coefficients of the above-mentioned expansion. α is an optical parameter describing the reflectivity change induced by the chemical modification under scrutiny. This assumption is very similar to Eq. 2.53 and α (as well as F in Sect. 3.1.4) are unknowns to be determined.

One also assumes that the chosen functional basis is chosen such that

$$\frac{\mathrm{d}^4}{\mathrm{d}x^4}\Psi_w(x) = 0 \quad \forall w \tag{2.76}$$

The loading $\frac{b_0'}{Et}$ thus only affects the boundary conditions when calculating the chemically-induced kinematic fields, so that the rotation field linearly depends on the projections $\langle\gamma_w\rangle_{w=0,1,\ldots}$. Turning to a pixel-valued rotation field $\frac{dv}{dx}(x)$, this may be formally written as

$$\frac{\mathbf{dv}}{\mathbf{dx}}(\mathbf{x}) = \alpha\mathcal{M}(x, l_A^2, l_B^4, l_C^2, L)\gamma \tag{2.77}$$

where $\frac{\mathbf{dv}}{\mathbf{dx}}(\mathbf{x})$ is the rotation field recast as a vector, γ is a vector gathering the coefficients $\langle\gamma_w\rangle_{w=0,1,\ldots}$ and $\mathcal{M}$ a matrix obtained from Eq. 2.74. Similarly, one defines the matrix $\mathcal{T}$ so that

$$\mathbf{d}_\theta(\mathbf{x})\frac{\mathbf{dv}}{\mathbf{dx}}(\mathbf{x}) = \alpha\mathcal{T}(x, l_A^2, l_B^4, l_C^2, L)\gamma \tag{2.78}$$

and the matrix $\mathcal{P}$ gathering the pixel-valued components of the user-defined functional basis $\Psi_w(x)$. The pixel-valued measured fields $R_{wi}(x)$ and $R_{wd}(x)$ are also represented by the vectors $\mathbf{R_{wi}}$ and $\mathbf{R_{wd}}$, respectively.

It is then proposed to consider the cost-function η_M^2

$$\begin{aligned}\eta_M^2 &= \int\left(R_{wi}(x) - d_\theta(x)\frac{dv}{dx}(x)\right)^2 dx + \int\left(R_{wd}(x) - \sum_w \gamma_w\Psi_w(x)\right)^2 dx \\ &= \eta_M^2\left(l_A^2, l_B^4, l_C^2, L, \alpha, \gamma\right)\end{aligned} \tag{2.79}$$

which is the sum of mechanical and chemical contributions. The contributions however share the same metric (dictated by the reflectivity changes), and also share (under the above described assumptions) a simple dependence to the coefficients $\langle\gamma_w\rangle_{w=0,1,\ldots}$. η_M^2 is thus to be minimized to retrieve the material parameters as well as the projection γ and the coefficient α.

The optimal vector $\gamma_\mathbf{s}$ is obtained by first computing by singular value decomposition [207] the subspaces $I^\perp$ and $\mathcal{D}^\perp$ orthogonal to $\mathbf{R_{wi}}$ and $\mathbf{R_{wd}}$, respectively

$$I^{\perp t}\mathbf{R_{wi}} = \mathbf{0} \tag{2.80}$$

$$\mathcal{D}^{\perp t}\mathbf{R_{wd}} = \mathbf{0} \tag{2.81}$$

The matrix Q is defined

$$Q = \mathcal{P}^t\mathcal{D}^\perp I^{\perp t}\mathcal{T} \tag{2.82}$$

It is easily verified that the optimal $\gamma_\mathbf{s}$ is collinear to the singular vector $\gamma_\mathbf{Q}$ associated with the least singular value of $Q + Q^t$. The scaling factor α_Q such that

$$\gamma_\mathbf{s} = \alpha_Q\gamma_\mathbf{Q} \tag{2.83}$$

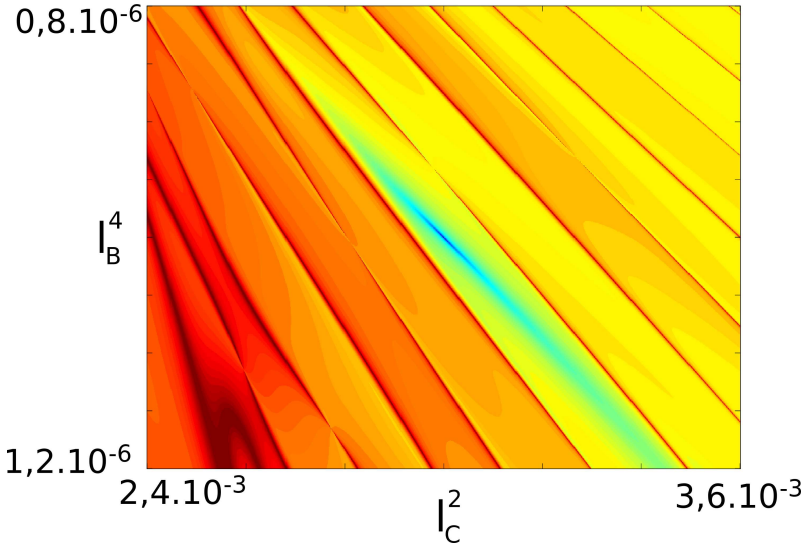

Figure 2.15: Map of $\eta_l^2(l_A^2 = 10^{-3}, l_B^4, l_C^2)$ obtained for the displacement fields of FIG.2.14 and assuming uniform chemical loadings (a single constant function in the functional basis $\langle \Psi_w(x) \rangle$).

is easily obtained as a minimizer of the sole chemical contribution to η_M^2

$$\alpha_Q = \frac{\mathbf{R_{wd}}^t \mathcal{P} \boldsymbol{\gamma}_\mathbf{Q}}{\boldsymbol{\gamma}_\mathbf{Q}{}^t \mathcal{P}^t \mathcal{P} \boldsymbol{\gamma}_\mathbf{Q}} \tag{2.84}$$

Similarly, the optimal scaling factor α_s is subsequently obtained as the minimizer of the sole mechanical contribution

$$\alpha_s = \frac{\mathbf{R_{wi}}^t \mathcal{T} \boldsymbol{\gamma}_\mathbf{s}}{\boldsymbol{\gamma}_\mathbf{s}{}^t \mathcal{T}^t \mathcal{T} \boldsymbol{\gamma}_\mathbf{s}} \tag{2.85}$$

The cost-function η_M^2 is thus minimized with respect to $\boldsymbol{\gamma}$ and α for a given set $\{l_A^2, l_B^4, l_C^2\}$, thus defining (discarding the dependance to the cantilever length L)

$$\begin{aligned} \eta_l^2(l_A^2, l_B^4, l_C^2) &= \min_{\boldsymbol{\gamma}, \alpha} \eta_M^2(l_A^2, l_B^4, l_C^2, \boldsymbol{\gamma}, \alpha) \\ &= \eta_M^2(l_A^2, l_B^4, l_C^2, \boldsymbol{\gamma}_\mathbf{s}, \alpha_s) \end{aligned} \tag{2.86}$$

For a given user-defined basis, η_l^2 is thus a function of the sole material parameter under scrutiny. FIG.2.15 displays the map $\eta_l^2(l_A^2 = 10^{-3}, l_B^4, l_C^2)$ obtained for the displacement fields of FIG.2.14 (100 pixels, $l_A^2 = 10^{-3}$, $l_B^4 = 10^{-6}$, $l_C^2 = 3 \times 10^{-3}$, $L = 2$ and assuming a uniform chemical loading). The function η_l^2 has been obtained assuming that only uniform chemical loadings are to be sought, so that $\langle \Psi_w(x) \rangle = \Psi_0 = 1$. A single absolute minimum is found as expected, even though local minima may exist further away from the solution. It is thus thought that iteratively minimizing $\eta_l^2(l_A^2, l_B^4, l_C^2)$ from a reasonable initial guess using standard algorithms such as the conjugate gradient method (including the constrains 2.61-2.65) would yield the actual material parameters.

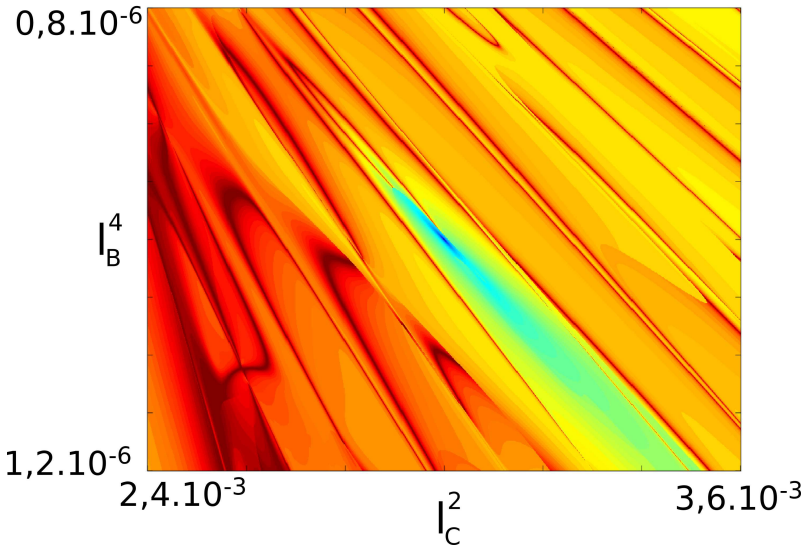

Figure 2.16: Map of $\eta_l^2(l_A^2 = 10^{-3}, l_B^4, l_C^2)$ obtained for the displacement fields of FIG.2.14 and assuming cubic chemical loadings.

Reproducing the same procedure when enlarging the user-defined functional basis so that it describes polynomial chemical loadings up to the third order yields the map displayed in FIG.2.16. This adds a rather limited complexity to the cost-function landscape, so that the material parameter identification should not be affected by the choice of the user-defined functional basis.

Finally, it should be mentioned that these maps have also been drawn when corrupting the measured fields with a gradually increasing, spatially uncorrelated, Gaussian noise. For up to 30% noise levels, the maps obtained with or without noise are barely distinguishable, an almost constant value is simply added to the residual. This also supports the idea that the involved material parameters should be identifiable using the set-up described in Sect. 2.2 and the above-described identification procedure.

An Euler-Bernoulli beam theory for isotropic elastic materials based on a second strain gradient description with a through-thickness cohesion modulus gradient has been derived in this section. This is thought to accurately describe the mechanical behavior of micro-cantilever sensors, and closed-form solutions are obtained for chemical loadings. The proposed modeling involves 6 material parameters, and only 4 (Young's modulus included) when the cantilever thickness is large enough. The shape of the displacement field resulting from a chemical loading is found to depart from the uniform curvature resulting from Stoney's assumptions, and depends on the cantilever thickness as well as on the material parameters. Such a theory may then potentially contribute to explain some of the controversial experimental results found in the literature (when dealing with amorphous or polymeric materials). These potentialities are to be experimentally confirmed and thus require a robust experimental identification procedure. Such a procedure exploit-

ing full-field measurements obtained with the set-up described in Sect. 2.2 is proposed and validated on computer-generated data. The research effort is then oriented toward the use of this set-up with cantilevers made of a homogeneous, isotropic material, in order to test for the validity range of this second strain gradient description. Choosing such a material, which should simultaneously

- allow the implementation of a suited calibration procedure for the measurement set-up (of Sect. 2.2) when the cantilever is made of a single material and thus does not feature any bimaterial effect (see Sect. 2.2.3);
- display surfaces which are easy to chemically modify;

is thus the next barrier to overcome.

Conclusion and Perspectives

It is shown herein that full-field measurements provide the opportunity to circumvent the difficulties arising when dealing with two experimental aspects of the mechanics of micrometer-sized structures.

- The need to assess elastic parameters for the used materials has generated a plethora of characterization methods as a result of the diversity of the possible options to strike the balance between various needs and constrains:
  - One has to access the local mechanical state in the structure under scrutiny;
  - This testing structure should be easily reproducible, and this is a real challenge with micrometer-sized structures (because of the geometrical fluctuations and of the material properties);
  - The testing device should be easy to handle.

  By relaxing the need to establish a uniform stress/strain state in the tested volume, full-field measurements allow the use of micrometer-sized structures (for which the geometrical margins become comparable to their smallest dimension) to access the mechanical properties of the involved materials. As these micrometer-sized structures are usually defined out of thin films and are thus essentially two-dimensional, the kinematic hypothesis associated with plate or beam theories may be used to estimate the displacement at any point of the structure from the displacement field measured at their surface. It has been shown that reflective patterns may be deposited onto these films (Chap. 1, Sect.2.2) to allow for digital image correlation for instance, and various systems (such as the one presented in Chap. 1, Sect. 2.1) provide access to the out-of-plane deformation of the structures.

  Alternatively, it is proposed to characterize thin film materials without involving any micromachined structure. The Scanning Microdeformation Microscope has been revisited to allow for a robust estimation of the decoupled elastic parameters of isotropic materials (Chap. 1, Sect. 3.2). Efforts are now put to extend this characterization method to anisotropic materials and should benefit from full-field measurements near the tip (Chap. 1, Sect. 3.3).

- Downsizing mechanical structures significantly increases their surface/volume ratio, so that micrometer-sized structures have also been shown to deform as a result

of the (heterogeneous) chemical modification of their surface. This has been exploited to devise micromechanical sensors for a wide range of target molecules, but the modeling effort has been somehow left behind. Describing surface effects in the continuum mechanics framework is particularly challenging and two possible approaches are described:

- The first one considers the surface as a volume whose thickness vanishes and that is ascribed to deform together with the underlying body. A thermodynamic analysis is used to set the surface mechanical parameters, and an asymptotic analysis is used to retrieve the body deformation.
- The second one is based on second-strain gradient elasticity, which has been shown to feature a cohesion modulus defining a surface property. The corresponding Euler-Bernoulli beam theory is shown to involve only three additional elastic parameters, so that the complexity remains modest enough to allow their identification from experimental data.

For both approaches, it has been shown that full-field measurements obtained with an innovative imaging set-up described in Chap. 2, Sect. 2.2 provide the mechanical and chemical information required to identify the involved parameters, and the described identification procedures yields a figure of merit of the chosen framework.

These two examples thus illustrate the importance of accessing redundant mechanical data when dealing with the mechanics of micrometer-sized structures. As already mentioned, further developments for the elastic characterization of materials will focus on extending the proposed approach to anisotropic materials. Considering the surface coupling phenomena, the two proposed modeling frameworks allow to draw perspectives along two lines:

- The choice among the exposed modeling frameworks should be based on a wide range of experimental systems, ranging from model systems (cantilevers made of a uniform isotropic material) to multi-layered systems (such as those proposed in Chap. 2, Sect. 2.1). In should be highlighted that the two frameworks represent two rather different options, namely, the surface effect is described either as extrinsic for an asymptotic analysis or as a material parameter (intrinsic) in the second-strain gradient theory. It is first to be noted that under the latter, identifying the material parameters driving the structure response **is** identifying elastic parameters, thus somehow merging the two main lines (elasticity and surface couplings) of the work described herein. Second, choosing among these two frameworks will have major consequences on the further developments of the field. Where the second-strain gradient elasticity framework is shown to be the more adequate, it paves the way to material optimization and to the extensive study of the relationships between the processing conditions and the properties of the obtained multi-functional materials.

- Regarding applications, it seems that the development of innovative cantilever sensors has been rather limited the very last years, despite the significant effort made to develop commercial set-ups. This approach may however be renewed in case the above-mentioned modeling effort demonstrates that alternative kinematic quantities should be measured to yield unambiguous data in sensing applications. Besides these applications relying on the mechanical transduction of chemical stimuli, it should be highlighted that the reverse coupling (*i.e.,* chemical modifications induced by a mechanical deformation) on similar systems has received very little attention so far. There is thus a clear field for investigations there and the target point could be the development of homeostatic systems such as the recently proposed hydrogel-based systems [13]. The use of silicon-based materials or metals exploiting the above-studied coupling phenomena (instead of the volume change of hydrogels) would probably lead to a new family of homeostatic systems possibly featuring much higher energy densities.

Appendix

Appendix : SMM modeling

The expression for condition (1.80) reads

$$\begin{aligned}\mathcal{R}(f,p_0,p_1,p_2,p_3,p_4,p_5,p_6,p_7,p_8,p_9,X,Z) = \frac{1}{6\mu(f,p_0)^4 p_2^2}\\ \left\{3p_3^2X\left[6XZ-p_1p_9\mu(f,p_0)^4(2Z+1)\right]F_1(f,p_0,p_4,p_5,p_6,p_7,p_8)\right.\\ +p_3^2\mu(f,p_0)^3\left(p_1p_9\mu(f,p_0)^4-6XZ\right)F_2(f,p_0,p_1,p_4,p_5,p_6,p_7,p_8)\\ +6\mu(f,p_0)\left(3X-p_1p_9\mu(f,p_0)^4\right)F_3(f,p_0,p_1,p_2,p_4,p_5,p_6,p_7,p_8)\\ \left.+6\mu(f,p_0)^4F_4(f,p_0,p_1,p_2,p_4,p_5,p_6,p_7,p_8)\right\}\\ +\frac{p_1^2p_9^2p_3^2\mu(f,p_0)^4}{6p_2^2}F_1(f,p_0,p_4,p_5,p_6,p_7,p_8)=0\end{aligned} \tag{87}$$

where the functions F_i stand for

$$\begin{aligned}F_1 \quad & (f,p_0,p_4,p_5,p_6,p_7,p_8) =\\ & \theta(f,p_0,p_4,p_5)\left[\Sigma(f,p_0,p_6,p_7)\,T_1(f,p_0,p_8)+T_2(f,p_0,p_8)\right]\\ & +\Sigma(f,p_0,p_6,p_7)\,T_3(f,p_0,p_8)+T_4(f,p_0,p_8)\end{aligned} \tag{88}$$

$$\begin{aligned}F_2 \quad & (f,p_0,p_1,p_4,p_5,p_6,p_7,p_8) =\\ & \theta(f,p_0,p_4,p_5)\left[\Sigma(f,p_0,p_6,p_7)\,T_5(f,p_0,p_1,p_8)+T_6(f,p_0,p_1,p_8)\right]\\ & +\Sigma(f,p_0,p_6,p_7)\,T_7(f,p_0,p_1,p_8)+T_8(f,p_0,p_1,p_8)\end{aligned} \tag{89}$$

$$\begin{aligned}F_3 \quad & (f,p_0,p_1,p_2,p_4,p_5,p_6,p_7,p_8) =\\ & \theta(f,p_0,p_4,p_5)\left[\Sigma(f,p_0,p_6,p_7)\,T_9(f,p_0,p_1,p_2,p_8)+T_{10}(f,p_0,p_1,p_2,p_8)\right]\\ & +\Sigma(f,p_0,p_6,p_7)\,T_{11}(f,p_0,p_1,p_2,p_8)+T_{12}(f,p_0,p_1,p_2,p_8)\end{aligned} \tag{90}$$

$$\begin{aligned}F_4 \quad & (f,p_0,p_1,p_2,p_4,p_5,p_6,p_7,p_8) =\\ & \theta(f,p_0,p_4,p_5)\left[\Sigma(f,p_0,p_6,p_7)\,T_{13}(f,p_0,p_1,p_2,p_8)+T_{14}(f,p_0,p_1,p_2,p_8)\right]\\ & +\Sigma(f,p_0,p_6,p_7)\,T_{15}(f,p_0,p_1,p_2,p_8)+T_{16}(f,p_0,p_1,p_2,p_8)\end{aligned} \tag{91}$$

and the T_i read

$$T_1(f,p_0,p_8) = C^-(L)C^-(L)+S^-(L)S^+(L) \tag{92}$$

$$T_2(f,p_0,p_8) = S^+(L)C^-(L)-S^-(L)C^+(L) \tag{93}$$

$$T_3(f,p_0,p_8) = C^-(L)S^-(L)-C^+(L)S^+(L) \tag{94}$$

$$T_4(f,p_0,p_8) = S^-(L)S^+(L)+C^+(L)C^+(L) \tag{95}$$

where the functions defined by Eqs.(1.69-1.70) should be seen as functions of (f, p_0, p_8) if taken at $x = L$

$$\begin{aligned}
T_5(f,p_0,p_1,p_8) &= C^-(L)\,U_1(f,p_0,p_1,p_8) - S^+(L)\,U_2(f,p_0,p_1,p_8) && (96)\\
T_6(f,p_0,p_1,p_8) &= -C^-(L)\,U_3(f,p_0,p_1,p_8) + C^+(L)\,U_2(f,p_0,p_1,p_8) && (97)\\
T_7(f,p_0,p_1,p_8) &= S^-(L)\,U_1(f,p_0,p_1,p_8) - S^+(L)\,U_4(f,p_0,p_1,p_8) && (98)\\
T_8(f,p_0,p_1,p_8) &= -S^-(L)\,U_3(f,p_0,p_1,p_8) + C^+(L)\,U_4(f,p_0,p_1,p_8) && (99)
\end{aligned}$$

with

$$\begin{aligned}
U_1(f,p_0,p_1,p_8) &= S^-(L) + \mu(f,p_0)\,p_1 C^-(L) && (100)\\
U_2(f,p_0,p_1,p_8) &= C^+(L) - \mu(f,p_0)\,p_1 S^-(L) && (101)\\
U_3(f,p_0,p_1,p_8) &= C^-(L) - \mu(f,p_0)\,p_1 S^+(L) && (102)\\
U_4(f,p_0,p_1,p_8) &= S^+(L) + \mu(f,p_0)\,p_1 C^+(L) && (103)
\end{aligned}$$

$$\begin{aligned}
T_9(f,p_0,p_1,p_2,p_8) &= S^-(L)\,V_1(f,p_0,p_1,p_2,p_8)\\
&\quad -C^-(L)\,V_2(f,p_0,p_1,p_2,p_8) && (104)\\
T_{10}(f,p_0,p_1,p_2,p_8) &= S^-(L)\,V_3(f,p_0,p_1,p_2,p_8)\\
&\quad -S^+(L)\,V_2(f,p_0,p_1,p_2,p_8) && (105)\\
T_{11}(f,p_0,p_1,p_2,p_8) &= C^-(L)\,V_4(f,p_0,p_1,p_2,p_8)\\
&\quad -C^+(L)\,V_1(f,p_0,p_1,p_2,p_8) && (106)\\
T_{12}(f,p_0,p_1,p_2,p_8) &= S^+(L)\,V_4(f,p_0,p_1,p_2,p_8)\\
&\quad -C^+(L)\,V_3(f,p_0,p_1,p_2,p_8) && (107)
\end{aligned}$$

with

$$\begin{aligned}
V_1(f,p_0,p_1,p_2,p_8) &= p_2^2 C^+(L) - p_1\mu(f,p_0)^3 S^+(L) && (108)\\
V_2(f,p_0,p_1,p_2,p_8) &= p_2^2 S^+(L) + p_1\mu(f,p_0)^3 C^-(L) && (109)\\
V_3(f,p_0,p_1,p_2,p_8) &= p_2^2 S^-(L) + p_1\mu(f,p_0)^3 C^+(L) && (110)\\
V_4(f,p_0,p_1,p_2,p_8) &= p_2^2 C^-(L) - p_1\mu(f,p_0)^3 S^-(L) && (111)
\end{aligned}$$

The free resonance condition (*i.e.,* when the resonator is not in contact) is obtained by setting $X = 0$ and $p_9 = 0$

$$\begin{aligned}
&\mathcal{R}_{free}(f,p_0,p_1,p_2,p_4,p_5,p_6,p_7,p_8) =\\
&\quad \frac{1}{\mu^4(f,p_0)p_2^2}\left\{\mu(f,p_0)\left[p_0p_4 - p_5\mu^4\right]T_{14}(f,p_0,p_1,p_2,p_8)\right.\\
&\quad + \left[p_0^2p_4p_7 - p_0p_4p_6\mu(f,p_0)^4 - p_0p_5p_7\mu(f,p_0)^4 + p_5p_6\mu(f,p_0)^8\right]T_{13}(f,p_0,p_1,p_2,p_8)\\
&\quad + \mu(f,p_0)^3\left[p_0p_7 - \mu(f,p_0)^4p_6\right]T_{15}(f,p_0,p_1,p_2,p_8)\\
&\quad \left. + \mu(f,p_0)^4T_{16}(f,p_0,p_1,p_2,p_8)\right\} = 0 \qquad (112)
\end{aligned}$$

Appendix : Acronyms

AFM: Atomic Force Microscope
ASTM: American Society for Testing and Materials
DIC: Digital Image Correlation
EBSD: Electron BackScatter Diffraction
ESPI: Electronic Speckle Pattern Interferometry
FF-SMM: Full-Field Scanning Microdeformation Microscope
FIB: Focused Ion Beam
MEMS: Micro-Elctro-Mechanical Systems
MM-SMM: Multiple-Mode Scanning Microdeformation Microscope
PAS: Plane of Apparent Splitting
PDMS: Poly-DiMethylSiloxane
PSD: Position-Sensitive Detector
SEM: Scanning Electron Microscope
SMM: Scanning Microdeformation Microscope
TE: Transverse Electrical
TEL: Thermodynamically Equivalent Layer
TEM: Transmission Electron Microscope
TM: Transverse Magnetic

Bibliography

[1] DREXLER E. (1981). Molecular engineering: an approach to the development of general capabilities for molecular manipulation, *Proc. Natl. Acad. Sci USA*, 78 (9), p. 5275-5278.

[2] BINNIG G., ROHRER H., GERBER C. and WEIBERL E. (1982). Tunneling through a controllable vacuum gap, *Appl. Phys. Lett.*, 40 (2), p. 178-180.

[3] HAUFLER R.E., WANG L.S., CHIBANTE L.P.F., JIN C., CONCEICAO J., CHAI Y. and SMALLEY R.E. (1991). Fullerene triplet state production and decay: R2PI probes of C60 and C70 in a supersonic beam, *Chem Phys. Lett.*, 179(5-6), p. 449-454.

[4] KARN B., KUIKEN T. and OTTO M. (2009). Nanotechnology and in situ remediation : a review of the benefits and potential risks, *Environmental Health Perspectives*, 117(12), p. 1823-1831.

[5] ESTEBAN M., WEBERSIK C., LEARY D. and THOMPSON-POMEROY D. (2008). Innovation in Responding to Climate Change: Nanotechnology, Ocean Energy and Forestry, *United Nations University Institute of Advanced Studies*. `http://www.ias.unu.edu/resource_centre/...`
`InnovationinRespondingtoClimateChange_UNU-IASReport.pdf`

[6] KEITH D.W. (2010). Photophoretic levitation of engineered aerosols for geoengineering. *PNAS*, 107(38), p. 16428-16431.

[7] LI C., LY J., LEI B., FAN W., ZHANG D., HAN J., MEYYAPPAN M., THOMPSON M. and ZHOU C. (2004). Data storage studies on nanowire transistors with self-assembled porphyrin molecules. *J. Phys. Chem. B*, 108, p. 9646-9649.

[8] ROCO M.C. (2003). Nanotechnology : convergence with modern biology and medicine. *Current opinion in biotechnology*, 14, p. 337-346.

[9] KEARNES M. and MACNAGHTEN P. (2006). Introduction : (Re)imagining nanotechnology. *Science as culture*, 15(4), p. 279-290.

[10] `http://www.asyousow.org/health_safety/nanoissuebrief.shtml`

[11] MASSE R. and BOUDÈNE C. Are nanoparticles a new class of environmental toxin? *Bull. Acad. Natle Méd.*, 195(9), p. 2037-2043.

[12] FRITZ J., BALLER M.K., LANG H.P., ROTHUIZEN H., VETTIGER P., MEYER E., GÜNTHERODT H., GERBER C. and GIMZEWSKI J.K. (2000). Translating biomolecular recognition into nanomechanics. *Science*, 288, p. 316-318.

[13] HE X., AIZENBERG M., KUKSENOK O., ZARZAR L.D., SHASTRI A., BALAZS A.C. and AIZENBERG J. (2012). Synthetic homeostatic materials with chemo-mechano-chemical self-regulation. *Nature*, 487(7406), p. 214-218.

[14] `http://www.mmta.co.uk/silicon-market-overview`

[15] FUNKE C., KUNA M. and MÖLLER H.-J. (2004) Biaxial fracture test of silicon wafers. *Advanced engineering materials*, 6(7), p. 594-598.

[16] PEARCE C.A. and GURUSWAMY S. (2008) New biaxial flexure test device for ultrathin single crystal wafers. *J. Am. Ceram. Soc.*, 91(12), p. 4023-4028.

[17] RUPNOWSKI P. and SOPORI B. (2009) Strength of silicon wafers : fracture mechanics approach. *Int. J. Fract.*, 155, p. 67-74.

[18] BORRERO-LÓPEZ O., VODENITCHAROVA T., HOFFMAN M. and LEO A.J. (2009) Fracture strength of polycrystalline silicon wafers for the photovoltaic industry. *J. Am. Ceram. Soc.*, 92(11), p. 2713-2717.

[19] FUNKE C., WOLF S. and STOYAN D. (2009) Modeling the tensile strength and crack length of wire-sawn silicon wafers. *Journal of solar energy engineering*, 131, p. 011-012.

[20] RUPNOWSKI P., SOPORI B., ARMENTROUT D. and GOOD E. (2010) Strength of multicrystalline silicon wafers for various surface conditions. *Mater. Res. Soc. Symp. Proc.*, 1210, p. 127-132.

[21] CHAE S.-H., ZHAO J.-H., EDWARDS D.R. and HO P.S. (2010) Effect of dicing technique on the fracture strength of Si dies with emphasis on multimodal failure distribution. *IEEE Transactions on Device and Materials Reliability*, 10(1), p. 149-156.

[22] KAMAT S.V. (2009). Experimental techniques for the measurement of mechanical properties of materials used in microelectromechanical systems.*Defence Science Journal*, 59(6), p. 605-615.

[23] MUHLSTEIN C.L., BROWN S. B. and RITCHIE R.O. (2001) High-cycle fatigue of single-crystal silicon thin films. *J. Microelectromechanical systems*, 10(4), p. 593-600.

[24] COMTOIS J.H., MICHALICEK M.A. and BARRON C.C. (1997). Fabricating micro-Instruments in surface-micromachined polycrystalline silicon. In *Proceedings of the 43th International Instrumentation Symposium*, p. 169-179.

[25] JAYARAMAN S., EDWARDS R.L. and HEMKER K.J. (1999). Relating mechanical testing and microstructural features of polysilicon thin films. *J. Mater. Res.*, 14(3), p. 688-697.

[26] SHARPE JR W.N. and BAGDAHN J. (2004) Fatigue testing of polysilicon, a review. *Mechanics of Materials*, 36, p. 3-11.

[27] MUHLSTEIN C.L., HOWE R.T. and RITCHIE R.O. (2004) Fatigue of polycrystalline silicon for microelectromechanical system applications: crack growth and stability under resonant loading conditions. *Mechanics of Materials*, 36(1-2), p. 13-33.

[28] ALSEM D.H., STACH E.A., MUHLSTEIN C.L. and RITCHIE R.O. (2005) Fatigue failure in thin-film polycrystalline silicon is due to subcritical cracking within the oxide layer. *Appl. Phys. Lett.*, 86(4), 041914.

[29] KAHN H., AVISHAI A., BALLARINI R. and HEUER A.H. (2008) Surface oxide effects on failure of polysilicon MEMS after cyclic and monotonic loading. *Scripta Materialia*, 59, p. 912-915.

[30] ALSEM D.H., MUHLSTEIN C.L., STACH E.A. and RITCHIE R.O. (2008) Further considerations on the high-cycle fatigue of micron-scale polycrystalline silicon. *Scripta Materialia*, 59, p. 931-935.

[31] KAMIYA S., IKEDA Y., GASPAR J. and PAUL O. (2011) Effect of humidity and temperature on the fatigue behavior of polysilicon thin film. *Sensor and actuator A*, 170, p. 187-195.

[32] FERRARIS E., FASSI I. and DEL SARTO M. (2008) Fatigue life investigation of the 15 μm thick ThELMA epitaxial polysilicon. *Sensor Letters*, 6(1), p. 57-68.

[33] LANGFELDER G., DELLEA S., ZARAGA F., CUCCHI D. and AZPEITIA URQUIA M. (2012) The dependence of fatigue in microelectromechanical systems on the environment and the industrial packaging. *IEEE Transactions on Industrial Electronics*, 59(12), p. 4938-4948.

[34] THEILLET P.-O. and PIERRON O.N. (2009) Fatigue rates of monocrystalline silicon thin films in harsh environments: influence of stress amplitude, relative humidity, and temperature. *Appl. Phys. Lett.*, 94, 181915.

[35] BAUMERT E.K., THEILLET P.-O. and PIERRON O.N. (2010) Investigation of the low-cycle fatigue mechanism for micron-scale monocrystalline silicon films. *Acta Materialia*, 58, p. 2854-2863.

[36] THEILLET P.-O. and PIERRON O.N. (2011) Quantifying adsorbed water monolayers on silicon MEMS resonators exposed to humid environments. *Sensors and Actuators A*, 171, p. 375-380.

[37] BAUMERT E.K., THEILLET P.-O. and PIERRON O.N. (2011) Fatigue-resistant silicon films coated with nanoscale alumina layers. *Scripta Materialia*, 65, p. 596-599.

[38] ERICSON F. and SCHWEITZ J.-Å. (1990) Micromechanical fracture strength of silicon. *J. Appl. Phys.*, 68(11), p. 5840-5844.

[39] WILSON C.J., ORMEGGI A. and NARBUTOVSKIH M. (1996). Fracture testing of silicon microcantilever beams. *J. Appl. Phys.*, 79(5), p. 2386-2393.

[40] GREEK S., ERICSON F., JOHANSSON S. and SCHWEITZ J.-Å. (1997). In situ tensile strength measurement and Weibull analysis of thick film and thin film micromachined polysilicon structures. *Thin Solid Films*, 292, p. 247-254.

[41] BOYCE B.L., SHAW M.J., LU P. and DUGGER M.T. (2010). Stronger silicon for microsystems. *Acta Materialia*, 58, p. 439-448.

[42] GAITHIER M.S., DELRIO F.W., GATES R.S., FULLER JR E.R. and COOK R.F. (2010). Strength distribution of single-crystal silicon theta-like specimens. *Scripta Materialia*, 63, p. 422-425.

[43] GAITHIER M.S., GATES R.S., KIRKPATRICK R., COOK R.F. and DELRIO F.W. (2013) Etching process effects on surface structure, fracture strength, and reliability of single-crystal silicon theta-like specimens. *Jal Microelectromechanical Systems*, 22(3), p. 589-602.

[44] DELUCA M., BERMEJO R., PLETZ M., SUPANCIC P. and DANZER R. (2011) Strength and fracture analysis of silicon-based components for embedding. *Journal of the European Ceramic Society*, 31(4), p. 549-558.

[45] BORRERO-LÓPEZ O., HOFFMAN M., BENDAVID A. and MARTIN P.J. (2009). Reverse size effect in the fracture strength of brittle thin films. *Scripta Materialia*, 60, p. 937-940.

[46] JONNALAGADDA K.N. and CHASIOTIS I. (2009). Strength and fracture resistance of amorphous diamond-like carbon films for MEMS. Journal of Nanomaterials, 2009, 204281.

[47] MARIANI S., GHISI A., CORIGLIANO A. and ZERBINI S. (2007). Multi-scale analysis of MEMS sensors subject to drop impacts. *Sensors*, 7, p. 1817-1833.

[48] KIMBERLEY J., CHASIOTIS I. and LAMBROS J. (2008). Failure of microelectromechanical systems subjected to impulse loads. *Int. J. Solids Structures*, 45, p. 497-512.

[49] MARIANI S., GHISI A., MARTINI R., CORIGLIANO A. and SIMONI B. (2010). Analysis of shock-induced polysilicon MEMS failure : a multi-scale finite element approach. In *Symposium on Design, Test, Integration and Packaging of MEMS/MOEMS, DTIP 2010* (5486521).

[50] MARIANI S., GHISI A., CORIGLIANO A., MARTINI R. and SIMONI B. (2011) Two-scale simulation of drop-induced failure of polysilicon MEMS sensors. *Sensors*, 11(5), p. 4972-4989.

[51] BORRERO-LÓPEZ O., HOFFMAN M., BENDAVID A. and MARTIN P.J. (2010). The use of the scratch test to measure the fracture strength of brittle thin films. *Thin Solid Films*, 518, p. 4911-4917.

[52] ALSEM D.H., VAN DER HULST R., STACH E.A., DUGGER M.T., DE HOSSON J.TH.M. and RITCHIE R.O. (2010). Wear mechanisms and friction parameters for sliding wear of micron-scale polysilicon sidewalls. *Sensors and Actuators A*, 163, p. 373-382.

[53] KAUSHIK A. KAHN H. and HEUER A.H. (2005) Wafer level mechanical characterization of silicon nitride MEMS. *J. Electromechanical Systems*, 14(2), p. 359-367.

[54] LIU X., METCALF T.H., WANG Q. and PHOTIADIS D.M. (2007) Elastic properties of several silicon nitride films. *Mater. Res. Soc. Symp. Proc.*, 989, p. 511-515.

[55] REN Y. and LAM D. C. C. (2005) Experiments on the elastic size dependence of LPCVD silicon nitride. *Mater. Res. Soc. Symp. Proc.*, 875.

[56] MESCHER M.J., REED M.L. and SCHLESINGER T.E. (1997) Stress control in sputtered silicon nitride films. *Mater. Res. Soc. Symp. Proc.*, 472, p. 239-244.

[57] KIM J.H., LEE W. S. and CHUNG K. W. (1998) Correlation between the mechanical stress and microstructure in reactive bias magnetron sputtered silicon nitride films. *Mater. Res. Soc. Symp. Proc.*, 505, p. 421-426.

[58] READ D.T., CHENG Y.-W., KELLER R.R. and MCCOLSKEY J.D. (2001). Tensile properties of free-standing aluminum thin films. *Scripta Materialia*, 45, p. 583-589.

[59] HE S., CHANG J.S., LI L. and HO H. (2009). Characterization of Young's modulus and residual stress gradient of MetalMUMPs electroplated nickel film. *Sensors and Actuators A*, 154, p. 149-156.

[60] PARK J.-H., BAE H.-Y. and KIM Y.-J. (2010). Determination of tensile properties and residual stresses of Ni-Co thin films. *Int. Jal. Precision engineering and manufacturing*, 11(5), p. 771-778.

[61] LIN M.-T., TONG C.-J. and SHIU K.-S. (2010). Novel microtensile method for monotonic and cyclic testing of freestanding copper thin films. *Experimental Mechanics*, 50, p. 55-64.

[62] SHAN W.L., YANG Y., HILLIE K.T., JORDAAN W.A. and SOBOYEJO W.O. (2013). Role of oxide thickening in fatigue crack initiation in LIGA nickel MEMS thin films. *Materials Science and Engineering A*, 561, p. 434-440.

[63] DE PASQUALE G., SOMÀ A. and BALLESTRA A. (2009). Mechanical fatigue analysis of gold microbeams for RF-MEMS applications by pull-in voltage monitoring. *Analog Integr. Circ Sig Process*, 61, p. 215-222.

[64] HWANGBO Y. and SONG J.-H. (2010). Fatigue life and plastic deformation behavior of electrodeposited copper thin films. *Mater. Sci. Eng.*, 527, p. 2222-2232.

[65] WANG H., LIU R., MAO S.-P., TANG J., ZHANG C.-C. and DING G.-F. (2009). Effect of specimen size on Young's modulus of electrodeposited Ni. *Surface Review and Letters*, 16(2), p. 303-307.

[66] ÖVEÇOĞLU M.L., DOERNER M.F. and NIX W.D. (1987). Elastic interactions of screw dislocations in thin films on substrates. *Acta Metall.*, 35(12), p. 2947-2957.

[67] RUPERT T.J., GIANOLA D.S., GAN Y. and HEMKER K.J. (2009). Experimental observations of stress-driven grain boundary migration. *Science*, 326, p. 1686-1690.

[68] PRIESTER L., COUZINIÉ J.-P., DÉCAMPS B. and LARTIGUE-KORINEK S. (2010). Interactions between dislocations and interfaces : consequences for metal and ceramic plasticity. *Int. J. Mat. Res.*, 101(10), p. 1202-1210.

[69] SHAW J. M., GELORME J. D., LABIANCA N. C., CONLEY W. E. and HOLMES S. J. (1997). Negative photoresists for optical lithography. *IBM Journal of Research and Development*, 41, p. 81-94.

[70] DESPONT M., LORENZ H., FAHRNI N., BRUGGER J., RENAUD P. and VETTIGER P. (1997). High aspect ratio ultrathick, negative-tone near-UV photoresist for MEMS applications. In *Proc. MEMS'97, IEEE*, p. 518-522.

[71] LORENZ H., DESPONT M., FAHRNI M., LABIANCA N., VETTIGER P. and RENAUD P. (1997). SU-8: a low-cost negative resist for MEMS. *J. Micromech. Microeng.*, 7, p. 121-124.

[72] MCALEAVEY A., COLES G., EDWARDS R.L. and SHARPE JR. W.N. (1999). Mechanical properties of SU-8. *Materials Research Society Symposium - Proceedings*, 546, p. 213-218.

[73] VOGEL J., FEIGE H.-J., SAUPE J., SCHUBERT S. and GRIMM J. (2014). Mechanical material characterization of photosensitive polymers. *Microsystem technologies*, 20, p. 1975-1979.

[74] WEIHS T. P., HONG S., BRAVMAN J. C. and NIX W. D. (1988). Mechanical deflection of cantilever micro-beams: a new technique for testing the mechanical properties of thin films. *J. Mater. Res.*, 3(5), p. 931-942.

[75] FANG W. and WICKERT J. A. (1996). Determining mean and gradient residual stresses in thin films using micromachined cantilevers. *J. Micromech. Microeng.*, 6, p. 301-309.

[76] MOUNAIX P., DELOBELLE P., MÉLIQUE X., BORNIER L. and LIPPENS D. (1998). Micromachining and mechanical properties of GaInAs/InP microcantilevers, *Mat. Sci. Eng.*, B51, p. 258-262.

[77] SCHWEITZ J-Å and ERICSON F. (1999). Evaluation of mechanical materials properties by means of surface micromachined structures. *Sensors and Actuators*, 74, p. 126-133.

[78] FANG W. (1999). Determination of the elastic modulus of thin film materials using self-deformed micromachined cantilevers. *J. Micromech. Microeng.*, 9, p. 230-235.

[79] GRAVIER S., COULOMBIER M., SAFI A., ANDRÉ N., BOÉ A., RASKIN J.-P. and PARDOEN T. (2009). New on-chip nanomechanical testing laboratory - applications to aluminum and polysilicon thin films. *Jal Microelectromechanical systems*, 18(3), p. 555-569.

[80] HE J.H., LUO J.K., HOPCROFT M.A., LE H.R. and MOORE D.F. (2009). Nanomechanical charaterisation of MEMS thin film materials. *Int. J. Computational Materials Science and surface engineering*, 2(3-4), p. 342-354.

[81] HUANG Z., HONG W. and SUO Z. (2004). Evolution of wrinkles in hard films on soft substrate. *Phys. Rev. E*, 70, 030601.

[82] CHOI H.-J., KIM J.-H., LEE H.-J., SONG S.-A., LEE H.-J., HAN J.-H. and MOON M.-W. (2010). Wrinkle-based measurement of elastic modulus of nanoscale thin Pt film deposited on polymeric substrate : verification and uncertainty analysis. *Experimental Mechanics*, 50, p. 635-641.

[83] CHUNG J.-Y., NOLTE A.J. and STAFFORD C.M. (2011). Surface wrinkling : a versatile platform for measuring thin-film properties. *Adv. Mater.*, 23, p. 349-368.

[84] READ D.T. and DALLY J.W. (1993). A new method for measuring the strength and ductility of thin films, *J. Mater. Res.*, 8 (7), p. 1542-1549.

[85] SHARPE JR. W.N., YUAN B. and EDWARDS R. L. (1997). A new technique for measuring the mechanical properties of thin films. *Jal. microelectromechanical systems*, 6(3), p. 193-199.

[86] SHARPE JR. W.N., TURNER K.T. and EDWARDS R.L. (1999). Tensile testing of polysilicon. *Experimental Mechanics*, 39(3), p. 162-170.

[87] GAD-EL-HAK M. (2002), *The MEMS Handbook*, CRC Press.

[88] SHARPE JR W.N. and HEMKER K.J. (2002). Mechanical testing of free-standing thin films. *Mater. Res. Soc. Symp. Proc.*, 687, p. 293-304.

[89] SHARPE JR W.N. (2003). Murray Lecture - Tensile testing at the micrometer scale: opportunities in experimental mechanics, *Exp. Mech.*, 43(3), p. 228-237.

[90] SRIKAR V.T. and SPEARING S.M. (2003). A critical review of microscale mechanical testing methods used in the design of microelectromechanical systems, *Exp. Mech.*, 43 (3), p. 238-247.

[91] HAQUE M.A. and SAIF M.T.A. (2003). A review of MEMS-Based microscale and nanoscale tensile and bending testing, *Exp. Mech.*, 43 (3), p. 248-255.

[92] HEMKER K.J. and SHARPE JR. W.N. (2007). Microscale characterization of mechanical properties. *Annu. Rev. Mater. Res.*, 37, p. 93-126.

[93] SHARPE JR. W.N. (2008). A review of tension test methods for thin films. *Mater. Res. Soc. Symp. Proc.*, 1052, p. 3-14.

[94] BUCHHEIT T.E., GLASS S.J., SULLIVAN J.R., MANI S.S., LAVAN D.A., FRIEDMANN T.A. and JANEK R. (2003) Micromechanical testing of MEMS materials. *Journal of Materials Science*, 38, p. 4081-4086.

[95] JADAAN O.M., NEMETH N.N., BAGDAHN J. and SHARPE JR. W.N. (2003). Probabilistic Weibull behavior and mechanical properties of MEMS brittle materials. *J. Mat. Sci.*, 38, p. 4087-4113.

[96] CORIGLIANO A., GHISI A., LANGFELDER G., LONGONI A., ZARAGA F. and MERASSI A. (2011) A microsystem for the fracture characterization of polysilicon at the micro-scale. *European Journal of Mechanics, A/Solids*, 30(2), p. 127-136.

[97] HAZRA S.S., BAKER M.S., BEUTH J.L. and DE BOER M.P. (2011) Compact on-chip microtensile tester with prehensile grip mechanism. *Jal Microelectromechanical systems*, 20(4), p. 1043-1053.

[98] MINOTTI P., BOURBON G., JOSEPH E. and LE MOAL P. (2002). Generalized MEMS lot monitoring using fully integrated material and structure mechanical analysis, *Sensors and Actuators A*, 101, p. 220-230.

[99] GASPAR J., SCHMIDT M.E., HELD J. and PAUL O. (2009) Wafer-scale microtensile testing of thin films. *Journal of microelectromechanical systems*, 18(5), p. 1062-1076.

[100] ORTHNER M.P., RIETH L.W. and SOLZBACHER F. (2010). High speed wafer scale bulge testing for the determination of thin film mechanical properties. *Rev. Sci. Instr.*, 81, 055111.

[101] KANG W. and SAIF M.T.A. (2010). A novel method for in situ uniaxial tests at the micro/nano scale - Part I : theory. *Journal of microelectromechanical systems*, 19(6), p. 1309-1321.

[102] KANG W., HAN J.H. and SAIF M.T.A. (2010). A novel method for in situ uniaxial tests at the micro/nano scale - Part II : experiment. *Jal Microelectromechanical systems*, 19(6), p. 1322-1330.

[103] CORIGLIANO A., DOMENELLA L. and LANGFELDER G. (2010) On-chip mechanical characterization using an electro-thermo-mechanical actuator. *Experimental Mechanics*, 50, p. 695-707.

[104] UCHICH M.D., DIMIDUK D.M., FLORANDO J.N. and NIX W.D. (2004). Sample dimensions influence strength and crystal plasticity. *Science*, 305, p. 986-989.

[105] GREER J.R., KIM J.-Y. and BUREK M.J. (2009). The In-situ Mechanical Testing of Nanoscale Single-crystalline Nanopillars. *JOM*, 61(12), p. 19-25.

[106] LACROIX R., KERMOUCHE G., TEISSEIRE J. and BARTHEL E. (2012). Plastic deformation and residual stresses in amorphous silica pillars under uniaxial loading. *Acta Materialia*, 60, p. 5555-5566.

[107] FUJII T., NAMAZU T., SUDOH K., SAKAKIHARA S. and INOUE S. (2013). Focused ion beam induced surface damage effect on the mechanical properties of silicon nanowires. *Journal of engineering materials and technology*, 135, 041002.

[108] DAUM B., DEHM G., CLEMENS H., RESTER M., FISCHER F.D. and RAMMERSTORFER F.G. (2013). Elastoplastic buckling as source of misinterpretation of micropillar tests. *Acta Materialia* , 61, p. 4996-5007.

[109] MOSER B., WASMER K., BARBIERI L. and MICHLER J. (2007). Strength and fracture of Si micropillars : a new scanning electron microscopy-based microcompression test. *J. Mater. Res.*, 22(4), p. 1004-1011.

[110] KIENER D., GROSINGER W., DEHM G. and PIPPAN R. (2008). A further step towards an understanding of size-dependent crystal plasticity: in situ tension experiments of miniaturized single-crystal copper samples. *Acta Materialia*, 56, p. 580-592.

[111] GIANOLA G.S. and EBERL C. (2009) Micro- and nanoscale tensile testing of materials. *JOM*, 61(3), p. 24-35.

[112] DEHM G. (2009). Miniaturized single-crystalline fcc metals deformed in tension: new insights in size-dependent plasticity. *Progress in Materials Science*, 54, p. 664-688.

[113] KIM J.-Y. and GREER J.R. (2009). Tensile and compressive behavior of gold and molybdenum single crystals at the nano-scale. *Acta Materialia*, 57, p. 5245-5253.

[114] RASTOGI P.K. (eds.) (2000). Photomechanics, Springer, Berlin (Germany).

[115] PETERS W.H. and RANSON W.F. (1982). Digital Imaging Techniques In Experimental Stress Analysis. *Opt. Eng.*, 21(3), 213427.

[116] SUTTON M.A., WOLTERS W.J., PETERS W.H., RANSON W.F. and MCNEILL S.R. (1983). Determination of Displacements Using an Improved Digital Correlation Method, *Im. Vis. Comp.*, 1 (3), p. 133-139.

[117] CHU T. C., RANSON W. F., SUTTON M. A. and PETTERS W. H. (1985). Applications of Digital-Image-Correlation Techniques to Experimental Mechanics. *Exp. Mech.*, 3(25), p. 232-244.

[118] SUTTON M.A., MCNEILL S.R., HELM J.D. and CHAO Y.J. (2000). Advances in Two-Dimensional and Three-Dimensional Computer Vision, in : RASTOGI P.K. (eds.), *Photomechanics*, Springer, Berlin (Germany), p. 323-372.

[119] ROUX S., HILD F. and BERTHAUD Y. (2002). Correlation Image Velocimetry: A Spectral Approach, *Appl. Optics*, 41(1), p. 108-115.

[120] HILD F. and ROUX S. (2006). Digital image correlation : from displacement measurement to identification of elastic properties. *Strain*, 42(2), p. 69-80.

[121] RÉTHORÉ J., ELGUEDJ T., SIMON P. and CORET M. (2009). On the Use of NURBS Functions for Displacement Derivatives Measurement by Digital Image Correlation. *Experimental Mechanics*, 50(7), p. 1099-1116.

[122] SUTTON M.A. (2013). Computer vision-based, noncontacting deformation measurements in mechanics : a generational transformation. *Experimental Mechanics*, 65, 050802.

[123] HILD F. and ROUX S. (2012). Comparison of local and global approaches to digital image correlation. *Experimental Mechanics*, 52(9), p. 503-1519.

[124] SUTTON M.A., MCNEILL S.R., JANG J. and BABAI M. (1988). Effects of subpixel image restoration on digital image correlation error estimates, *Opt. Eng.*, 27(10), p. 870-877.

[125] SCHREIER H.W., BRAASCH J.R. and SUTTON M.A. (2000). Systematic errors in digital image correlation caused by intensity interpolation, *Opt. Eng.*, 39(11), p. 2915-2921.

[126] WANG Y.Q., SUTTON M.A., BRUCK H.A. and SCHREIER H.W. (2009). Quantitative error assessment in pattern matching: effects of intensity pattern noise, interpolation, strain and image contrast on motion measurements. *Strain*, 45, p. 160-178.

[127] BORNERT M., BRÉMAND F., DOUMALIN P., DUPRÉ J.-C., FAZZINI M., GRÉDIAC M., HILD F., MISTOU S., MOLIMARD J., ORTEU J.-J., ROBERT L., SURREL Y., VACHER P. and WATTRISSE B. (2009). Assessment of Digital Image Correlation Measurement Errors: Methodology and Results. *Experimental Mechanics*, 49(3), p. 353-370.

[128] AMIOT F., BORNERT M., DOUMALIN P., DUPRÉ J.-C., FAZZINI M., ORTEU J.-J., POILÂNE C., ROBERT L., ROTINAT R., TOUSSAINT E., WATTRISSE B. and WIENIN J.-S. (2013). Assessment of Digital Image Correlation Measurement Accuracy in the Ultimate Error Regime: Main Results of a Collaborative Benchmark. *Strain*, 49(6), p. 483-496.

[129] VENDROUX G. and KNAUSS W.G. (1998). Submicron deformation field measurements: part 2. Improved digital image correlation, *Exp. Mech.*, 38(2), p. 86-91.

[130] YA'AKOBOVITZ A., KRYLOV S. and HANEIN Y. (2010). Nanoscale displacement measurement of electrostatically actuated micro-devices using optical microscopy and digital image correlation. *Sensors and Actuators A*, 162, p. 1-7.

[131] HWANG S.-F., HORN J.-T. and WANG H.-J. (2008). Strain Measurement of nickel thin film by a digital image correlation method. *Strain*, 44, p. 215-222.

[132] HWANG S.-F., HORN J.-T. and WANG H.-J. (2008). Strain measurement of SU-8 photoresist by digital image correlation method with a hybrid genetic algorithm. *Optics and Lasers in Engineering*, 46, p. 281-289.

[133] SCRIVENS W.A., LUO Y., SUTTON M.A., COLLETTE S.A., MYRICK M.L., MINEY P., COLAVITA P.E., REYNOLDS A.P. and LI X. (2007). Development of patterns for digital image correlation measurements at reduced length scales. *Exp. Mech.*, 47, p. 63-77.

[134] SHARPE JR. W.N., PULSKAMP J., GIANOLA D.S., EBERL C., POLCAWICH R.G. and THOMPSON R.J. (2007). Strain measurements of silicon dioxide microspecimens by digital image processing. *Experimental Mechanics*, 47, p. 649-658.

[135] HA J.-E., PARK J.-H. and KANG D.-J. (2008). New strain measurement method at axial tensile test of thin films through direct imaging. *J. Phys. D. : Appl. Phys.*, 41, 175406.

[136] SHARPE JR. W.N. (2008). Mechanical property measurement at the micro/nano-scale. *Strain*, 44, p. 20-26.

[137] KIM C.-Y., SHARPE JR. W.N. and HEMKER K.J. (2012). An optical method for strain-controlled fatigue testing of microspecimens. *Journal of Microelectromechanical Systems*, 21(4), p. 774-775.

[138] NEGGERS J., HOEFNAGELS J.P.M., HILD F., ROUX S. and GEERS M.G.D. (2014). Direct stress-strain measurements from bulged membranes using topography image correlation. *Experimental Mechanics*, 54, p. 717-727.

[139] CHASIOTIS I. and KNAUSS W.G. (2000). Microtensile tests with the aid of probe microscopy for the study of MEMS materials. *Proceedings of SPIE*, 4175, p. 96-103.

[140] CHASIOTIS I. and KNAUSS W.G. (2002) A new microtensile tester for the study of MEMS materials with the aid of atomic force microscopy. *Experimental Mechanics*, 42(1), p. 51-57.

[141] KNAUSS W.G., CHASIOTIS I. and HUANG Y. (2003). Mechanical measurements at the micron and nanometer scales, *Mechanics of Materials*, 35, p. 217-231.

[142] CHO S.W. and CHASIOTIS I. (2007) Elastic properties and representative volume element of polycristalline silicon for MEMS. *Experimental Mechanics*, 47, p. 37-49.

[143] CHO S., CARDENAS-GARCIA J.F. and CHASIOTIS I. (2005). Measurement of nanodisplacements and elastic properties of MEMS via the microscopic hole method, *Sensors and Actuators A*, 120, p. 163-171.

[144] JONNALAGADDA K., CHO S.W., CHASIOTIS I., FRIEDMANN T. and SULLIVAN J. (2008). Effect of intrinsic stress gradient on the effective mode-I fracture toughness of amorphous diamond-like carbon films for MEMS. *Journal of the Mechanics and Physics of Solids*, 56, p. 388-401.

[145] XU Z.-H., JIN H., LU W.-Y., SUTTON M.A. and LI X. (2011). Influence of Scanning Rotation on Nanoscale Artificial Strain in Open-Loop Atomic Force Microscopy. *Experimental Mechanics*, 51(4), p. 619-624.

[146] VOGEL D., GOLLHARDT A. and MICHEL B. (2002) Micro- and nanomaterials characterization by image correlation methods. *Sensors and Actuators A*, 99, p. 165-171.

[147] SABATÉ N., VOGEL D., GOLLHARDT A., KELLER J., MICHEL B., CANÉ C., GRÀCIA I. and MORANTE J.R. (2006). Measurement of residual stresses in micromachined structures in a microregion. *Applied Physics Letters*, 88, 071910.

[148] VOGEL D., MAUS I. and MICHEL B. (2010) fibDAC stress relief : A novel stress measurement approach with high spatial resolution. *Electronics System Integration Technology Conference, ESTC 2010 - Proceedings*, 5642818.

[149] LI J.J., ZHAO C.W., XING Y.M., HOU X.H., FAN Z.C., JIN Y.J. and WANG Y. (2012) In-situ SEM investigation of sub-microscale deformation fields around a crack-tip in silicon. *Optics and Lasers in engineering*, 50(12), p. 1694-1698.

[150] SUTTON M.A., LI N., JOY D.C., REYNOLDS A.P. and LI X. (2007). Scanning Electron Microscopy for Quantitative Small and Large Deformation Measurements Part I: SEM Imaging at Magnifications from 200 to 10,000. *Experimental Mechanics*, 47, p. 775-787.

[151] SUTTON M.A., LI N., GARCIA D., CORNILLE N., ORTEU J.J., MCNEILL S.R., SCHREIER H.W., LI X. and REYNOLDS A.P. (2007). Scanning Electron Microscopy for Quantitative Small and Large Deformation Measurements Part II: Experimental Validation for Magnifications from 200 to 10,000. *Experimental Mechanics*, 47, p. 789-804.

[152] ESPINOSA H.D., PROROK B.C. and FISCHER M. (2003). A methodology for determining mechanical properties of freestanding thin films and MEMS materials, *Journal of the mechanics and physics of solids*, 51, p. 47-67.

[153] AMIOT F. and ROGER J.P. (2006). Nomarski imaging interferometry to measure the displacement field of micro-electro-mechanical systems. *Appl. Optics*, 45(30), p. 7800-7810.

[154] BONNOTTE E., DELOBELLE P., BORNIER L., TROLARD B. and TRIBILLON G. (1997). Two interferometric methods for the mechanical characterization of thin films by bulging tests. Application to single crystal of silicon. *J. Mater. Res.*, 12(9), p. 2234-2248.

[155] ASWENDT P., SCHMIDT C. D., ZIELKE D. and SCHUBERT S. (2003). ESPI solution for non-contacting MEMS-on-wafer testing. *Optics and Lasers in Engineering*, 40, p. 501?515.

[156] GANAPATI V., SCHOENFELDER S., CASTELLANOS S., OENER S., KOEPGE R., SAMPSON A., MARCUS M.A., LAI B., MORHERNN H., HAHN G., BAGDAHN J. and BUONASSISI T. (2010). Infrared birefringence imaging of residual stress and bulk defects in multicrystalline silicon. *J. Appl. Phys.*, 108, 063528.

[157] LEGROS M., GIANOLA D.S. and MOTZ C. (2010). Quantitative in situ mechanical testing in electron microscopes. *MRS Bulletin*, 35, p. 354-360.

[158] DALLY J.W. and READ D.T. (1993). Electron beam Moiré. *Experimental Mechanics*, 33(4), p. 270-277.

[159] LI Y.J., XIE H.M., GUO B.Q., LUO Q., GU C.Z. and XU M.Q. (2010) Fabrication of high-frequency moiré gratings for microscopic deformation measurement using focused ion beam milling. *J. Micromech. Microeng.*, 20, 055037.

[160] HŸTCH M. J., SNOECK, E. and KILAAS R. (1998). Quantitative measurement of displacement and strain fields from HREM micrographs. *Ultramicroscopy*, 74(3), p. 131-146.

[161] HŸTCH M.J. and HOUDELLIER F. (2007). Mapping stress and strain in nanostructures by high-resolution transmission electron microscopy. *Microelectronic engineering*, 84, p. 460-463.

[162] HŸTCH M., HOUDELLIER F., HÜE F and SNOECK E. (2008) Nanoscale holographic interferometry for strain measurements in electronic devices. *Nature*, 453(7198), p. 1086-1089.

[163] HŸTCH M., HOUDELLIER F., HÜE F and SNOECK E. (2011) Dark-field electron holography for the measurement of geometric phase. *Ultramicroscopy*, 111(8), p. 1328-1337.

[164] REBOH S., BENZO P., MORIN P., COURS R., HŸTCH M.J. and CLAVERIE A. (2013). A method to determine the Young's modulus of thin-film elements assisted by dark-field electron holography. *Appl. Phys. Lett.*, 102, 051911.

[165] BÉCHÉ A., ROUVIÈRE J.L., BARNES J.P. and COOPER D. (2013). Strain measurement at the nanoscale: comparison between convergent beam electron diffraction, nano-beam electron diffraction, high resolution imaging and dark field electron holography. *Ultramicroscopy*, 131, p. 10-23.

[166] HUMPHREYS F.J. (2001). Grain and subgrain characterization by electron backscatter diffraction. *J. Mat. Sci.*, 36, p. 3833-3854.

[167] KAMAYA M., WILKINSON A.J. and TITCHMARSH J.M. (2005). Measurement of plastic strain of polycristalline material by electron backscatter diffraction. *Nuclear Eng. Design*, 235, p. 713-725.

[168] WILKINSON A.J. (1996). Measurement of elastic strains and small lattice rotations using electron back scatter diffraction. *Ultramicroscopy*, 62, p. 237-247.

[169] WILKINSON A.J., MEADEN G. and DINGLEY D.J. (2006). High-resolution elastic strain measurement from electro backscatter diffraction patterns: new levels of sensitivity. *Ultramicroscopy*, 106, p. 307-313.

[170] MAURICE C. and FORTUNIER R. (2008). A 3D Hough transform for indexing EBSD and Kossel patterns. *Journal of Microscopy*, 230(3), p. 520-529.

[171] RIEDL T. and WENDROCK H. (2014). Reliability of high-resolution electron backscatter diffraction determination of strain and rotation variations using phase-only and cross correlation. *Crystal Research and Technology*, 49(4), p. 195-203.

[172] VAUDIN M.D., GERBIG Y.B., STRANICK S.J. and COOK R.F. (2008). Comparison of nanoscale measurements of strain and stress using electron back scattered diffraction and confocal Raman microscopy. *Appl. Phys. Lett.*, 93, 193116.

[173] NARAYANAN S., KALIDINDI S.R. and SCHADLER L.S. (1997). Determination of unknown stress states in silicon wafers using microlaser Raman spectroscopy. *Jal Appl. Phys.*, 82(5), p. 2595-2602.

[174] LOECHELT G. H., CAVE N.G. and MENÉNDEZ J. (1999). Polarized off-axis Raman spectroscopy: A technique for measuring stress tensors in semiconductors. *Journal of Applied Physics*, 86(11), p. 6164-6180.

[175] MIYATAKE T. and PEZZOTTI G. (2011). Tensor-resolved stress analysis in silicon MEMS device by polarized Raman spectroscopy. *Physica Status Solidi A*, 208(5), p. 1151-1158.

[176] ROBACH O., MICHA J.-S., ULRICH O. and GERGAUD P. (2011). Full local elastic strain tensor from Laue microdiffraction : simultaneous Laue pattern and spot energy measurement. *Applied Crystallography*, 44, p. 688-696.

[177] TRAVAILLOT T., DOHN S., BOISEN A. and AMIOT F. (2013). Imaging interferometry to measure surface rotation field. *Appl. Opt.*, 52(18), p. 4360-4369.

[178] NOMARSKI G. (1955). Microinterféromètre différentiel à ondes polarisées. *J. Phys. Radium*, 16, p. 9S-11S.

[179] FRANÇON M. and MALLICK S. (1971). Compensated Polarization Interferometers for the Observation of Phase Objects, in *Polarization interferometers: applications in microscopy and macroscopy*, Wiley-Interscience, p. 55-67.

[180] BOUSSINESQ M. J. (1885).Valeurs des déplacements, des déformations et de pressions intérieures, quand les potentiels se réduisent à un seul de leurs éléments, in *Application des potentiels à l'étude de l'équilibre et du mouvement des solides élastiques*, Gauthier-Villars, p. 81-108 (in French).

[181] MALACARA D. and HARRIS O. (1970). Interferometric measurement of angles. *Applied Optics*, 9(7), p. 1630-1633.

[182] CHAPMAN G.D. (1974). Interferometric Angular Measurement. *Appl. Opt.*, 13(7), p. 1646-1651.

[183] SHI P. and STIJNS E. (1988). New optical method for measuring small-angle rotations. *Appl. Opt.*, 27(20), p. 4342-4344.

[184] TAY C.J., QUAN C., WANG S.H. and SHANG H.M. (2001). Determination of a micromirror angular rotation using laser interferometric method. *Opt. Comm.*, 195(1-4), p. 71-77.

[185] GAO W., HUANG P.S., YAMADA T. and KIYONO S. (2002). A compact and sensitive two-dimensional angle probe for flatness measurement of large silicon wafers. *Precision Engineering*, 26(4), p. 396-404.

[186] SURREL Y., FOURNIER N., GRÉDIAC M. and PARIS P.-A. (1999). Phase-stepped deflectometry applied to shape measurement of bent plates. *Experimental Mechanics*, 39(1), p. 66-70.

[187] BORN M., WOLF E. and BHATIA A.B. (1959). Geometrical theory of optical imaging in *Principles of optics: electromagnetic theory of propagation, interference and diffraction of light*, Cambridge University Press (1959), p. 133-202.

[188] DUBOIS A., SELB J., VABRE L. and BOCCARA A.C. (2000). Phase measurements with wide-aperture interferometers. *Appl. Optics*, 39(14), p. 2326-2331.

[189] SHEPPARD C.R.J. and LARKIN K.G. (1995). Effect of numerical aperture on interference fringe spacing. *Appl. Optics*, 34 (22), p. 4731-4734.

[190] SCHULZ G. et ELSSNER K.-E. (1991). Errors in phase-measurement interferometry with high numerical apertures. *Appl. Optics*, 30 (31), p. 4500-4506.

[191] LEE S.S., AHN B. and YAMANAKA K. (1999). Characterization of delamination in titanium nitride coating on steel using acoustic microscopy. *J. Mater. Sci.*, 34, p. 6095.

[192] CAPELLA B. and DIETLER G. (1999). Force-distance curves by atomic force microscopy. *Surf. Sci. Report.*, 34, p. 1.

[193] RABE U. and ARNOLD W. (1994). Acoustic microscopy by atomic-force microscopy. *Appl. Phys. Lett.*, 64, p. 1493.

[194] OLIVER W.C. and PHARR G.M. (1992). An improved technique for determining hardness and elastic-modulus using load and displacement sensing indentation experiments. *J. Mater. Res.*, 7, p. 1564.

[195] LI X. and BHUSHAN B. (2002). A review of nanoindentation continuous stiffness measurement technique and its applications. *Mater. Charact.*, 48, p. 11.

[196] BAMBER M.J., COOKE K.E., MANN A.B. and DERBY B. (2001). Accurate determination of Young's modulus and Poisson's ratio of thin films by a combination of acoustic microscopy and nanoindentation. *Thin Solid Films*, 398, p. 299.

[197] JENNETT N.M., ALDRICH-SMITH G. and MAXWELL A.S. (2004). Validated measurement of Young's modulus, Poisson ratio, and thickness for thin coatings by combining instrumented nanoindentation and acoustical measurements. *J. Mat. Res.*, 19, p. 143.

[198] HURLEY D.C. and TURNER J.A. (2007). Measurement of Poisson's ratio with contact-resonance atomic force microscopy. *J. Appl. Phys.*, 102, 033509.

[199] LE ROUZIC J., DELOBELLE P., CRETIN B., VAIRAC P. and AMIOT F. (2011). Simultaneous measurement of Young's modulus and Poisson's ratio at microscale with two-modes scanning microdeformation microscopy. *Materials Letters*, 68, p. 370-373.

[200] DOHN S., SCHMID S., AMIOT F. and BOISEN A. (2010). Position and mass determination of multiple particles using cantilever-based sensors. *Appl. Phys. Lett.*, 97, 044103.

[201] STHAL F. and CRETIN B. (1993). Scanning microdeformation microscopy. *Appl. Phys. Lett.*, 62, p. 829.

[202] VAIRAC P. and CRETIN B. (1996). Scanning microdeformation microscopy in reflection mode. *Appl. Phys. Lett.*, 68, p. 461.

[203] VAIRAC P. and CRETIN B. (1996). New structures for heterodyne interferometric probes using double-pass. *Opt. Commun.*, 132, p. 19.

[204] CRETIN B. and VAIRAC P. (1997). Optical detection for scanning microdeformation microscopy. *Appl. Phys. Lett.*, 71, p. 2082.

[205] VAIRAC P. and CRETIN B. (1998). Frequency shift of a resonating cantilever in ac force microscopy : towards a realistic model. *Appl. Phys. A*, 66(1), p. S227-S230.

[206] LE ROUZIC J., VAIRAC P., CRETIN B. and DELOBELLE P. (2008). Sensitivity optimization of the scanning microdeformation microscope and application to mechanical characterization of soft materials. *Rev. Sci. Instr.*, 79, 033707.

[207] PRESS W. H., TEUKOLSKY S. A., VETTERLING W. T. and FLANNERY B. P. (2002). Numerical Recipes in C++. Cambridge University Press, Cambridge (UK).

[208] FENG R. and FARRIS R.J. (2002). The characterization of thermal and elastic constants for an epoxy photoresist SU8 coating. *J. Mater. Sci.*, 37, p. 4793.

[209] LAU G.K., GOOSEN J.F.L., VAN KEULEN F., CHU DUC T. and SARRO P.M. (2007). Powerful polymeric thermal microactuator with embedded silicon microstructure. *Appl. Phys. Lett.*, 90, 214103.

[210] MCALEAVEY A., COLES G., EDWARDS R.L. and SHARPE JR. W.N. (1999). Mechanical properties of SU-8. *Materials Research Society Symposium - Proceedings*, 546, p. 213.

[211] AL-HALHOULI A. T., KAMPEN I., KRAH T. and BÜTTGENBACH S. (2008). Nanoindentation testing of SU-8 photoresist mechanical properties. *J. Microelectron. Eng.*, 85, p. 942.

[212] SEIDEL H. and CSEPREGI L. (1983). Three-dimensional structuring of silicon for sensor applications. *Sensors and Actuators*, 4, p. 455-463.

[213] MEYER E. (1992). Atomic Force Microscopy. *Progress in surface science*, 41(1), p. 3-49.

[214] GIMZEWSKI J. K., GERBER C., MEYER E. and SCHLITTLER R. R. (1994). Observation of a chemical reaction using a micromechanical sensor. *Chem Phys. Lett.*, 217, p. 589-594.

[215] BARNES J.R., STEPHENSON R.J., WELLAND M.E., GERBER C. and GIMZEWSKI J.K. (1994). Photothermal spectroscopy with femtojoule sensitivity using a micromechanical device. *Nature*, 372, p. 79-81.

[216] THUNDAT T., SHARP S. L., FISCHER W. G., WARMACK R. J. and WACHTER E. A. (1995). Micromechanical radiation dosimeter. *Appl. Phys. Lett.*, 66(12), p. 1563-1565.

[217] WACHTER E. A., THUNDAT T., ODEN P. I., WARMACK R. J., DATSKOS P. G. and SHARP S. L. (1996). Remote optical detection using microcantilevers. *Review of Scientific Instruments*, 67(10), p. 3434-3439.

[218] MANALIS S.R., MINNE S.C., QUATE C.F., YARALIOGLU G.G. and ATALAR A. (1997). Two-dimensional micromechanical bimorph arrays for detection of thermal radiation. *Appl. Phys. Lett.*, 70(24), p. 3311-3313.

[219] VARESI J., LAI J., PERAZZO T., SHI Z. and MAJUMDAR A. (1997). Photothermal measurements at picowatt resolution using uncooled micro-optomechanical sensors. *Appl. Phys. Lett.*, 71 (3), p. 306-308.

[220] BERGER R., GERBER C., GIMZEWSKI J. K., MEYER E. and GÜNTHERODT H. (1996). Thermal analysis using a micromechanical calorimeter. *Appl. Phys. Lett.*, 69, p. 40-42.

[221] CHEN G. Y., THUNDAT T., WACHTER E. A. and WARMACK R. J. (1995). Adsorption-induced surface stress and its effects on resonance frequency of microcantilevers. *J. Appl. Phys.*, 77(8), p. 3618-3622.

[222] BERGER R., DELAMARCHE E., LANG H. P., GERBER C., GIMZEWSKI J.K., MEYER E. and GÜNTHERODT H.-J. (1997). Surface stress in the self-assembly of alkanethiols on gold. *Science*, 276, p. 2021-2024.

[223] BERGER R., DELAMARCHE E., LANG H.P., GERBER C., GIMZEWSKI J.K., MEYER E. and GÜNTHERODT H. (1998). Surface stress in the self-assembly of alkanethiols on gold probed by a force microscopy technique. *Appl. Phys. A.*, 66, S55-S59.

[224] BERGER R., LANG H.-P., DELAMARCHE E., GERBER C., GIMZEWSKI J.K., ANDREOLI C., BRUGGER J., DESPONT M. and VETTIGER P. (1997). Integration of silicon micromechanical arrays with molecular monolayers for miniaturized sensor systems. *IBM Research report*, RZ 2926.

[225] LANG H. P., BALLER M. K., BERGER R., GERBER C., GIMZEWSKI J. K., BATTISTON F., FORNARO P., RAMSEYER J.P., MEYER E. and GÜNTHERODT H. (1998). An artificial nose based on a micromechanical cantilever array. *IBM Research report*, Rz 3068.

[226] LANG H. P., BERGER R., BATTISTON F., RAMSEYER J. P., MEYER E., ANDREOLI C., BRUGGER J., VETTIGER P., DESPONT M., MEZZACASA T., SCANDELLA L., GÜNTHERODT H., GERBER C. and GIMZEWSKI J.K. (1998). A chemical sensor based on a micromechanical cantilever array for the identification of gases and vapors. *Appl. Phys. A.*, 66, S61-S64.

[227] LANG H. P., BERGER R., ANDREOLI C., BRUGGER J., DESPONT M., VETTIGER P., GERBER C., GIMZEWSKI J.K., RAMSEYER J.P., MEYER E. and GÜNTHERODT, H. (1997). Sequential position readout from arrays of micromechanical cantilever sensors. *Appl. Phys. Lett.*, 72(3), p. 383-385.

[228] BATTISTON F., RAMSEYER J. P., LANG H. P., BALLER M. K., GERBER C., GIMZEWSKI J. K., MEYER E. and GÜNTHERODT H. (2001). A chemical sensor based on a microfabricated cantilever array with simultaneaous resonance-frequency and bending readout. *Sensors and Actuators B*, 77, p. 122-131.

[229] LAVRIK N. V., SEPANIAK M. J. and DATSKOS P. G. (2004). Cantilever transducers as a platform for chemical and biological sensors. *Review of Scientific Instruments*, 75(7), p. 2229-2253.

[230] FRITZ J., BALLER M.K., LANG H.P., ROTHUIZEN H., VETTIGER P., MEYER E., GÜNTHERODT H., GERBER C. and GIMZEWSKI J.K. (2000). Translating biomolecular recognition into nanomechanics. *Science*, 288, p. 316-318.

[231] HANSEN K. M., JI H. F., WU G., DATAR R., COTE R., MAJUMDAR A., THUNDAT T. (2001). Cantilever-based optical deflection assay for discrimination of DNA single-nucleotide mismatches. *Anal. Chem.*, 73, p. 1567-1571.

[232] MARIE R., JENSENIUS H., THAYSEN J., CHRISTENSEN C. B. and BOISEN A. (2002). Adsorption kinetics and mechanical properties of thiol modified DNA-oligos on gold investigated by microcantilever sensors. *Ultramicroscopy*, 91, p. 29-36.

[233] MCKENDRY R., ZHANG J., ARNTZ Y., STRUNZ T., HEGNER M., LANG H. P. , BALLER M.K., CERTA U., MEYER E., GÜNTHERODT H. and GERBER C. (2002). Multiple label-free biodetection and quantitative DNA-binding assays on a nanomechanical cantilever array. *PNAS*, 99(15), p. 9783-9788.

[234] RAITERI R., GRATTAROLA M., BUTT H. J. and SKLADAL P. (2001). Micromechanical cantilever-based biosensors. *Sensors and Actuators B*, 79, p. 115-126.

[235] ARNTZ Y., SEELIG J. D., LANG H. P., ZHANG J., HUNZIKER P., RAMSEYER J. P., MEYER E., HEGNER M. and GERBER C. (2003). Label-free protein assay based on a nanomechanical cantilever array. *Nanotechnology*, 14, p. 86-90.

[236] FRITZ J. (2008). Cantilever biosensors. *Analyst*, 133, p. 855-863.

[237] WU G., JI H., HANSEN K., THUNDAT T., DATAR R., COTE R., HAGAN M.F., CHAKRABORTY A.K. and MAJUMDAR A. (2001). Origin of nanomechanical cantilever motion generated from biomolecular interactions. *PNAS*, 98, p. 1560-1564.

[238] HAGAN F.H., MAJUMDAR A. and CHAKRABORTY A.K. (2002). Nanomechanical forces generated by surface grafted DNA. *J. Phys. Chem. B*, 106 (39), p. 10163-10173.

[239] STEVENSON K. A., MEHTA A., SACHENKO P., HANSEN K. and THUNDAT T. (2002). Nanomechanical effect of enzymatic manipulation of DNA on microcantilever surfaces. *Langmuir*, 18, p. 8732-8736.

[240] CHA B.H., LEE S.-M., PARK J. C., HWANG K.S., KIM S. K., LEE Y.-S., JU B.-K. and KIM T. S. (2009). Detection of hepatitis B virus (HBV) DNA at femtomolar concentrations using a silica nanoparticle-enhanced microcantilever sensor. *Biosensors and Bioelectronics*, 25, p. 130-135.

[241] BONGRAIN A., UETSUKA H., ROUSSEAU L., VALBIN L., SAADA S., GESSET C., SCORSONE E., LISSORGUES G. and BERGONZO P. (2010). Measurement of DNA denaturation on B-NCD coated diamond microcantilevers. *Phys. Status Solidi A*, 207(9), p. 2078-2083.

[242] EOM K., JUNG H., JEONG S., KIM C.H., YOON D.S. and KWON T. (2011). Nanomechanical Motion of Microcantilevers Driven by Ion-Induced DNA Conformational Transitions. *BioNanoScience*, 1(4), p. 117-122.

[243] ZHAO Y., GANAPATHYSUBRAMANIAN B and SHROTRIYA P. (2012). Cantilever deflection associated with hybridization of monomolecular DNA film. *Jal. Appl. Phys.*, 111, 074310.

[244] ZHANG J., LANG H.P., YOSHIKAWA G. and GERBER C. (2012). Optimization of DNA hybridization efficiency by pH-driven nanomechanical bending. *Langmuir*, 28(15), p. 6494-6501.

[245] PINNADUWAGE L. A., BOIADJIEV V., HAWK J. E. and THUNDAT T. (2003). Sensitive detection of plastic explosives with self-assembled monolayer-coated microcantilevers. *Appl. Phys. Lett.*, 83(7), p. 1471-1473.

[246] PINNADUWAGE L. A., THUNDAT T., GEHL A., WILSON S. D., HEDDEN D. L. and LAREAU R. T. (2004). Desorption characteristics of uncoated silicon microcantilever surfaces for explosive and common nonexplosives vapors. *Ultramicroscopy*, 100, p. 211-216.

[247] BOSCO F.G., BACHE M., HWU E.-T., CHEN C.H., ANDERSEN S.S., NIELSEN K.A., KELLER S.S., JEPPESEN J.O., HWANG I.-S. and BOISEN A (2012). Statistical analysis of DNT detection using chemically functionalized microcantilever arrays. *Sensors and Actuators B*, 171-172, p. 1054-1059.

[248] ILIC B., CZAPLEWSKI D., CRAIGHEAD H.G., NEUZIL P., CAMPAGNOLO C. and BATT C. (2000). Mechanical resonant immunospecific biological detector. *Appl. Phys. Lett.*, 77 (3), p. 450-452.

[249] LAVRIK N.V. and DATSKOS P.G. (2003). Femtogram mass detection using photothermally actuated nanomechanical resonators. *Appl. Phys. Lett.*, 82 (16), p. 2697-2699.

[250] ILIC B., CRAIGHEAD H.G., KRYLOV S., SENARATNE W., OBER C. and NEUZIL P. (2004). Attogram detection using nanoelectromechanical oscillators. *J. Appl. Phys.*, 95 (7), p. 3694-3703.

[251] GUPTA A., AKIN D. and BASHIR R. (2004). Single virus particle mass detection using microresonators with nanoscale thickness. *Appl. Phys. Lett.*, 84 (11), p. 1976-1978.

[252] CHASTE J., EICHLER A., MOSER J., CEBALLOS G., RURALI R. and BACHTOLD A. (2012). A nanomechanical mass sensor with yoctogram resolution. *Nature Nanotechnology*, 7, p. 301-304.

[253] BRAUN T., BARWICH V., GHATKESAR M.K., BREDEKAMP A.H., GERBER C., HEGNER M. and LANG H.-P. (2005). Micromechanical mass sensors for biomolecular detection in a physiological environment. *Phys. Rev. E,* 72, 031907.

[254] BURG T.P. and MANALIS S.R. (2003). Suspended microchannel resonators for biomolecular detection. *Appl. Phys. Lett.*, 83 (13), p. 2698-2700.

[255] GODIN M., BRYAN A. K., BURG T. P., BABCOCK K. and MANALIS S.R. (2007). Measuring the mass, density, and size of particles and cells using a suspended microchannel resonator. *Appl. Phys. Lett.*, 91, 123121.

[256] ITOH T. and SUGA T. (1994). Force sensing microcantilever using sputtered zinc oxide thin film. *Appl. Phys. Lett.*, 64, p. 37-39.

[257] BERGER R., LANG H.P., GERBER C., GIMZEWSKI J.K., FABIAN G.H., SCANDELLA L., MEYER E. and GÜNTHERODT H. (1998). Micromechanical thermogravimetry. *Chem Phys. Lett.*, 294, p. 363-369.

[258] THAYSEN J., BOISEN A., HANSEN O. and BOUWSTRA S. (2000). Atomic force microscopy probe with piezoresistive read-out and highly symmetrical Wheatstone bridge arrangement. *Sensors and Actuators*, 83, p. 47-53.

[259] JOHANSSON A., CALLEJA M., RASMUSSEN P. A. and BOISEN A. (2005). SU-8 cantilever sensor system with integrated readout. *Sensors and Actuators A*, 123-124, p. 111-115.

[260] LOUI A., GOERICKE F.T., RATTO T.V., LEE J., HART B.R. and KING W.P. (2008). The effect of piezoresistive microcantilever geometry on cantilever sensitivity during surface stress chemical sensing. *Sensors and Actuators, A: Physical*, 147(2), p. 516-521.

[261] YOSHIKAWA G., LANG H.-P., AKIYAMA T., AESCHIMANN L., STAUFER U., VETTIGER P., AONO M., SAKURAI T. and GERBER C. (2009). Sub-ppm detection of vapors using piezoresistive microcantilever array sensors. *Nanotechnology*, 20(1), 015501.

[262] NOH J.W., ANDERSON R.R., KIM S., HU W. and NORDIN G.P. (2009). In-plane all-photonic transduction with differential splitter using double-step rib waveguide for photonic microcantilever arrays. *Optics Express*, 17(22), p. 20012-20020.

[263] ARAKAWA E.T., LAVRIK N.V. and DATSKOS P.G. (2003). Detection of anthrax simulants with microcalorimetric spectroscopy : Bacillus subtilis and Bacillus cereus spores. *Appl. Optics*, 42 (10), p. 1757-1762.

[264] GFELLER K.Y., NUGAEVA N. and HEGNER M. (2005). Rapid Biosensor for Detection of Antibiotic-Selective Growth of Escherichia coli. *Applied and environmental microbiology*, 71(5), p. 2626-2631.

[265] NUGAEVA N., GFELLER K.Y., BACKMANN N., LANG H.-P., DÜGGELIN M. and HEGNER M. (2005). Micromechanical cantilever array sensors for selective

fungal immobilization and fast growth detection. *Biosensors and Bioelectronics*, 21, p. 849-856.

[266] TARK S.-H., DAS A., SLIGAR S. and DRAVID V.P. (2010). Nanomechanical detection of cholera toxin using microcantilevers functionalized with ganglioside nanodiscs. *Nanotechnology*, 21, 435502.

[267] MERTENS J., DAUDÉN M.I., CARRASCOSA J.L. and TAMAYO J. (2012). Stepwise motion of a microcantilever driven by the hydrolysis of viral ATPases. *Nanotechnology*, 23, 015501.

[268] LONGO G., ALONSO-SARDUY L., MARQUES RIO L., BIZZINI A., TRAMPUZ A., NOTZ J., DIETLER G. and KASAS S. (2013). Rapid detection of bacterial resistance to antibiotics using AFM cantilevers as nanomechanical sensors. *Nature Nanotechnology*, 8, p. 522-526.

[269] LAM Y., ABU-LAIL N.I., ALAM M.S. and ZAUSCHER S. (2006). Using microcantilever deflection to detect HIV-1 envelope glycoprotein gp120. *Nanomedecine : Nanotechnology, Biology and Medecine*, 2, p. 222-229.

[270] ALODHAYB A., BROWN N., RAHMAN S.M.S., HARRIGAN R. and BEAULIEU L.Y. (2013). Towards detecting the human immunodeficiency virus using microcantilever sensors. *Appl. Phys. Lett.*, 102, 173106.

[271] HILL K., DUTTA P., ZAREBA A., ELDRIDGE M. L. and SEPANIAK M. J. (2008). Morphological and chemical optimization of microcantilever surfaces for thyroid system biosensing and beyond. *Analytica chimica acta*, 625, p. 55-62.

[272] BRAUN T., GHATKESAR M.K., BACKMANN N., GRANGE W., BOULANGER P., LETELLIER L., LANG H.-P., BIETSCH A., GERBER C. and HEGNER M. (2009). Quantitative time-resolved measurement of membrane protein-ligand interactions using microcantilever array sensors. *Nature Nanotechnology*, 4(3), p. 179-185.

[273] CHEN T., CHANG D.P., LIU T., DESIKAN R., DATAR R., THUNDAT T., BERGER R. and ZAUSCHER S. (2010). Glucose responsive polymer brushes for microcantilever sensing. *J. Mater. Chem.*, 20, p. 3391-3395.

[274] XU and MUTHARASAN (2009). Cantilever biosensors in drug discovery. *Expert Opinion on Drug Discovery*, 4(12), p. 1237-1251.

[275] SARPHIE D., MCKENDRY R. and NDIEYIRA J. (2009). Nanomechanical cantilever biosensors: A springboard to novel antibiotics. *Innovations in Pharmaceutical Technology*, 29, p. 12-17.

[276] HUBER F., LANG H.P., BACKMANN N., RIMOLDI D. and GERBER C. (2013). Direct detection of a BRAF mutation in total RNA from melanoma cells using cantilever arrays. *Nature Nanotechnology*, 8, p. 125-129.

[277] KANG K., SACHAN A., NILSEN-HAMILTON M. and SHROTRIYA P. (2011). Aptamer functionalized microcantilever sensors for cocaine detection. *Langmuir*, 27, p. 14696-14702.

[278] HOU H., BAI X., XING C., GU N., ZHANG B. and TANG J. (2013). Aptamer-based cantilever array sensors for oxytetracycline detection. *Anal. Chem.*, 85(4), p. 2010-2014.

[279] BOISEN A., DOHN S., KELLER S.S., SCHMID S. and TENJE M. (2011). Cantilever-like micromechanical sensors. *Reports on Progress in Physics*, 74(3), 036101.

[280] HUBER F., LANG H.P., HEGNER M., DESPONT M., DRECHSLER U. and GERBER C. (2008). Analyzing refractive index changes and differential bending in microcantilever arrays. *Review of scientific instruments*, 79, 086110.

[281] DOHN S., GREVE A., SVENDSEN W.E. and BOISEN A. (2010). The influence of refractive index change and initial bending of cantilevers on the optical lever readout method. *Rev. Sci. Instr.*, 81, 065104.

[282] ARLETT J.L., MYERS E.B. and ROUKES M.L. (2011). Comparative advantages of mechanical biosensors. *Nature Nanotechnology*, 6, p. 203-215.

[283] HEADRICK J.J., SEPANIAK M.J., LAVRIK N.V. and DATSKOS P.G. (2003). Enhancing chemi-mechanical transduction in microcantilever chemical sensing by surface modification. *Ultramicroscopy*, 97, p. 417-424.

[284] WATARI M., GALBRAITH. J., LANG H.-P., SOUSA M., HEGNER M., GERBER C., HORTON M.A. and MCKENDRY R.A. (2007). Investigating the molecular mechanisms of in-plane mechanochemistry on cantilever arrays. *J. Am. Chem. Soc.*, 129, p. 601-609.

[285] HILL K., DUTTA P., ZAREBA A., ELDRIDGE M. L. and SEPANIAK M. J. (2008). Morphological and chemical optimization of microcantilever surfaces for thyroid system biosensing and beyond. *Analytica chimica acta*, 625, p. 55-62.

[286] JI H.-F. and ARMON. B. D. (2010). Approaches to increasing surface stress for improving signal-to-noise ratio of microcantilever sensors. *Analytical Chemistry*, 82(5), p. 1634-1642.

[287] WU S., NAN T., XUE C., CHENG T., LIU H., WANG B., ZHANG Q. and WU X. (2013). Mechanism and enhancement of the surface stress caused by a small-molecule antigen and antibody binding. *Biosensors and Bioelectronics*, 48, p. 67-74.

[288] TABARD-COSSA V., GODIN M., BURGESS I.J., MONGA T., LENNOX R.B. and GRÜTTER P. (2007). Microcantilever-based sensors: effect of morphology, adhesion, and cleanliness of the sensing surface on surface stress. *Analytical chemistry*, 79(21), p. 8136-8143.

[289] WEISSMÜLLER J. and DUAN H. (2008). Cantilever bending with rough surfaces. *Physical Review Letters*, 101(14), 146102.

[290] GODIN M., TABARD-COSSA V., MIYAHARA Y., MONGA T., WILLIAMS P.J., BEAULIEU L.Y., LENNOX R.B. and GRÜTTER P. (2010). Cantilever-based sensing: The origin of surface stress and optimization strategies. *Nanotechnology*, 21(7), 075501.

[291] GRAHAME D.C. and WHITNEY R.B. (1942). The Thermodynamic Theory of Electrocapillarity. *J. Am. Chem. Soc.*, 64(7), p. 1548-1552.

[292] GRAHAME D.C. (1947). The electrical double-layer and the theory of electrocapillarity. *Chem. Rev.*, 41(3), p. 441-501.

[293] FREDLEIN R.A., DAMJANOVIC A. and BOCKRIS J.O.M. (1971). Differential surface tension measurements at thin solid metal electrodes. *Surface Science*, 25, p. 261-264.

[294] FREDLEIN R.A. and BOCKRIS J.O.M (1974). An electrocapillary study of the gold-perchloric acid solution interface. *Surf. Sci.*, 46, p. 641-652.

[295] RAITERI R. and BUTT H.J. (1995). Measuring electrochemically induced surface stress with an atomic force microscope. *J. Phys. Chem.*, 99, p. 15728-15732.

[296] HAISS W. and SASS J. K. (1995). Adsorbate-induced surface stress at the solid electrolyte interface measured with an STM. *Journal of Electroanalytical chemistry*, 386, p. 267-270.

[297] BRUNT T.A., RAYMENT T., O'SHEA S.J. and WELLAND M.E. (1996). Measuring the surface stresses in an electrochemically deposited metal monolayer: Pb on Au (111). *Langmuir*, 12, p. 5942-5946.

[298] IBACH H., BACH C.E., GIESEN M. and GROSSMAN A. (1997). Potential-induced stress in the solid-liquid interface: Au(111) and Au(100) in an HCl04 electrolyte. *Surf. Sci.*, 375, p. 107-119.

[299] HU K. and BARD A.J. (1998). In situ monitoring of kinetics of charged thiol adsorption on gold using an atomic force microscope. *Langmuir*, 14, p. 4790-4794.

[300] HAISS W., NICHOLS R. J., SASS J.K. and CHARLE K.P. (1998). Linear correlation between surface stress and surface charge in anion adsorption on Au(111). *Journal of Electroanalytical chemistry*, 452, p. 199-202.

[301] VALINCIUS G. (1998). Elastic Electrocapillary properties of polycristalline gold. *Langmuir*, 14, p. 6307-6319.

[302] VALINCIUS G. (1999). Electrocapillary equations of solid electrodes. *Journal of electroanalytical chemistry*, 478, p. 40-49.

[303] HAISS W. (2001). Surface stress of clean and adsorbate-covered solids. *Rep. Prog. Phys.*, 64, p. 591-648.

[304] HEATON T. and FRIESEN C. (2007). Pt111 and Au111 electrocapillarity: interphase structure, the pzc, and oxygen reduction. *J. Phys. Chem. C*, 111, p. 14433-14439.

[305] TIAN F., PEI J. H., HEDDEN D. L., BROWN G. M. and THUNDAT T. (2004). Observation of the surface stress induced in microcantilevers by electrochemical redox processes. *Ultramicroscopy*, 100, p. 217-223.

[306] LÁNG G. G., ROKOB T. A. and HORÁNYI G. (2005). Comments on "Observation of the surface stress induced in microcantilevers by electrochemical redox processes". *Ultramicroscopy*, 104, p. 330-332.

[307] TABARD-COSSA V., GODIN M., BEAULIEU L. Y. and GRÜTTER P. (2005). A differential microcantilever-based system for measuring surface stress changes induced by electrochemical reactions. *Sensors and Actuators B*, 107, p. 233-241.

[308] LEE D., THUNDAT T. and JEON S. (2007). Electromechanical identification of molecules adsorbed on microcantilevers. *Sensors and Actuators B*, 124, p. 143-146.

[309] QAZI M. and KOLEY G. (2008). NO2 detection using microcantilever based potentiometry. *Sensors*, 8, p. 7144-7156.

[310] BANGE A.F., BROWN G.M., SENESAC L.R. and THUNDAT T. (2008). Voltammetry of the Pb/Pb2+ redox couple using a gold microcantilever electrode. *ECS Transactions*, 16(11), p. 147-153.

[311] BANGE A.F., BROWN G.M., SENESAC L.R. and THUNDAT T. (2009). Stripping voltammetry of Pb and Cu using a microcantilever electrode. *Surface Science*, 603, p. L125-L127.

[312] XU Y., ZHANG B. and XIA W. (2009). The adsorption of dopamine on gold and its interactions with iron(III) ions studied by microcantilevers. *Analytica Chimica Acta*, 649, p. 117-122.

[313] YEN Y.-K., HUANG C.-Y., CHEN C.-H., HUNG C.-M., WU K.-C., LEE C.-K., CHANG J.-S., LIN S. and HUANG L.-S. (2009). A novel, electrically protein-manipulated microcantilever biosensor for enhancement of capture antibody immobilization. *Sensors and Actuators, B: Chemical*, 141(2), p. 498-505.

[314] ZHAO H., XUE C., NAN T., TAN G., LI Z., LI Q.X., ZHANG Q. and WANG B. (2010). Detection of copper ions using microcantilever immunosensors and enzyme-linked immunosorbent assay. *Analytica Chimica Acta*, 676, p. 81-86.

[315] ZHOU F., BIESHEUVEL M., CHOI E.-Y., SHU W., POETES R., STEINER U. and HUCK W.T.S. (2008). Polyelectrolyte brush amplified electroactuation of microcantilevers. *Nano letters*, 8(2), p. 725-730.

[316] AMIOT, F., KANOUFI F., HILD F. and ROGER J.P. (2009). Charge redistribution in electrochemically-actuated mechanical sensors. *Sensors and Actuators A*, 152, p. 88-95.

[317] NAGAI Y., DULANTO CARBAJAL J., WHITE J.H., SLADEK R., GRÜTTER P. and LENNOX R.B. (2013). An electrochemically controlled microcantilever biosensor. *Langmuir*, 29, p. 9951-9957.

[318] NORMAN L.L. and BADIA A. (2009). Redox actuation of a microcantilever driven by a self-assembled ferrocenylundecanethiolate monolayer : an investigation of the origin of the micromechanical motion and surface stress. *J. Am. Chem. Soc.*, 131(6), p. 2328-2337.

[319] DIONNE E.R., TOADER V. and BADIA A. (2014). Microcantilevers bend to the pressure of clustered redox centers. *Langmuir*, 30, p. 742-752.

[320] WHITE H.S., EARL D.J., NORTON J.D. and KRAGT H.J. (1990). In situ topographical imaging of electrode surfaces using high-resolution phase measurement interferometric microscopy. *Anal. Chem.*, 62, p. 1130-1134.

[321] LI Q. and WHITE H.S. (1995). Interferometric measurement of a depletion layer structure and volumetric data in concentrated organic redox solutions. *Anal. Chem.*, 67, p. 561-569.

[322] SMITH C.P., KENNEDY H.L., KRAGT H.J., WHITE H.S. and BIEGEN J.F. (1990). Phase-measurement interferometric microscopy of microlithographically fabricated platinum electrodes. *Anal. Chem.*, 62, p. 1135-1138.

[323] AMIOT F., ROGER J. P. and BOCCARA A. C. (2003). Towards massive parallel reading of sensitive mechanical microsensors. *Proc. SPIE : Advanced Biomedical and Clinical Diagnostic Systems*, 4958, p. 183. San Jose, CA, USA.

[324] HELM M., SERVANT J. J., SAURENBACH F. and BERGER R. (2005). Read-out of micromechanical cantilever sensors by phase shifting interferometry. *Appl. Phys. Lett.*, 87, 064101.

[325] AMIOT F. and ROGER J. P. (2006). Nomarski imaging interferometry to measure the displacement field of micro-electro-mechanical systems. *Appl. Optics*, 45(30), p. 7800-7810.

[326] WEHRMEISTER J., FUSS A., SAURENBACH F., BERGER R. and HELM M. (2007). Readout of micromechanical cantilever sensor arrays by Fabry-Perot interferometry. *Review of scientific instruments*, 78, 104105.

[327] KELLING S., PAOLONI F., HUANG J., OSTANIN V.P. and ELLIOTT S.R. (2009). Simultaneous readout of multiple microcantilever arrays with phase-shifting interferometric microscopy. *Rev. Sci. Instr.*, 80, 093101.

[328] KOEV S.T., BENTLEY W.E. and GHODSSI R. (2010). Interferometric read-out of multiple cantilever sensors in liquid samples. *Sensors and Actuators B*, 146, p. 245-252.

[329] MERTENS J., ÁLVAREZ M. and TAMAYO J. (2005). Real-time profile of microcantilevers for sensing applications. *Appl. Phys. Lett.*, 87, 234102.

[330] JEON S., JUNG N. and THUNDAT T. (2007). Nanomechanics of self-assembled monolayer on microcantilever sensors measured by a multiple-point deflection technique. *Sensors and Actuators B*, 122, p. 365-368.

[331] GODIN M., LAROCHE O., TABARD-COSSA V., BEAULIEU L. Y., GRÜTTER P. and WILLIAMS P. J. (2003). Combined in-situ micromechanical cantilever-based sensing and ellipsometry. *Review of Scientific Instruments*, 74(11), p. 4902-4907.

[332] AMIOT F., HILD F., KANOUFI F. and ROGER J. P. (2007). Identification of the electroelastic coupling from multi-physical fields measured at the micrometre scale. *J. Phys. D. : Appl. Phys.*, 40, p. 3314-3325.

[333] STONEY G. (1909). The tension of metallic films deposited by electrolysis. *Proc. Roy. Soc. London Ser A*, 82, p. 172.

[334] CHU S.N.G. (1998). Elastic bending of semiconductor wafer revisited and comments on Stoney's equation, *J. Electrochem. Soc.*, 145 (10), p. 3621-3627.

[335] KLEIN C. A. (2000). How accurate are Stoney's equation and recent modifications. *J. Appl. Phys.*, 88(9), p. 5487-5489.

[336] CHEN W.T. and NELSON C.W. (1979). Thermal stress in bonded joints. *IBM J. Res. Develop.*, 23 (2), p. 179-188.

[337] SUHIR E. (1986). Stresses in bi-metal thermostats. *J. Appl. Mech.*, 53, p. 657-660.

[338] SUHIR E. (1989). Interfacial stresses in bimetal thermostats. *J. Appl. Mech.*, 56, p. 595-600.

[339] VOLKERSEN O. (1938). Die Nietkraftverteilung in zugbeanspruchten Nietverbindungen mit konstanten Laschenquerschnitten. *Luftfahrtforschung*, 15 (1/2), p. 41-47.

[340] LEMAITRE J., LECKIE F.A. and SHERMAN D. (1992). Crazing of laminates. *Eur. J. Mech. A/Solids*, 11 (3), p. 289-304.

[341] HSUEH C.H. (2002). Thermal stresses in elastic multilayer systems. *Thin Solid Films*, 418, p. 182-188.

[342] VERMAAK J.S., MAYS C.W. and KUHLMANN-WILSDORF D. (1968). On surface stress and surface tension : 1 . Theoretical considerations. *Surface Science*, 12, p. 128-133.

[343] LAGOWSKI J., GATOS H.C. and SPROLES J.E.S. (1975). Surface stress and the normal mode of vibration of thin crystals : GaAs. *Appl. Phys. Lett.*, 26(9), p. 493-495.

[344] MOHILNER D.M. and BECK T.R. (1979). Thermodynamic theory of electrocapillarity for solid metal electrodes. *J. Phys. Chem*, 83(9), p. 1160-1166.

[345] JAECKEL L., LANG G. and HEUSLER K.E. (1994). New interferometric method to investigate surface energies at solid electrodes. *Electrochim. Acta*, 39, p. 1031-1038.

[346] CAMMARATA R. C. (1994). Surface and interface stress effects in thin films. *Progress in surface science*, 46(1), p. 1-38.

[347] IBACH H. (1997). The Role of Surface Stress in Reconstruction, Epitaxial Growth and Stabilization of Mesoscopic Structures. *Surface Science Reports*, 29, p. 193.

[348] SCHMICKLER W. and LEIVA E. (1998). A note on the surface stress and tension of solid metal electrodes. *Journal of electroanalytical chemistry*, 453, p. 61-67.

[349] SMETANIN M., VISWANATH R.N., KRAMER D., BECKMANN D., KOCH T., KIBLER L.A., KOLB D.M. and WEISSMULLER J. (2008). Surface stress-charge response of a (111)-textured gold electrode under conditions of a weak ion adsorption. *Langmuir*, 24, p. 8561-8567.

[350] SRINIVASAN V., CICERO G. and GROSSMAN J.C. (2008). Adsorption-induced surface stresses in alkanethiolate-Au self-assembled monolayers. *Phys. Rev. Letters*, 101, 185504.

[351] SADER J.E. (2001). Surface stress induced deflections of cantilever plates with applications to the atomic force microscope : rectangular plates. *J. Appl. Phys.*, 89(5), p. 2911-2921.

[352] CUENOT S., FRÉTIGNY C., DEMOUSTIER-CHAMPAGNE S. and NYSTEN B. (2004). Surface tension effect on the mechanical properties of nanomaterials measured by atomic force microscopy. *Phys. Rev. B*, 69, 165410.

[353] REN Y. and LAM D. C. C. (2005). Experiments on the elastic size dependence of LPCVD silicon nitride. *Mater. Res. Soc. Symp. Proc.*, 875.

[354] CHEN C.Q., SHI Y., ZHANG Y.S., ZHU J. and YAN Y.J. (2006). Size dependence of Young's modulus in ZnO nanowires. *Phys. Rev. Lett.*, 96, 075505.

[355] GURTIN M.E., MARKENSCOFF X. and THURSTON R.N. (1976). Effect of surface stress on the natural frequency of thin crystals. *Appl. Phys. Lett.*, 29(9), p. 529-530.

[356] GURTIN M. E. and MURDOCH A. I. (1978). Surface stress in solids. *Int. J. SolidsStruct.*, 14, p. 431-440.

[357] CHANG L. and RAJAPAKSE R.K.N.D. (2010). Continuum Models Incorporating Surface Energy for Static and Dynamic Response of Nanoscale Beams. *IEEE Transactions on Nanotechnology*, 9(4), p. 422-431.

[358] STEIGMANN D.J. and OGDEN R.W. (1997). Plane deformations of elastic solids with intrinsic boundary elasticity. *Proceedings of the Royal Society of London Series A-Mathematical Physical and Engineering Sciences*, 453, p. 853-877.

[359] STEIGMANN D.J. and OGDEN R.W. (1999). Elastic surface-substrate interactions. *Proceedings of the Royal Society of London Series A-Mathematical Physical and Engineering Sciences*, 455, p. 437-474.

[360] TOUPIN R.A. (1962). Elastic materials with couple-stresses. *Arch. ration. Mech. Analysis*, 11, p. 385.

[361] MINDLIN R.D. (1964). Micro-structure in Linear Elasticity. *Arch. Rat. Mech. Anal.*, 16, p. 51-78.

[362] GERMAIN P. (1973). The method of virtual power in continuum mechanics. Part 2: Microstructure. *SIAM Journal of Applied Mathematics*, 25(3), p. 556-575.

[363] LAM D.C.C., YANG F., CHONG A.C.M., WANG J. and TONG P. (2003). Experiments and theory in strain gradient elasticity. *J. Mech. Phys. Solids*, 51, p. 1477-1508.

[364] PAPARGYRI-BESKOU S., TSEPOURA K.G., POLYZOS D. and BESKOS D.E. (2003). Bending and stability analysis of gradient elastic beams. *Int J. Solids. Struct.*, 40, p. 385-400.

[365] LAZOPOULOS K.A. and LAZOPOULOS A.K. (2010). Bending and buckling of thin strain gradient elastic beams. *Eur. Jal. Mech. A / Solids*, 29, p. 837-843.

[366] CHEN S.H. and FENG B. (2011). Size effect in micro-scale cantilever beam bending. *Acta Mech.*, 219, p. 291-307.

[367] RAJABI F. and RAMEZANI S. (2012). A non linear microbeam model based on strain gradient elasticity theory with surface energy. *Arch. Appl. Mech.*, 82, p. 363-376.

[368] MA H.M., GAO X.-L. and REDDY J.N. (2008). A microstructure dependent Timoshenko beam model based on a modified couple stress theory. *J. Mech. Phys. Sol.*, 56, p. 3379-3391.

[369] LAZOPOULOS K.A. and LAZOPOULOS A.K. (2011). On a strain gradient elastic Timoshenko beam model. *ZAMM Journal of Applied Mathematics and Mechanics / Zeitschrift für Angewandte Mathematik und Mechanik*, 91(11), p. 875-882.

[370] RAMEZANI S. (2012). A micro scale geometrically non-linear Timoshenko beam model based on strain gradient elasticity theory. *Int. Jal. Non-linear Mech.*, 47, p. 863-873.

[371] LIU F., ZHANG Y. and OU-YANG Z. C. (2003). Flexoelectric origin of nanomechanic deflection in DNA-microcantilever system. *Biosensors and Bioelectronics*, 18, p. 655-660.

[372] BERGESE P., OLIVIERO G., ALESSANDRI I. and DEPERO L.E. (2007). Thermodynamics of mechanical transduction of surface confined receptor/ligand reactions. *Journal of colloid and interface science*, 316, p. 1017-1022.

[373] SUSHKO M.L., HARDING J.H., SHLUGER A.L., MCKENDRY R.A. and WATARI M. (2008). Physics of nanomechanical biosensing on cantilever arrays. *Advanced Materials*, 20, p. 3848-3853.

[374] FEDERICI S., OLIVIERO G., MAIOLO D., DEPERO L.E., COLOMBO I. and BERGESE P. (2012). On the thermodynamics of biomolecule surface transformations. *Journal of Colloid and Interface Science*, 375(1), p. 1-11.

[375] BEGLEY M. R., UTZ M. and KOMARAGIRI U. (2005). Chemo-mechanical interactions between adsorbed molecules and thin elastic films. *Jal. Mech. Phys. Solids*, 53, p. 2119-2140.

[376] BEGLEY M. R. and UTZ M. (2008). Multiscale modeling of adsorbed molecules on freestanding microfabricated structures. *Journal of Applied Mechanics-Transactions of the ASME*, 75(2), 021008.

[377] YI X. and DUAN H. L. (2009). Surface stress induced by interactions of adsorbates and its effect on deformation and frequency of microcantilever sensors. *Journal of the Mechanics and Physics of Solids*, 57(8), p. 1254-1266.

[378] ZANG J. and LIU F. (2007). Theory of bending of Si nanocantilevers induced by molecular adsorption: a modified Stoney formula for the calibration of nanomechanical sensors. *Nanotechnology*, 18, 405501.

[379] ZHANG J.Q., YU S.W., FENG X.Q. and WANG G.F. (2008). Theoretical analysis of adsorption-induced microcantilever bending. *Journal of Applied Physics*, 103, 093506.

[380] ZHANG J.Q., FENG X.Q., HUANG G.Y. and YU S.W. (2012). Theoretical analysis of chemisorption-induced surface stress. *Advanced Materials Research*, 528, p. 229-232.

[381] ZHANG J.Q., FENG X.Q., HUANG G.Y. and YU S.W. (2013). Chemisorption-induced microcantilever deflection : a theoretical model. *Phil. Mag. Letters*, 93(4), p. 183-195.

[382] SHENOY V. B., MILLER R., TADMOR E. B., RODNEY D., PHILLIPS R. and ORTIZ M. (1999). An Adaptive Finite Element Approach to Atomic-Scale Mechanics - The Quasicontinuum Method. *J. Mech. Phys. Solids*, 47(3), p. 611-642.

[383] ERICKSEN J.L. (2008). On the Cauchy-Born rule. *Mathematics and Mechanics of solids*, 13, p. 199-220.

[384] SUNYK R. and STEINMANN P. (2003). On higher gradients in continuum-atomistic modeling. *Int. Jal. Sol. Struct.*, 40, p. 6877-6896.

[385] SHENOY V.B. (2005). Atomistic calculations of elastic properties of metallic fcc crystal surfaces. *Phys. Rev. B*, 71, 094104.

[386] JAYAWARDANA K., MORDACQ C., ORTNER C. and PARK H.S. (2011) An analysis of surface relaxation in the surface Cauchy-Born model. *arXiv.math*, arXiv:1112.0683.

[387] FRIESECKE G. and JAMES R.D. (2000). A scheme for the passage from atomic to continuum theory for thin films, nanotubes and nanorods. *J. Mech. Phys. Solids*, 48, p. 1519-1540.

[388] TOUPIN R.A. and GAZIS D.C. (1963). Surface effects and initial stress in continuum and lattice models of elastic crystals. *Proceedings of the international conference on lattice dynamics*, p. 597-605. Copenhagen, Denmark.

[389] MINDLIN R.D. (1965). Second gradient theory of strain and surface tension in linear elasticity. *Int. J. Solids Structures*, 1, p. 417-438.

[390] MARANGANTI R. and SHARMA P. (2007). A novel atomistic approach to determine strain-gradient elasticity constants : tabulation and comparison for various metals, semiconductors, silica, polymers and the (ir) relevance for nanotechnologies. *J. Mech. Phys. Solids*, 55, p. 1823-1852.

[391] DANESCU A. and GRENET G. (2012). Continuum strain-gradient elasticity from discrete valence force model for diamond-like crystals. *Int. J. Fract.*, 174, p. 95-102.

[392] SHODJA H.M., AHMADPOOR F. and TEHRANCHI A. (2012). Calculation of the additional constants for fcc materials in second strain gradient elasticity: behavior of a nano-size Bernoulli-Euler beam with surface effects. *Jal of Applied Mechanics*, 79, 021008.

[393] JAKATA K. and EVERY A.G. (2008). Determination of the dispersive elastic constants of the cubic crystals Ge, Si, GaAs and InSb. *Phys. Rev. B.*, 77, 174301.

[394] HAO H.-Y. and MARIS H.J. (2001). Dispersion of the long-wavelength phonons in Ge, Si, GaAs, quartz, and sapphire. *Phys. Rev. B.*, 63, 224301.

[395] WU C., PETRINI V., JOSEPH E. and AMIOT F. (2014). Design and fabrication of a multiple-thickness electrochemical cantilever sensor. *Microelectronic engineering*, 119, p. 1-5.

[396] GARRAUD N., FEDALA Y., KANOUFI F., TESSIER G., ROGER J.P. and AMIOT F. (2011). Multiple wavelengths reflectance microscopy to study the multi-physical behavior of MEMS. *Optics Letters*, 36(4), p. 594-596.

[397] FEINLEIB J. (1966). Electroreflectance in metals. *Phys. Rev. Lett.*, 16, p. 1200.

[398] TESSIER G., HOL É S. and FOURNIER D. (2001). Quantitative thermal imaging by synchronous thermoreflectance with optimized illumination wavelengths. *Appl. Phys. Lett.*, 78, p. 2267.

[399] KOFMAN R., GARRIGOS R. and CHEYSSAC P. (1981). Optical-response of a charged metal-aqueous electrolyte interphase. *Thin Solid Films*, 82(1), p. 73-80.

[400] AMIOT F. (2007). A model for chemically-induced mechanical loading on MEMS. *J. Mechanics of Materials and Structures*, 2(9), p. 1787-1803.

[401] LIONS J. L. (Ed.). (1973). Perturbations singulières dans les problèmes aux limites et en contrôle optimal (Vol. 323). Berlin: Springer-Verlag.

[402] KLARBRING A. (1991). Derivation of a model of adhesively bonded joints by the asymptotic expansion method. *Int. J. Eng. Sci.*, 29(4), p. 493-512.

[403] GEYMONAT G. and KRASUCKI F. (1997). Analyse asymptotique du comportement en flexion de deux plaques collées. *C. R. Acad Sci. Paris*, 325, p. 307-314.

[404] MUSKHELISHVILI N. I. (1963). Some basic problems of the mathematical theory of elasticity. Gröningen, Netherlands: P. Noordhoff Ltd.

[405] AMIOT F. (2013). An Euler-Bernoulli second strain gradient beam theory for cantilever sensors. *Philosophical Magazine Letters*, 93(4), p. 204-212.

[406] FOREST S., CORDERO N.M. and BUSSO E.P. (2011). First vs second gradient of strain theory for capillarity effects in elastic fluid at small length scales. *Computational Materials Science*, 50, p. 1299-1304.